Charmonium production at HERA-B

Cand. Scient. Thesis

Andreas Christensen

Institute of Physics
University of Oslo

June 2002

I ain't happy
I'm feeling glad,
I got sunshine
in a bag.
I'm useless,
but not for long,
the future is comin' on

-*Gorillaz*

Acknowledgments

First of all I wish to thank my supervisor Assoc. Prof. Farid Ould-Saada for trusting me with this interesting and challenging topic. His enthusiasm and support throughout the work with this diploma thesis has been extraordinary. To have such expertise and insight available at any given time is more than any student can ask for. I am happy to realize that I have been very privileged. I also thank my second supervisor Prof. Torleiv Buran for his continuous support and good advice during this period.

This work has depended on the assistance of several people from the HERA-B collaboration. I am particularly indebted to Olya Igonkina who has willingly shared her experience and expertise on physics analysis at HERA-B and in general. The help she has provided has been nothing short of essential for the progress of this work. Brian Petersen has also been indispensable, always giving quick and accurate answers to considerably less accurate questions. I also thank Prof. Thomas Bauer, Prof. Antonio Zoccoli and Federico Sanchez for the discussions connected to this work.

I am grateful to all the members of EPF-group at the University of Oslo. The 'Ph.D team' has been a great resource, always ready to give this diploma student a helping hand. Yuriy Pylypchenko deserves to be mentioned specially for sharing all the technical problems as well as the late evenings at the office. I also thank my fellow students for creating a friendly atmosphere here in Oslo.

I have been fortunate enough to have a family to help me through the ups and downs of working on a diploma thesis. I am deeply grateful to my parents Else Marie and Kenneth Christensen who have provided moral support whenever I needed it. I also give a special thank to my mother-in-law Nanna Kurtze and her husband Kjell Terje Gundersen for their enthusiasm and encouragement.

But my main debt is to my wife Norunn whose cheerful spirit has been a never failing source of inspiration. Her ability to make every day a joyful one is what kept me going.

Abstract

The fraction of J/ψ produced from radiative decays of χ_c (F_{χ_c}) in proton-Carbon and proton-Titanium reactions at $\sqrt{s}$ = 42 GeV, has been measured. Based on a sample of approximately 3000 J/ψ particles reconstructed from a di-muon final state, the χ_c particle has been reconstructed by the addition of a photon. The number of reconstructed χ_c particles are $N^C_{\chi_c} = 171 \pm 52$ for Carbon reactions and $N^{Ti}_{\chi_c} = 105 \pm 46$ for Titanium reactions. The results obtained are $F^C_{\chi_c}$=$0.36 \pm 0.11(stat) \pm 0.04(syst)$ and $F^{Ti}_{\chi_c}$=$0.47 \pm 0.22(stat) \pm 0.05(syst)$ for Carbon and Titanium reactions respectively. The combined result for both target materials is $F^{both}_{\chi_c} = 0.32 \pm 0.10(stat) \pm 0.03(syst)$. The results agree well with previous measurements and the theoretical estimates.

Contents

List of Figures

Chapter 1

Introduction

The discovery of the J/ψ particle in 1974 was the first evidence of the existence of quarkonium, a bound state of a heavy quark-antiquark pair. The J/ψ particle, consisting of a c quark and its corresponding antiquark $\bar{c}$, was found to be unexpectedly narrow. This means that the J/ψ particle has only few available decay channels compared to what is expected from its high mass of 3.1 GeV. Much effort has been put into understanding the quarkonium decays, and these mechanisms are today well described by perturbative QCD. More recently the attention has turned to the production of quarkonium.
The bound states of $c\bar{c}$ pairs are called *charmonium* and include several particles with different angular momentum configurations. An important aspect in the description of charmonium production is to learn whether the charmonium particles are produced directly, or from the decays of heavier particles. Experimental results from the late 70's showed that a considerable fraction of the J/ψ were indeed produced from the decays of heavier charmonium states. But how large is this fraction for a given reaction at a certain energy? This question presents the subject for this thesis.
At HERA-B the reaction is between a proton beam of 920 GeV and a nucleon in a fixed target at a center of mass energy of $\sqrt{s} = 42$ GeV. The charmonium particles which decay into the J/ψ , are the χ_c particles, which include three different angular momentum states χ_{c0} , χ_{c1} and χ_{c2} . The decays of the χ_c states to J/ψ are radiative, or in other words, through the emission of a photon. The subject of this thesis can then be formulated more precisely:

What is the fraction of J/ψ produced from radiative χ_c decays in proton-nucleon reactions at $\sqrt{s} = 42\ GeV$?

The current model describing quarkonium production is under development and still needs experimental input. Today there exists only two previous measurements of the fraction of J/ψ produced from χ_c for proton-nucleon reactions. A successful measurement at HERA-B will then give an important contribution to our understanding of the mechanisms governing some of natures most fundamen-

tal processes.
Chapter 2 starts by presenting some of the motivations for measuring the fraction of J/ψ produced from χ_c . This is followed by an outline of the theoretical predictions for this measurement. Then, in Chapter 3, the experimental setup at HERA-B is presented. This includes a description of the subdetectors of the HERA-B spectrometer and the available data from the run 2000. The Monte-Carlo simulation of the events is also presented. In Chapter 4 the expressions used to calculate the fraction of J/ψ produced from χ_c , are presented. A general introduction to particle reconstruction is given before the the di-muon spectrum is presented. Then the J/ψ signal is studied in detail to isolate the particles used for the next part of the analysis: Reconstruction of the χ_c .
In Chapter 5 the method for the analysis is presented including χ_c reconstruction and background description. This is followed by the optimization of the χ_c signal where the number of reconstructed χ_c particles and the significance of the signal is studied for cuts on various parameters. The optimized signals are then used for calculation of the final results in Chapter 6. The signal is tested for stability within variation of some cuts, and a systematic error is estimated. Then the results are discussed and compared to previous measurements. The conclusions are presented in Chapter 7 followed by an outlook for the next period of data taking at HERA-B.

Chapter 2

Motivation

In the first section of this chapter some of the motivations behind a measurement the fraction of J/ψ produced from χ_c (F_{χ_c}) are summarized. They include estimations with respect to technical aspects of modern experiments, the search for *quark-gluon plasma* in addition to the intrinsic value of understanding quarkonium production. The current model for describing the production of quarkonium needs more experimental input, making this measurement highly relevant.
Examples of the problems connected to the earlier production models are given in the next section followed by a brief description of the theoretical assumptions behind the current production model. Then the predicted result on F_{χ_c} according to this model is discussed.

2.1 Motivation

Heavy quarkonium bound states, $Q\bar{Q}$, are formed by quark-pairs of the flavours c (charm), b (bottom) or t (top) quark. This gives the two quarkonium bound states charmonium $c\bar{c}$ and bottomonium $b\bar{b}$. Due to the high mass, and consequently the extremely short lifetime of the t quark, there has been no observations of a $t\bar{t}$ bound state.
The decay of quarkonium into lighter states is well understood; the theoretical predictions agree well with the experiments. But if this reaction is turned around and the production of quarkonium through partonic reactions is studied, the situation is dramatically different. During the last five years the theoretical models describing heavy quarkonium have developed rapidly as the experiments have opened the phenomenological possibilities. Charmonium production has had the central role in testing the production models and remains an important theoretical probe because bottomonium still is more scarcely produced in today's experiments. Although most of the modern experiments now focus on single quark bound states and their implications for CP-violation and 'New Physics', triggering and tagging of the events mostly depend on quarkonium leptonic de-

cays. This requires that the production mechanisms for quarkonium in general are well understood.
Also the search for *quark-gluon plasma* brings charmonium production mechanisms into actuality. Quark-gluon plasma is a deconfined state of partons expected to cause suppression of the charmonium bound state J/ψ due to inter-quark potential screening. The interpretation of the quark-gluon signature is thus dependent on well understood charmonium production. However, the intrinsic value of well described production mechanisms of quarkonium is motivating enough for most physicists to pursue the topic.
The experimental and theoretical efforts have culminated in a theoretical description of quarkonium production referred to as *non-relativistic Quantum Chromodynamics* (NRQCD). Having accounted for most of the problems encountered by its theoretical predecessor the *colour singlet model* (CSM) it is now regarded as *'Beyond any doubt the correct theory for quarkonium systems in the heavy quark limit'* [2].
Although NRQCD is now established as the best candidate theory, more and better measurements are still needed to develop the theory further. There already exist numerous measurements of the fraction of J/ψ produced from χ_c (F_{χ_c}) for pion beams, with different target materials at various energies (see figure 2.1). But for proton beams in fixed target experiments the measurements are few and of various quality with respect to the significance of the results. Making what seems like a reasonable demand of errors of less than 40% in the determination of the number of reconstructed χ_c , there is only one measurement of F_{χ_c} for fixed target proton beams. (See Appendix C for a summary of the previous measurements of F_{χ_c} .) Thus it is clear that more measurements are necessary. The measurements with pion beams are, as mentioned, more numerous and at center of mass energies much higher than the charmonium threshold $\sqrt{s} >> 2m_c$, where m_c denotes the mass of the c-quark, the cross sections are dominated by gluon fusion for both pion and proton beams [2]. Taking the quark-mass to be approximately 1.5 GeV [3] it is easily seen that this is the case for all experiments relevant here with beam energies from 185 to 300 GeV and center of mass energies in the range of 18-24 GeV. With F_{χ_c} expected to be energy independent in this range, the pion and proton beams should give close to similar results. As seen from figure 2.1 this is not the case; the pion beams have somewhat higher values. An additional measurement can therefore give an interesting contribution to the explanation of this discrepancy between the beam types. It should be noted that the F_{χ_c} is not affected by nuclear dependence, because this contribution cancels in the fraction of the cross-sections.
A successful measurement at HERA-B may give a significant contribution to the world statistics of the measurement of the fraction of J/ψ produced from χ_c . This is not to be seen as a measurement to select production models, but rather as input to develop the NRQCD theoretical framework. It is clear that the experimental situation suffers from both scarcity of measurements and discrepancies

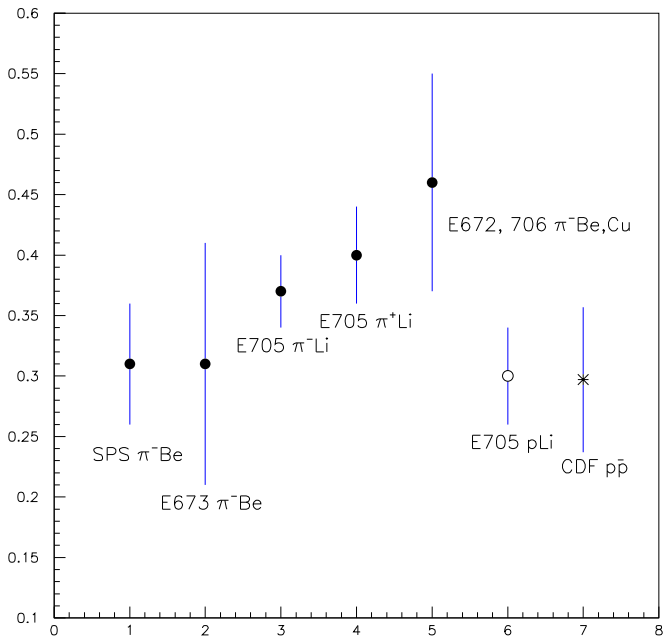

Figure 2.1: Experimental results for F_{χ_c} for pion and proton beams on fixed target and $p\bar{p}$ collisions.

between theory and data. The contribution from HERA-B is therefore necessary and important.

2.2 The Quarkonia production models

The parton sub-processes for $c\bar{c}$ production is quark annihilation and gluon-fusion:

$$q\bar{q} \rightarrow Q\bar{Q} \tag{2.1}$$
$$gg \rightarrow Q\bar{Q} \tag{2.2}$$

where (2.2) is the dominating process for the energy domain of the relevant fixed target experiments. The first order Feynman diagrams for these reactions are shown in figure 2.2. For consistency with the established models QCD, and the standard model in general, conservation of quantum numbers is of course fundamental in quarkonium production. This limits the possible spin-states that can

Particle	Mass [MeV]	ΔM [MeV]	$Br(\chi_{cJ} \to J/\psi\gamma)$ [%]
χ_{c0}	3415.0 ± 0.8	318.12	$(6.6 \pm 1.8) \cdot 10^{-3}$
χ_{c1}	3510.51 ± 0.12	413.63	27.3 ± 1.6
χ_{c2}	3556.18 ± 0.13	459.30	13.5 ± 1.1

Table 2.1: Some properties of the χ_c particles. ΔM is the mass difference with respect to the J/ψ particle and $Br(\chi_{cJ} \to J/\psi\gamma)$ is the branching ratio of indicated χ_c state to $J/\psi\ \gamma$.

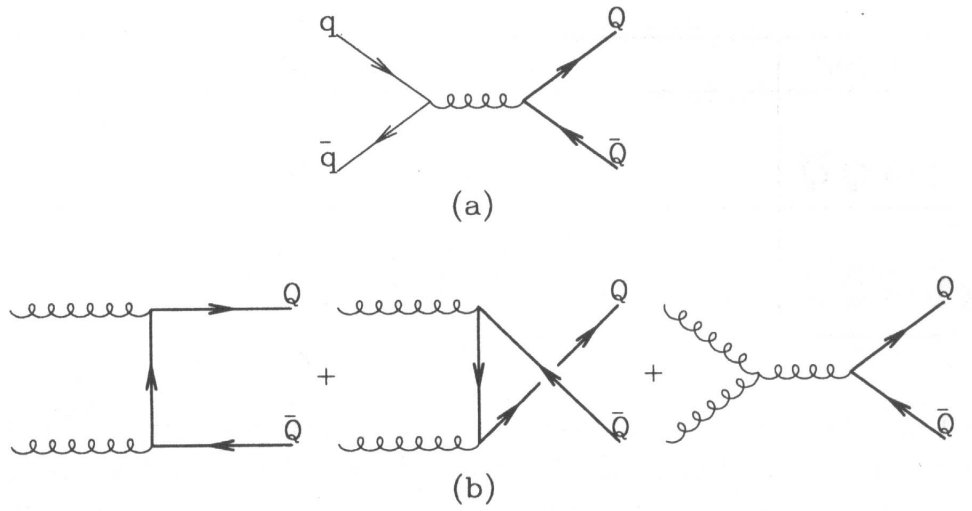

Figure 2.2: First order Feynman diagrams for first order quarkonia hadroproduction. a) quark-annihilation. b) gluon-fusion.

be created by eq. 2.2 in the lowest order processes (see figure 2.2) by Yang's theorem generalized for gluons: An odd-spin particle cannot couple to a symmetrical state of massless spin-one gluons, thereby pushing the production of J=1 charmonium states to higher order processes. This affects the gluon-fusion production of J/ψ, ψ' and χ_{c1} which then must include the emission of a hard gluon to reach a colour singlet final state. This significantly reduces the predicted production cross-section compared to the J=0,2 (η_c, χ_{c0} and χ_{c2}) states. (See figure 2.3 for an overview of the charmonium states.) This is not in agreement with experimental results and a theoretical underestimation of a factor 2 of F_{χ_c} is seen [4]. The effect of suppressed J=1 states is even more striking when considering the ratio of the χ_{c1} and χ_{c2} production cross-sections: The predicted value of $\frac{\sigma(\chi_{c1})}{\sigma(\chi_{c2})}$ =0.08 [4] is in sharp contrast to the measurement of 0.32 ± 0.14 of pN reactions at $\sqrt{s} = 39$ GeV done by the E771 collaboration at Fermilab [32]. The ratio of the χ_{c1} and χ_{c2} cross sections is approximately energy independent as long as the

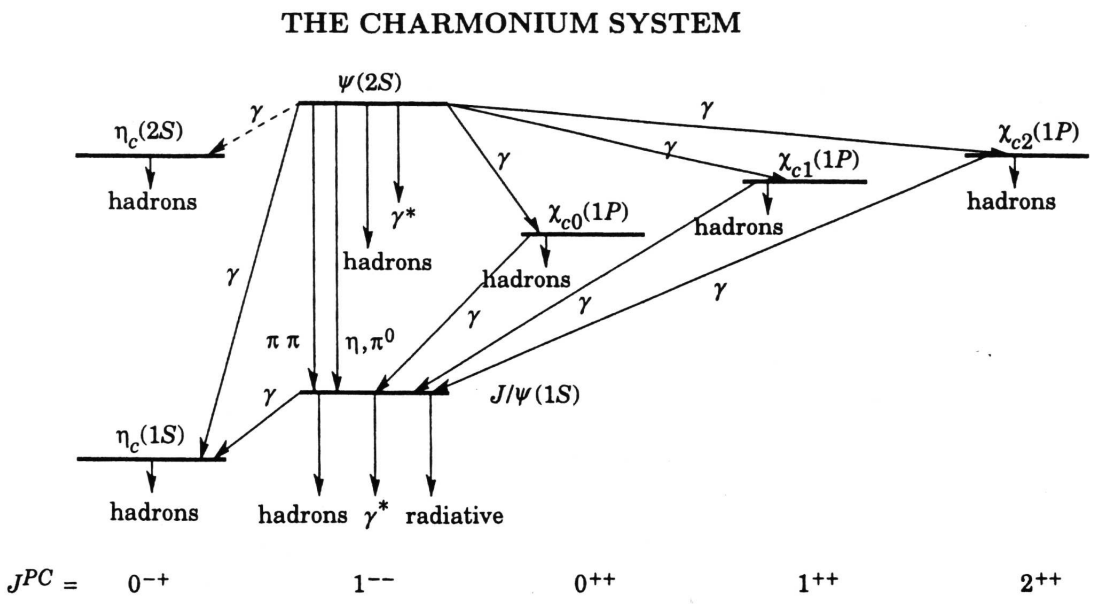

Figure 2.3: The Charmonium system.

gluon-fusion dominates the production [2].
The theoretical predictions cited above are deduced from the Color Singlet Model (CSM) [6] and display the necessity of a better theory. Non-Relativistic QCD (NRQCD) gives predictions in accordance with most experimental results, although the development of the theory is ongoing.
The NRQCD model opens the possibility for fragmentation. This is the creation of $q\bar{q}$ pairs by the colour force-field of the gluons. In effect this allows for the reaction (2.2) to occur subsequently in gluon-fusion, thereby enhancing the probability to produce a J=1 final state. Because the $q\bar{q}$ pairs produced through fragmentation will be in a colour octet state, the NRQCD model is also referred to as the Colour Octet Model.
The inclusion of octet states is incorporated in the NRQCD model through the method of factorization. This approach separates the calculation of the cross-section into two parts, one dealing with the colliding partons, the other with the subsequent hadronization of the two heavy quarks. The production cross-section for a general quarkonium state can then be written as

$$\sigma_H = \sum_{i,j} \int_0^1 dx_1 dx_2 f_{i/A}(x_1) f_{j/B}(x_2) \hat{\sigma}(i,j \to H), \tag{2.3}$$

$$\hat{\sigma}(i,j \to H) = \sum C^{ij}_{Q\bar{Q}[n]} \langle O^H_n \rangle. \tag{2.4}$$

where the integral in eq. 2.3 corresponds to the sum of partons in the colliding hadrons with the distribution functions $f_{i/A}(x_1)$ and $f_{j/B}(x_2)$. The distribution functions give the fraction of the total momentum $x_{1,2}$ ascribed to parton i,j.

This part of the quarkonium production cross-section is relativistic and thereby treated perturbatively. The coefficients $C^{ij}_{Q\bar{Q}[n]}$ in eq. 2.4 describe the production of the heavy quark pair in a state n, and the matrix element $\langle O^H_n \rangle$ describes the subsequent hadronization and is found empirically. Here $n = 1$ denotes a singlet state and $n = 8$ an octet state. In short: The probability of producing a quarkonium state is factorized as the product of the probability of creating a heavy quark pair multiplied by the probability of these quarks forming a given quarkonium state.
The validity of separating these parts is dependent on *velocity scaling*, *i.e.* that different orders of the relative velocity of the heavy quark pair v are separable. With the typical velocity of the heavy quarks decreasing with larger mass, the validity of the factorization picture is dependent on the quarks being heavy enough. It is convincingly the case for bottomonium and likely to be valid for charmonium with $m_c \approx 1.5$ GeV [5]. Assuming that the c-quark is sufficiently heavy, the factorization approach is valid and the relativistic physics of quark annihilation and gluon fusion can indeed be separated from the non-relativistic process of quarkonia formation.
For phenomenology some of the most sensitive and experimentally feasible probes of NRQCD are related to the production of the J=1 states. The measurements of the production cross-sections of J/ψ, ψ' and χ_{c1} states as well as the ratios of different spin-states like the F_{χ_c} are therefore well suited. A comparison with NRQCD and CSM predictions with data for J/ψ production cross-section is shown in figure 2.4 and clearly shows how NRQCD is able to account for the experimental results, whereas consideration of singlet states only leads to a large underestimation. The difference between the predictions of F_{χ_c} for singlet production only compared with the inclusion of octet states is less obvious. Both the J/ψ and the χ_{c1} states are J=1 states, and their relative enhancement due to octet contributions is not trivially estimated. The inclusion of octet states results in a lower predicted value of $F^{NR}_{\chi_c}$=0.27 for NRQCD compared to $F^{CSM}_{\chi_c}$=0.69 for CSM contributions only (see table 2.2). These values are given in [4], but they are based on an estimate of the production cross-section ratio of $\frac{\sigma(\chi_{c1})}{\sigma(\chi_{c2})}$ =0.15. A more recent estimate, after inclusion of higher order velocity expansions, suggests a value of 0.3 [2]. The exact impact of the higher order velocity expansions for the NRQCD prediction of F_{χ_c} is not quoted in [4], but it is expected that the F_{χ_c} NRQCD prediction will increase. The NRQCD-model is still being developed and it is difficult to give a definite predicted value for F_{χ_c} . However, the prediction

$$F_{\chi_c} \geq 0.27$$

is expected to be close to the correct value, although not completely up to date. The semi-empirical form of NRQCD model makes more experimental input crucial for further development. Using the available data from the 2000 run at

HERA-B, a measurement of F_{χ_c} may be possible, and can then give a welcome contribution to the NRQCD-model. Also measurements of the production cross section of J/ψ is ongoing at HERA-B and a measurement of the ψ' production cross-section should be possible after the next running period.
In this Chapter the motivations for measuring F_{χ_c} at HERA-B have been presented. The fundamental theoretical assumptions for the NRQCD model is given, and the predictions of this model have been compared to those of the previous CSM model.
In the next chapter a description of the experimental setup and the available data from the run 2000 at HERA-B is presented. The production of Monte-Carlo simulated events used in the following analysis are also described.

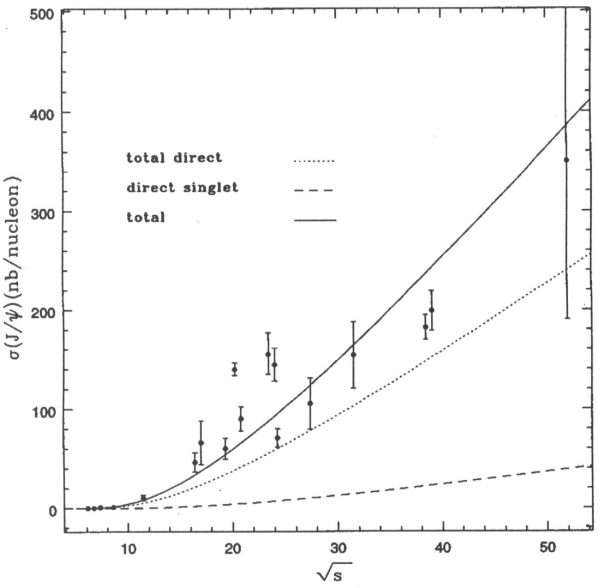

Figure 2.4: The J/ψ production cross sections in proton-nucleon collisions. The solid line is the NRQCD-model estimation including direct production and radiative feed-down from $\chi_c \to J/\psi\ \gamma$, $\psi' \to J/\psi$ +X and $\psi' \to \chi_c\ \gamma$, $\chi_c \to J/\psi\ \gamma$. The dotted line shows the direct cross-section including octet-contributions and the dashed line is the predictions including singlet contributions only (CSM). The distribution is from [2].

Topic	pN CSM	pN NRQCD	pN exp.	$\pi^- N$ CSM	$\pi^- N$ NRQCD	$\pi^- N$ exp.
$\sigma_{J/\psi}$	33 nb	90 nb	143 ± 21nb	38 nb	98 nb	178 ± 21 nb
F_{χ_c}	0.69	0.27	0.31 ± 0.04	0.66	0.28	0.37 ± 0.03
$\frac{\sigma(\chi_{c1})}{\sigma(\chi_{c2})}$	0.08	0.15	$0.08^{+0.25}_{-0.15}$*	0.11	0.13	$0.52^{+0.57}_{-0.27}$

Table 2.2: Comparisons between theoretical predictions from the Color Singlet Model (CSM) and Non Relativistic QCD (NRQCD) with experimental results. The experimental values are from the E705 experiment at Fermilab where 300 GeV beams of protons and $\pi^{\pm}$ were used on a Lithium target[4]. *) This value is from [31] and is the combined result for pion and proton beams.

Chapter 3

Experimental setup

This Chapter begins with an overview of the HERA-B experiment. First some of the general features of the experiment are presented, followed by a closer look at the sub-detectors of the HERA-B spectrometer. Then the the main features of the trigger systems used during the run 2000 are presented. The available data sample is described followed by a description of how the Monte-Carlo simulation is performed. Then the sample of available Monte-Carlo simulated events is described at the end of this chapter.

3.1 Overview

The HERA facility at DESY (Deutsches Elektronen Sychrotron) is host to the only electron-proton and positron-proton colliding beam experiments in the world. The electrons or positrons have an energy of 27 GeV and run in the opposite direction of the 920 GeV protons which are used in the HERA-B experiment. See figure 3.1 for an overview of the HERA storage rings and the DESY experiments. The proton beam at HERA-B is divided into 220 parts, or 'buckets', separated by time intervals of 96 ns. Only 180 of these buckets are filled, resulting in a bunch crossing rate of around 8.5 MHz. The fixed target gives a center of mass energy of $\sqrt{s} = 42.6$ GeV for the pN-reactions.
A schematic view of the spectrometer at HERA-B is shown in figure 3.2. The subdetectors are described in the following sections.

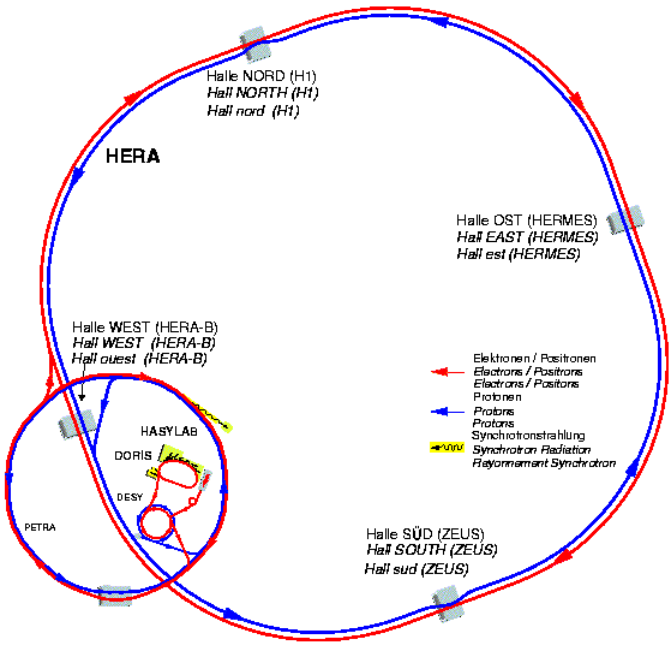

Figure 3.1: Overview of the DESY research facility showing the HERA-rings with electron or positron beams (clockwise) and the protons (counter-clockwise) used for the HERA-B experiment.

3.2 Target

A target consisting of up to eight wires is inserted into the halo of the proton beam to generate the interactions measured by the HERA-B spectrometer. The wires are mounted on movable forks, making it possible to adjust the position relative to the beam and thereby control the interaction rate. The target configuration is shown in figure 3.3. In the run 2000 the J/ψ triggered data taking has been done with Carbon and Titanium wires. Physics studies related to atomic-number dependencies are planned for the next data-taking period using several different target materials. Tungsten, Aluminum, Iron and Carbon are the suggested materials.

3.3 Vertex Detector System

The Vertex Detector System (VDS) is designed to give information about the position of the vertices of charged particles. It is positioned between the target and the magnet (see figure 3.2) and consists of eight superlayers of detectors

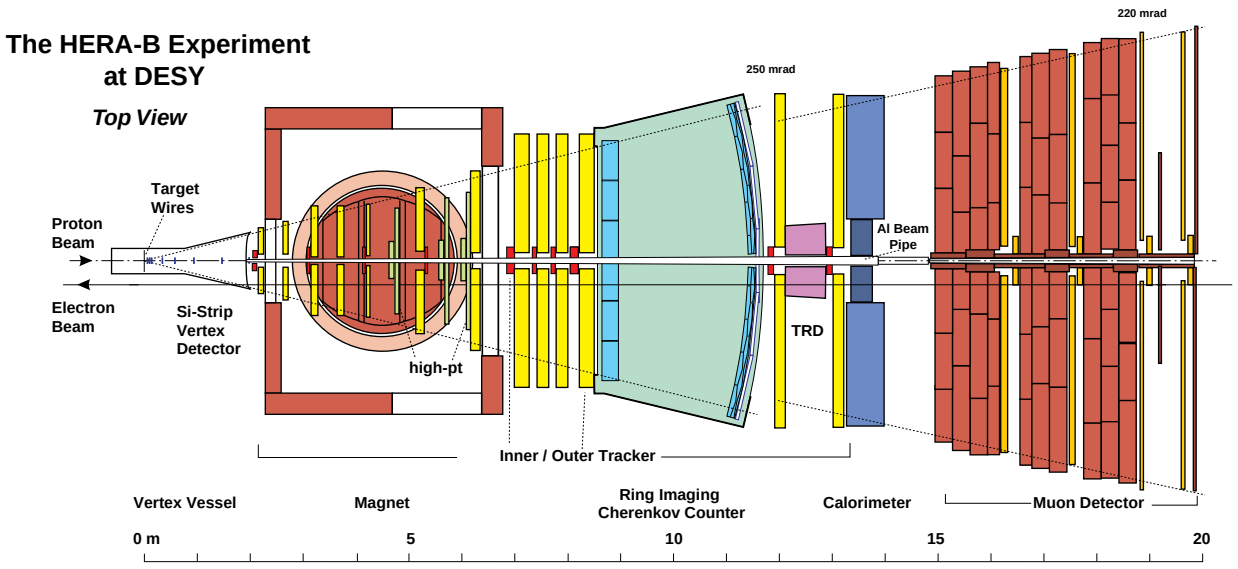

Figure 3.2: The HERA-B spectrometer at DESY, top view. Note that the tracking superlayers inside the magnet is now removed, but were present during the run 2000. The Transition Radiation Detector was not included in the spectrometer.

placed perpendicular to the beam (figure 3.4). Each superlayer is divided into four segments of double sided Silicon microstrip detectors. The VDS segments are retractable and their position relative to the beam can be adjusted. The superlayers 1-7 can be retracted into protective 'Roman pots' to prevent radiation damage. The resolution achieved J/ψ reconstructed from $\mu^+\mu^-$ or e^+e^- is 60 μm in the xy-plane and 500 μm in the z direction. The distribution of the VDS-hits in a run with eight wires is shown in figure 3.5. The VDS has an angular range of 10-250 mrad and covers the full acceptance of the detector.

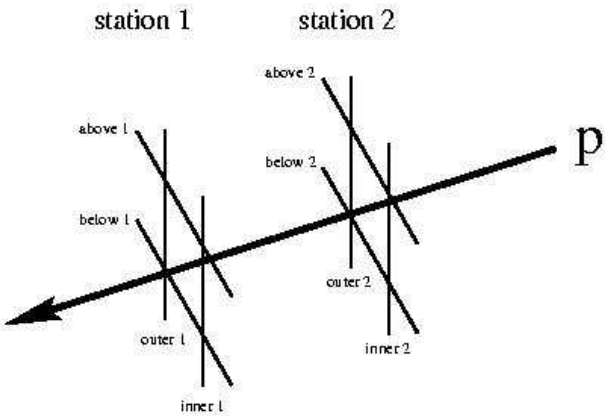

Figure 3.3: Schematic view of the target configuration with eight wires. The inner 2 wire (Carbon) and the below 1 (Titanium) have been used for the J/ψ triggered events in run 2000.

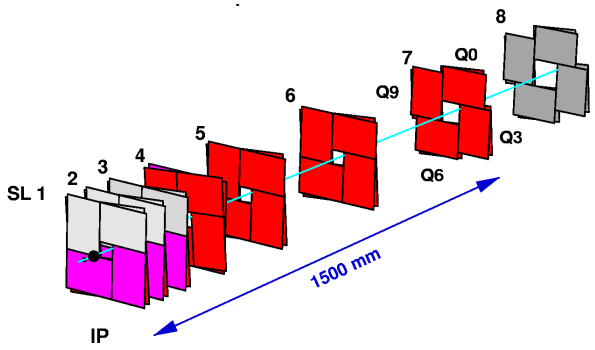

Figure 3.4: The configuration of the Vertex Detector System at HERA-B.

3.4 Magnet and Tracking

The magnet is used for momentum determination of charged particles. Knowing the magnetic field strength, the momentum is calculated from the curvature of the tracks. The magnet at HERA-B has a vertically oriented field of 2.13 Tm, resulting in a horizontal bending plane.
The Main tracking system is subdivided into the Inner Tracker (ITR) and Outer Tracker (OTR). This is done because the particle flux close to the beam is high and requires higher resolution than the area further out. The ITR is constructed using microstrip gas chambers and covers the area closer than 25 cm to the beam pipe. The ITR was still under commissioning during the run 2000 and could not be included in analysis or triggering. The OTR, however achieved a hit efficiency of 90% and a position resolution of $350\mu m^2$ in the xy-plane and played an important part in triggering the J/ψ events. It is a gaseous drift chamber construction where charged particles cause ionization of the gas which in turn can be mea-

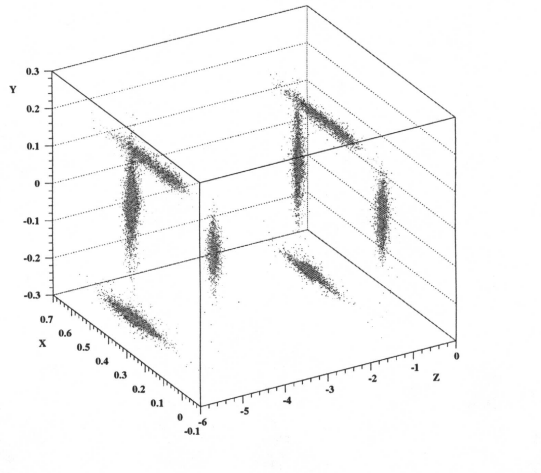

Figure 3.5: Reconstructed vertices using the VDS detector. The vertices show the positions of the eight target wires.

sured. The trajectory of the particle can then be reconstructed by connecting the measured hits. The chambers are hexagonal and are called *honeycomb chambers*. The chambers are divided into segments where the ones closest to the beam pipe, or closest to the ITR, have 5 mm cells, while the others have 10 mm cells. This is again to accomodate for the increased particle flux closer to the beam pipe. As can be seen in figure 3.6, the OTR superlayers are divided into three different regions. The Magnet Chambers are placed from the area after the target, inside and behind the magnet. They are used for momentum determination as described above. The Pattern Recognition Chambers and the Trigger Chambers are used for reconstructing the straight tracks behind the magnet to give information for event triggering. The magnet-chambers MC2-MC7 will be removed for the next period of data-taking.

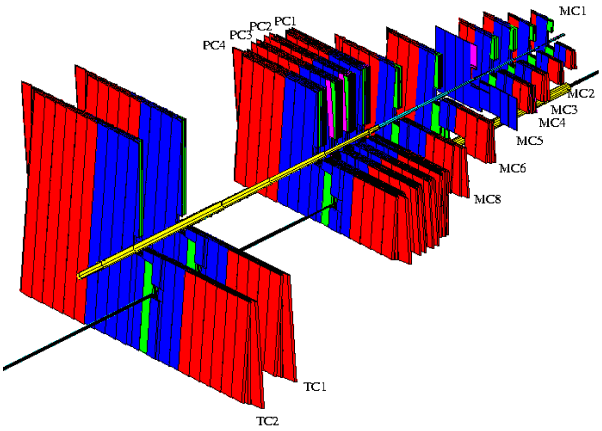

Figure 3.6: The Outer Tracker superlayer configuration. The beam direction on this picture is from right to left. The darkest areas show the segments with 5 mm cells closest to the beam, while the other chambers have 10 mm cells. (MC= Magnet Chambers, PC = Pattern recognition Chambers, TC= Trigger Chambers.)

3.5 Ring Imaging Cherenkov counter

The Ring Imaging Cherenkov counter (RICH) has the purpose of identifying particles for tagging decay modes. It works by the principle that a charged particle emits photons at a certain angle when traversing a gas or a liquid in which the speed of light is less than the speed of the particle. The angle of emission is a function to the particle mass, and one can thereby identify the particle. The construction of the HERA-B RICH is shown in figure 4.8. Spherical and planar mirrors reflect the emitted photons on to a photon-detector. Because the photons are emitted in a cone around the particle trajectory, they produce a circular hit pattern on the photon detectors. Due to the relatively low number of emitted photons per particle, the task of reconstructing the circles is difficult. The two methods that have been tested in the run 2000 are described in [34] and [35]. Since the particle identification is performed based on properties connected to the particle mass, the separation of particles that are close in mass is as a consequence hard to perform. Muons and charged pions, with a mass difference of 34 MeV, are therefore not well separated as can be seen in figure 3.8; the fat line marked 'π' in also contains muons. The RICH was successfully operated throughout the 2000 run.

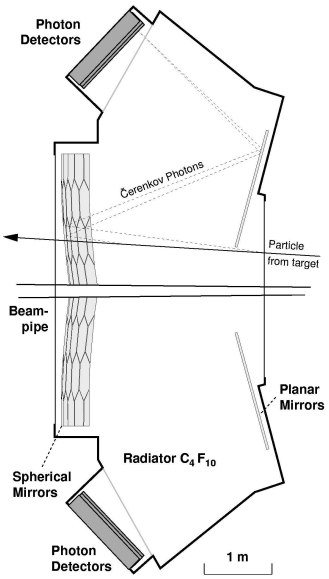

Figure 3.7: Schematic view of the Ring Imaging Cherenkov detector. Note how the emitted photons are reflected onto the photo sensitive detector via spherical and planar mirrors.

3.6 Electromagnetic calorimeter

The electromagnetic calorimeter (ECAL) is used both for electron identification and for photon detection. Electron identification enables triggering on electrons from J/ψ decays while detected photons are used for data-analysis, like reconstruction of radiative $\chi_c \rightarrow J/\psi\ \gamma$ decays. The ECAL is divided into three parts, Inner, Middle and Outer. The Inner part of the ECAL has higher granularity and better energy resolution than the Middle part which in turn is more sensitive than the Outer part. As can be seen from figure 5.7, the ECAL consists of modules. Each module is divided into cells, and the cell size is adjusted with respect to the lateral position of the module. In the Outer ECAL each module contains only one cell, while each module of the Middle part has 4 cells. In the inner part, where the highest resolution is needed, the modules are divided into 25 cells. The modules are built with shashlik sampling calorimeter technology using a sandwiched structure of lead or tungsten absorbers between layers of plastic scintillators. When electrons or photons hit the absorbers, electromagnetic showers are generated producing light emission in the scintillators, in turn amplified by photon-multipliers (see figure 3.11).
The ECAL signals are reconstructed as *clusters*, a collection of hit-cells of various configurations. The hit-cells is an ECAL cell with a 'considerable'[1] measured energy. A base cluster consists of hit cells only, and is typically caused by electromagnetic showers or light hadrons. Structured clusters are built up from more than one cluster and several hit cells [36]. The calibration of the ECAL was done

[1]The exact energy threshold is not known to the author.

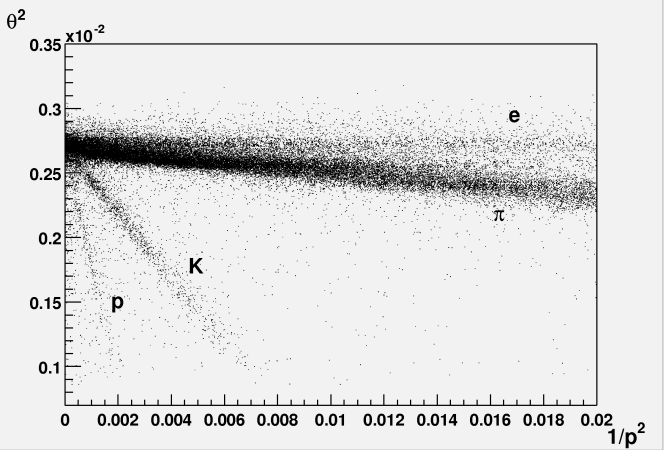

Figure 3.8: Particle identification using the RICH. The square of the Cherenkov angle is plotted as a function of the inverse square of the particle momentum. The separate lines show the different particle signatures. The fat line for π^0 contains muons due to the small mass difference of these two particles.

by reconstruction of π^0 from two clusters [14]. The Inner and Middle part were successfully calibrated from reconstructed π^0 signals (see figure 3.9), while the calibration of the Outer part did not reach the same level of accuracy. For the run 2000 analyses inclusion of the Outer ECAL is therefore questionable when precise cluster energies are needed [37]. This is indeed the case for χ_c reconstruction, and the results are therefore discussed without inclusion of the Outer ECAL in Section 6.3.3. The energy resolution is, for the Inner ECAL, estimated to

$$\frac{\sigma(E)}{E} = \frac{22.5\%}{\sqrt{E}} + 1.7\%. \tag{3.1}$$

There were no available estimates for the energy resolution of the Middle and Outer ECAL. The obtained spatial resolution was of 0.3 cm and 1.0 cm for the Inner and Middle parts respectively.

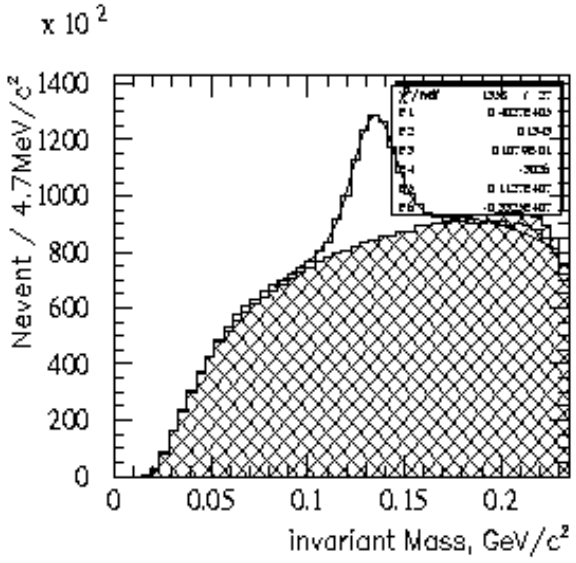

Figure 3.9: The π^0 reconstructed from two ECAL clusters after calibration of the ECAL. The mean position of the π^0 signal is 0.134 GeV. The picture is from [14]

3.7 Muon System

The Muon system is used for particle identification in data-analysis as well as for triggering on muonic J/ψ decays. It consists of 4 superlayers intersectioned by iron loaded concrete absorbers. The absorbers are used to screen out hadrons, which can penetrate less material than muons. Three different detectors are used in the Muon System. Gas Pixel chambers are used in the innermost region with the highest occupancy. The area further from the beam is covered by tube chambers in the first two superlayers (MU1 and MU2), and Pad chambers in the remaining two superlayers (MU3 and MU4). The signals in the Muon System are generated similarly to the Main Tracker; the traversing muons ionize the gas inside the chambers allowing for free electrons to drift and generate a signal. The Muon system covers angles from 10 mrad to 160 mrad in the y-direction and 220 mrad in the x-direction. For the run 2000, only the Tube chambers were used, reducing the acceptance to around 30% for muons from J/ψ decays.

3.8 Trigger

The concept of a trigger-system is basically to decide if an event is worth storing. It can be compared to a filter which only lets a few events, that fulfill a given set of criteria, pass. A well operating trigger-system is essential for an experiment like HERA-B because of the high interaction rate and because the interesting events ($b\bar{b}$ and $c\bar{c}$) are rare compared to the more abundant light quark final states. However, the run 2000 has been operated with the relatively low interaction rate of 5 MHz mainly because of problems with the trigger system. The

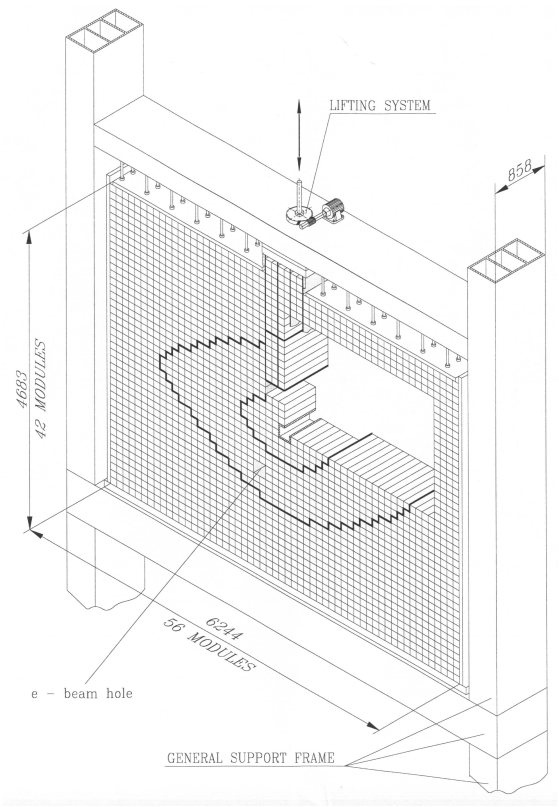

Figure 3.10: Technical drawing of the Electromagnetic calorimeter at HERA-B. The separation of the Inner, Middle and Outer ECAL parts is shown with a black lines.

emphasis in the following is on describing the trigger setup during the run 2000, A full description of the planned trigger scheme for the next runs is given in [18] The trigger system at HERA-B consists of a pre-trigger and a main trigger subdivided into four levels. The pre-trigger provides fast and simple information for the main trigger by considering input from either the ECAL, the Muon system or the high-pt tracker. The high-pt tracker was not operational during the run 2000. While the ECAL pre-trigger searches for clusters characteristic of electrons emanating from J/ψ decays, the Muon pre-trigger looks for a hit coincidence in the pad chambers in two superlayers of the Muon-system. This means that a hit in the MU3 superlayer should be followed by a hit in the MU4 superlayer in the immediate geometrical vicinity. This has been used for selecting candidates from muonic J/ψ decays. By using the pad chambers only, the innermost area of the spectrometer was not covered. But, since the Inner Tracker was not fully operational during the run 2000, the exclusion of this area had no big impact on the general performance.
The first level trigger (FLT) was still under commission during the run 2000 and

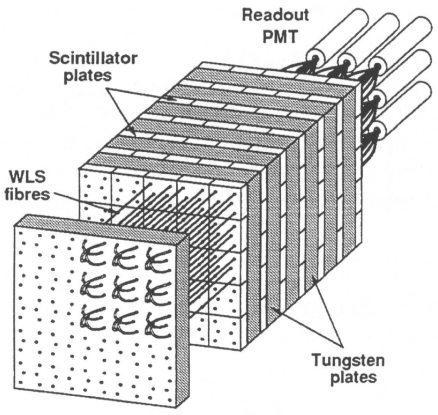

Figure 3.11: Inner ECAL module with 25 cells. Note the sandwiched structure of absorbing material and scintillating plastic.

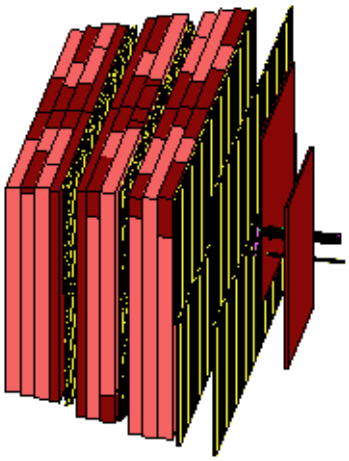

Figure 3.12: Overview of the Muon System showing the superlayer structure and the interleaved absorbers

was used only to count and forward selected candidates, or *seeds*, to the next level in the trigger chain. The Second Level Trigger (SLT) then performed further processing of the seeds. The SLT is a software based trigger consisting of 240 regular PCs. From the seed provided by the pre-trigger, the SLT constructs a geometrically limited area, commonly referred to as a 'Region of Interest' (RoI), in which track candidates are searched for. For muon candidates a threshold on the transverse momentum of the tracks is set to approximately 0.7 GeV. By utilizing OTR information, the trajectory of the candidates are estimated using a hit counting algorithm and a Kalman filter technique [24]. The accepted tracks are projected through the magnet for further comparison with hits in the VDS. If the track candidates are successfully matched to VDS hits, a complete record of the event is made. Digital signal processors are used to buffer the detector data for the time needed to write the necessary sub-detector information to disk.

Period	Run	Target wire	$N_{J/\psi}$	Fraction of total
1.07-24.07	16000-16665	C	1605 ± 51	44%
25.07-17.08	16674-17100	C	946 ± 36	26%
		Ti	1083 ± 44	30%

Table 3.1: The number of reconstructed J/ψ for the respective target wires.

3.9 Data

During the period from 01.07.00 to 17.08.00 HERA-B triggered on $450 \cdot 10^3$ di-muon candidates. Approximately half of the data was collected using one Carbon wire while the two wires were used in the other half; one Carbon and one Titanium. All the di-muon data is mainly triggered using the Second Level Trigger as described in Section 3.8. The quality of the runs vary since the detector was under commissioning during most of the data taking. The understanding of the event reconstruction improved after the run period had ended, and off-line reprocessings of the data samples were performed to update the alignment constants and the calibration of the sub-detectors. The data used in this analysis has been subject to three such reprocessings. A comparison between the second and third reprocessing was performed with respect to J/ψ and χ_c reconstruction [8]. Reconstruction of the χ_c was studied for one good quality run[2] and indicated improvements, especially in the Titanium events. For J/ψ , the mass position was improved by 6 MeV with respect to the table value. Also the ψ' signal was better determined. In the following, only results from the third reprocessing are presented.
Quality checks on the event level is performed in the Sections 4.4 and 5.2 with respect to various subdetector parameters. A detailed investigation of the data quality with respect to the number of hits in each subdetector for the different runs has been performed in [15]. The runs 16501-16527 and 16410-16414 have been excluded from the following analysis due to high number of false tracks in the Second Level Trigger (SLT ghost rate) and an unreasonably high number of hits in the subdetectors.

3.10 Monte-Carlo

A proper simulation of how the detector responds to relevant physics events is essential both for signal optimization as well as determination of acceptance and efficiencies for event selection and reconstruction. A complete simulation of the HERA-B scenario includes generating representative physics events as well as

[2] run16784

detector and trigger simulation.
Generating physics events means in principle to make use of all general knowledge in particle physics to predict the outcome of a special case. The simulation of experimental results is done using sophisticated software and random number generators, and is known as Monte-Carlo simulation. Here the relevant physics are final states of muon-pairs emanating from a J/ψ meson produced either directly or from a subsequent decay of a χ_c state. The simulated interactions which reproduce the HERA-B scenario, are proton-nucleon reactions at $\sqrt{s} = 42.6$ GeV with a rate of 5 MHz corresponding to conditions of the run 2000. The target materials were Carbon and Titanium.
The event generation is done in two steps using two different software packages. The first is the interaction between the incoming beam proton and a target nucleon. This part, handled by the PYTHIA [10] software package, produces the heavy quark pairs of flavours b or c which in turn hadronize. Then an interaction between the proton and the nucleon is simulated at an energy level corresponding to the residue of the previous reaction. This way the simulated physics events capture both high energy physics of heavy quark production as well as the following low energy proton-nucleus interactions. The low energy part is produced using the FRITIOF software package [11].
The low energy kinematics have proven difficult to reproduce in agreement with previous experiments. This has been solved by weighting the events, in effect forcing the generated events to match the kinematics of the E789 experiment [9], a fixed target experiment with an 800 GeV proton beam incident on a gold target. The implementation of the weight function in the event generator used at HERA-B is described in [13]. The lower energy relative to the HERA-B beam of 920 GeV is compensated for by scaling the distributions of the kinematical parameters such as transverse momentum and Feynman-x defined by:

$$x_F = \frac{2P_z}{\sqrt{s}}. \tag{3.2}$$

Here P_z is the longitudinal momentum of the particle and $\sqrt{s}$ the center of mass energy.
The next step is to run the events through a computer simulated HERA-B spectrometer. The geometry of the spectrometer and the interactions in each subdetector are simulated using the GEANT 3 program package [12]. Then a digitization of the electronic signals is performed to give realistic detector precision and to account for hit inefficiencies and defects in parts of the subdetectors. Such defects include for instance dead channels in the ECAL cells. The detector was, as mentioned, under development during the 2000 data taking and not all these changes are included in the simulations. A run from approximately the middle of the run period[3] is chosen as template for the Monte-Carlo detector conditions.

[3] run 16665

When estimating the fraction of J/ψ produced from chi_c, the trigger efficiency plays a minor role since it cancels in the ratios of the cross sections. The trigger efficiency is considered equal for directly produced J/ψ and for J/ψ from χ_c decays. However, a complete simulation of the trigger system is applied including both the MUON pre-trigger and the SLT. All event reconstruction and analysis are done with the same routines for Monte-Carlo as for data.

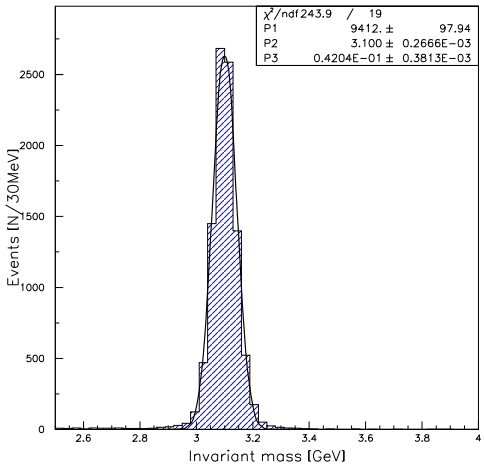

Figure 3.13: The Monte-Carlo J/ψ signal.

Decay channel	Wire	N triggered
direct J/ψ	C	4198
	Ti	1679
$\chi_{c0} \rightarrow \gamma\ J/\psi$	C	110
	Ti	42
$\chi_{c1} \rightarrow \gamma\ J/\psi$	C	724
	Ti	275
$\chi_{c2} \rightarrow \gamma\ J/\psi$	C	1881
	Ti	736
All	C	6913
	Ti	2732

Table 3.2: The Samples of triggered Monte-Carlo events for the different channels.

The Monte-Carlo sample available for this study consist of 9752 triggered J/ψ events, where 9412 ± 98 are reconstructed and fitted to a single Gaussian function.

MC Weight	χ_{c0}	χ_{c1}	χ_{c2}	All χ_c	Direct J/ψ
Default	3.8%	27%	69%	39%	61%
E789	3.8%	26%	70%	39%	61%
CSM	4.0%	14.7%	81%	58%	42%
NRQCD	0.8%	60%	39%	32%	68%

Table 3.3: The distribution between the respective χ_c states and directly produced J/ψ with different Monte-Carlo weighting. The percentages of the χ_{c0} , χ_{c1} and χ_{c2} are relative to the number of all reconstructed χ_c , while the percentages of direct J/ψ and J/ψ produced from χ_c are relative to the total number of reconstructed J/ψ .

(See figure 3.13.) The mean value of the mass of 3.1 GeV agrees with the world average value, and the width of the signal is 42 MeV. The reconstructed J/ψ particles are either directly produced, or produced through radiative χ_c decays. The available Monte-Carlo statistics are summarized in Table 3.2 for Carbon and Titanium events.(The numbers in Table 3.2 are somewhat lower than the total of triggered J/ψ events due to some loss of efficiency in the wire assignment.)
The distribution of events between the different charmonium states χ_{c0} , χ_{c1} and χ_{c2} is model dependent, and it is not obvious that this is well reproduced. The default Monte-Carlo sample is close to the Color Singlet Model (CSM) (see Section 2.2), but is quoted to have no real physical meaning [15]. Implementation of the predicted charmonium production cross sections according to the CSM and the Non Relativistic QCD model is made possible by weighting the events [16]. The distribution of particles between the χ_c states for the default Monte-Carlo after applying the weights from the respective production models, is shown in Table 3.3.

In this chapter the sub-detectors of the HERA-B spectrometer have been presented. The available data and Monte-Carlo samples have also been described. In the next chapter the di-muon invariant mass spectrum is presented, and the J/ψ signal used for the continuation of the analysis is obtained. The first sections in the next chapter will however present the the principle of the measurement and some general features of particle reconstruction.

Chapter 4

Event selection

This chapter begins by presenting the formulas needed for estimating the fraction of J/ψ produced from χ_c . This is followed by a description of the general principles of particle reconstruction. The invariant mass spectrum of the two muons is presented before the signals are discussed. The reconstructed J/ψ particles are then studied in more detail with respect to various parameters, resulting in the J/ψ signal used for the following analysis.

4.1 Measurement

The goal of this diploma thesis is to measure the fraction of J/ψ produced from χ_c decays. The J/ψ meson is reconstructed from a di-muon final state. Hence the reaction under study is

$$\begin{aligned} pN \rightarrow \chi_c X, & \\ \chi_c \rightarrow J/\psi\gamma, & \\ J/\psi \rightarrow \mu^+\mu^-. & \end{aligned} \tag{4.1}$$

Here χ_c includes the three different angular momentum states χ_{c0} , χ_{c1} and χ_{c2} where the value of the angular momentum J=0,1,2 is indicated by the subscripts. (See figure 2.3.) Almost all χ_c decays to J/ψ are radiative, but there is one exception, namely the hadronic decay of the χ_{c2} state $\chi_{c2} \rightarrow J/\psi\ \pi^+\pi^-\pi^0$.The branching ratio for this decay channel is however less than 1.5% [33] and is negligible compared to the radiative decays (see Table 2.1). Both the χ_c and the J/ψ are assumed to be produced promptly, meaning that any contribution from b-quark decays are negligible. For a sample of approximately 3000 J/ψ this should be a valid assumption, as it is expected to contain less than one event of the $b \rightarrow J/\psi\ X$. This rather crude estimate is done using the numbers for the J/ψ and $b\bar{b}$ cross-sections and the branching ratio $Br(b\bar{b} \rightarrow J/\psi X)$ re-estimated from the published E789 values to match the HERA-B scenario [17]. However, for a larger sample, expected to be collected by HERA-B in the run 2002, the

b-quark contribution will have to be accounted for.
To measure the fraction of J/ψ from χ_c is, in simple terms, to estimate the fraction of J/ψ particles produced from χ_c decays and the total number of J/ψ particles. In common terms of particle physics this fraction is given by

$$F_{\chi_c}^{J/\psi} = \frac{\sum_{J=0}^{2} \sigma(\chi_{cJ}) \cdot Br(\chi_{cJ} \to J/\psi\gamma)}{\sigma(J/\psi)} \tag{4.2}$$

where the sum extends over the three angular momentum states. The production cross sections for the indicated χ_c states and the J/ψ are given by $\sigma(\chi_{cJ})$ and $\sigma(J/\psi)$ respectively. The cross sections for the χ_c particles are given by

$$\sigma(\chi_{cJ}) = \frac{N_{\chi_{cJ}}}{\mathcal{L} \cdot \varepsilon_{\chi_{cJ}}^{tot} \cdot Br(\chi_{cJ} \to J/\psi\gamma) \cdot Br(J/\psi \to \mu^+\mu^-)}, \tag{4.3}$$

$$\varepsilon_{\chi_{cJ}}^{tot} = \varepsilon_{J/\psi}^{tot} \cdot \varepsilon_\gamma. \tag{4.4}$$

Here $N_{\chi_{cJ}}$ gives the number of observed χ_c particles, $\mathcal{L}$ is the luminosity and $\varepsilon_{\chi_{cJ}}^{tot}$ is the total efficiency for the χ_c given by the product of the efficiency for reconstructing a J/ψ multiplied by the efficiency for reconstructing the χ_c . The corresponding J/ψ cross section is given by

$$\sigma(J/\psi) = \frac{N_{J/\psi}}{\mathcal{L} \cdot \varepsilon_{J/\psi}^{tot} \cdot Br(J/\psi \to \mu^+\mu^-)} \tag{4.5}$$

where $N_{J/\psi}$ is the number of observed J/ψ particles and the other variables are as described above.
By substituting the equations 4.3, 4.4 and 4.5 into equation 4.2 the following expression is obtained

$$F_{\chi_c}^{J/\psi} = \frac{\sum_{J=0}^{2} N_{\chi_{cJ}}}{N_{J/\psi} \cdot \varepsilon_\gamma}. \tag{4.6}$$

Here N_{χ_c} and $\sum_{J=0}^{2} N_{\chi_{cJ}}$ are the numbers of J/ψ and χ_c observed in the data sample, while the photon efficiency ε_γ is found from Monte-Carlo. Estimation of ε_γ is done by considering a Monte-Carlo sample of J/ψ from χ_c decays only and measuring the number of χ_c reconstructed with the same algorithms as those used for data.

4.2 Particle reconstruction

A short lived particle is reconstructed from its decay products by calculating their total invariant mass. The invariant mass is convenient to use because it is

Lorenz invariant, *i.e* it has the same value in any reference frame. Using natural units, the invariant mass of n decay products is given by

$$W^2 = (\sum_n E_n)^2 - (\sum_n \vec{p}_n)^2 \tag{4.7}$$

where E_n is the energy and $\vec{p}$ the momentum of the n-th decay product. By energy and momentum conservation and substitution of $E^2 = M^2 + p^2$ into eq. 4.7, it is seen that the invariant mass of the decay products is similar to the rest mass M of the decayed particle. Hence the mass of a particle calculated from the decay $X \to \mu^+\mu^-$ is given by

$$M_X = \sqrt{(E_{\mu^+} + E_{\mu^-})^2 - (\vec{p}_{\mu^+} + \vec{p}_{\mu^-})^2} \tag{4.8}$$

$$= \sqrt{2(m_\mu^2 + E_{\mu^+}E_{\mu^-} - \vec{p}_{\mu^+} \cdot \vec{p}_{\mu^-})}. \tag{4.9}$$

The reconstruction of particles from two muons is done from tracks identified by the SLT as muons. The analysis is done using C/C++ and FORTRAN code written in the framework of ARTE, the HERA-B Analysis and reconstruction tool [25] and PAW (Physics Analysis Workstation). The GROVER (Generic Reconstruction of VERtices) package [26] is used for vertex position determination. By selecting muon-pairs with equal or opposite charges, the invariant mass spectrum is divided into to sub-samples, where of course only the opposite sign muons give particle resonances. The analysis in the following section is performed to display the characteristics of the di-muon spectrum. The runs from 16008 to 16927 have been used, which is less than the full statistics. A more detailed analysis on the full data sample is performed in section 4.4. The di-muon invariant mass spectrum displayed in the next section show signals from the the particles
ρ (770 MeV),ϕ (1020 MeV), J/ψ (3096 MeV) and ψ' (3686 MeV).

4.3 The di-muon spectrum

The invariant mass spectrum of identified pairs of muon tracks is shown in figure 4.1. The histogram shows the invariant mass reconstructed from opposites charged muons with a darker inset showing the corresponding spectrum from muons with equal charges. None of the distributions have been scaled, the entries correspond to the number of track pairs found in the data sets. Between 0.8-1.2 GeV there are enhancements due to the particles ρ and ϕ. Some properties of these particles are compiled in table 4.1. A close-up on this mass range is depicted in figure 4.2. With a mass difference between the ρ and ω of only 12 MeV, these particles are not cleanly separated. But since their relative widths

are of 150.7 MeV and 8.44 MeV for the ρ and ω respectively, separation is possible by fitting two Gaussians with different widths. To isolate the ω signal is interesting because the branching ratio of the decay $\omega \to \mu^+\mu^-$ only has one measurement by the ALEPH Collaboration [27]. An additional measurement of ω in the muon channel at HERA-B will therefore give an important contribution to the world statistics. In figure 4.2 the distribution has been fitted with one Gaussian function for the ω-ρ and one for the ϕ in addition to an exponential function to describe the background. In total 671 ± 90 ω/ρ particles and 189 ± 45 ϕ particles have been reconstructed. An analysis is currently ongoing at HERA-B to extract the ω signal.

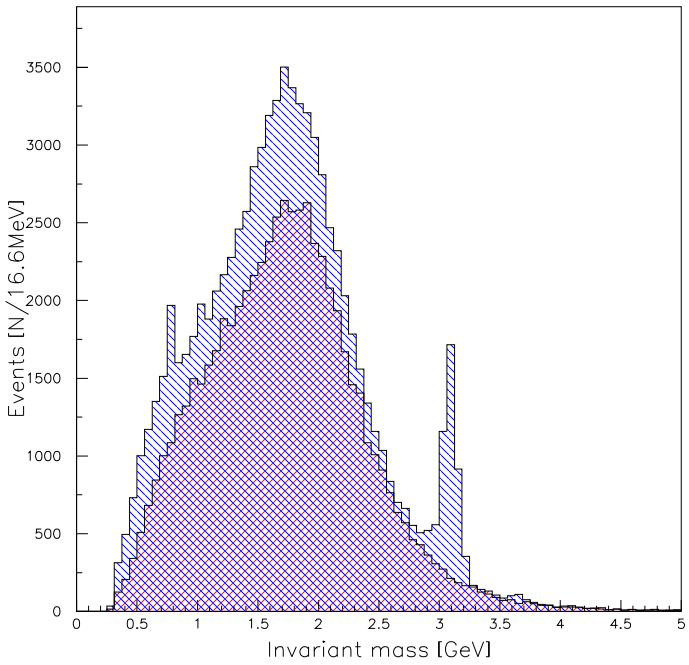

Figure 4.1: The full di-muon spectrum. The histogram shows the invariant mass of muons with opposite charge with a clear J/ψ signal at $\sim$3.1 GeV. The darker inset shows the invariant mass of muon pair with equal charges.

Following the di-muon spectrum further, there is an interval from approximately 1.2 GeV to 2.8 GeV where no particle resonances are visible. This interval contains many hadrons and their excited states, but none of these are reconstructed here. Then a clear J/ψ signal is visible at approximately 3.1 GeV followed by the ψ' at approximately 3.7 GeV. In figure 4.3 the J/ψ and ψ' resonances are fitted with Gaussian functions with the background described by an

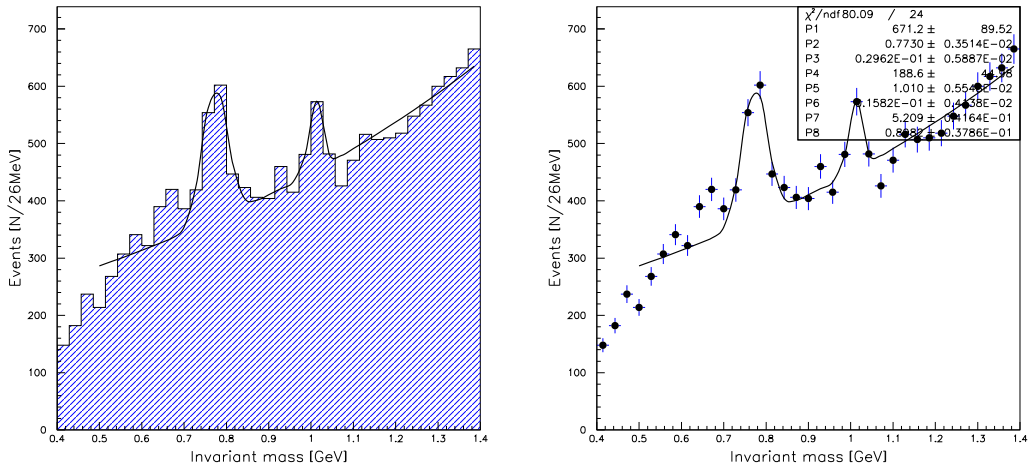

Figure 4.2: The low mass resonances of the di-muon invariant mass spectrum. The histogram is fitted with two Gaussians for the signals and one exponential. The ω and the ρ are not separated here.

Particle	Mass [MeV]	$\Gamma_{\mu^+\mu^-}/\Gamma_{tot}$ [%]	Width [MeV]
ρ	769.9 ± 0.8	$(4.60 \pm 0.28) \cdot 10^{-5}$	150.4 ± 1.6
ω	782.57 ± 0.12	$(9.0 \pm 2.9_{stat} \pm 1.1_{syst}) \cdot 10^{-5}$*)	8.44 ± 0.09
ϕ	1019.417 ± 0.014	$(2.9 \pm 0.4) \cdot 10^{-4}$	4.458 ± 0.032
J/ψ	3096.88 ± 0.04	6.01 ± 0.19	$(87 \pm 5) \cdot 10^{-3}$
ψ'	3686.00 ± 0.09	$(7.7 \pm 1.7) \cdot 10^{-3}$	$(277 \pm 31) \cdot 10^{-3}$

Table 4.1: Properties of the particles from the low mass part of the di-muon spectrum. All values are from [33], except *) which is from [27]

exponential function. Some of the background under the signal is due to misidentified muons. By using particle identification from subdetectors like the RICH or the MUON system this background can be reduced as shown in the next section. The remaining background may come from muon tracks which are not from a X$\rightarrow \mu^+\mu^-$ decay or just tracks that are not well reconstructed.
Here there are 2703 ± 61 reconstructed J/ψ mesons with the mean of the J/ψ mass at 3.088 ± 0.0014 GeV. The mass of the J/ψ is shifted by 8 MeV compared to the world average (see table 4.1). The width of the signal is 57 MeV, which is 15 MeV larger than what is expected from Monte-Carlo (see Section 3.10, figure 3.13). (This is the experimental width and should not be confused with the intrinsic width given in table 4.1.)
The ψ' signal contains 75 ± 17 particles with a mean at 3.656 ± 0.018 GeV. This is 30 MeV lower than the world average. The width for the ψ' is found to be

62 MeV, which is in reasonable agreement with the measured width of the J/ψ . There is no obvious reason why the ψ' has a greater mass shift than the J/ψ , but it could be due the lower statistics of the ψ' signal. However, within the error of 18 MeV, the mass shift of the ψ' is close to the 8 MeV shift seen for the J/ψ .

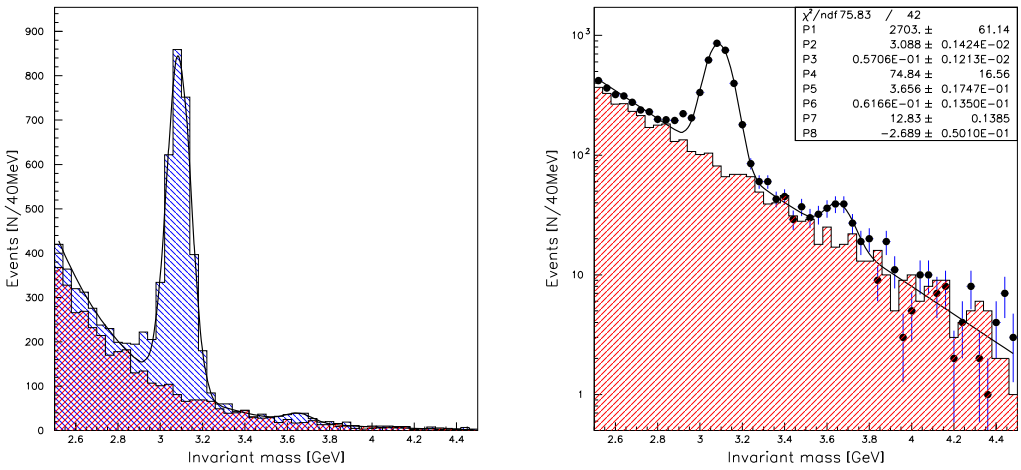

Figure 4.3: The J/ψ and ψ' signals in the di-muon spectrum. The the darker/shaded histograms show the muons with equal signs. The right histogram is plotted with a logarithmic y-axis for better visualization of the ψ' signal.

4.4 J/ψ signal

In this section some properties of the two muons used for J/ψ reconstruction is studied. The goal is to obtain a cleaner J/ψ sample by removing badly reconstructed muon tracks. This is not an optimization with respect to signal to background ratio, but is meant to remove events with nonphysical or unreasonable values of the studied parameters. The emphasis is therefore on retaining a high efficiency for the J/ψ reconstruction rather than reducing the background in the J/ψ signal. When reconstructing the χ_c by adding a photon to the J/ψ the main contribution to the background is not expected to be from the muons, but rather from the photon combinatorics. The parameters which have been studied for the muons are:

-Probability of vertex reconstruction
-Transverse momentum
-Muon chamber likelihood
-RICH likelihood

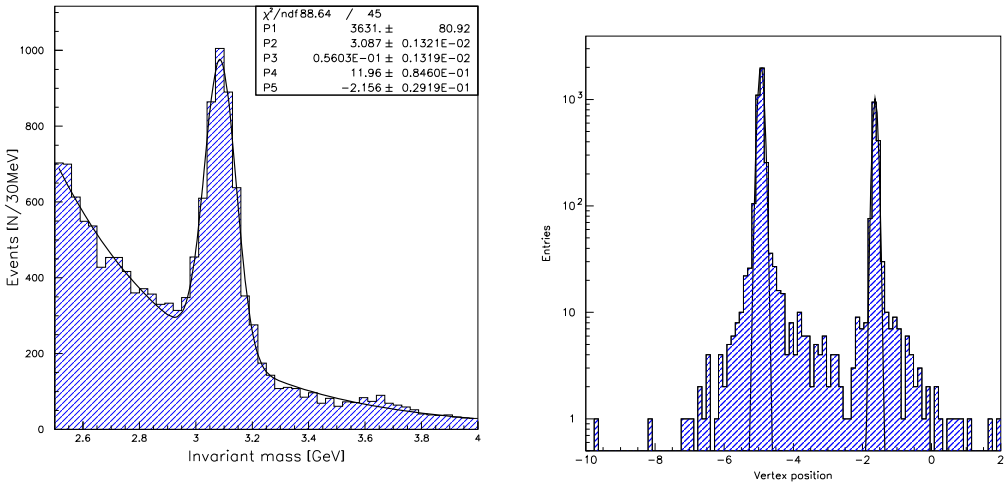

Figure 4.4: The 'raw' J/ψ spectrum (left) and the vertex distribution between the Carbon and the Titanium wire (right). The vertex distribution has logarithmic scale on the y-axis.

The distributions of the di-muon invariant mass have been fitted with a Gaussian function for the J/ψ resonance and an exponential function for the background. When the different muon properties are studied, events within two standard deviations of the mean of the fitted Gaussian are chosen. Efficiencies of the cuts are given as the percentage of reconstructed particles after the cuts with respect

to the number of reconstructed particles before the cuts.
The starting point for the analysis is the invariant mass distribution of SLT-triggered muon-pairs with opposite charges. The runs 16410-16414 and 16501-16527 have been removed as described in Section 3.9. Because it is improbable to have more than one J/ψ per event at HERA-B, any events with two or more reconstructed muon-pairs within two standard deviations of the J/ψ signal are removed. The remaining sample will be referred to as the 'raw' J/ψ sample. This sample yields 3631 ± 81 reconstructed J/ψ mesons with the mean of the invariant mass at 3.087 GeV and a width of 56.0 MeV (see figure 4.4).

4.4.1 Vertex position

The vertex positions in the Z-direction, parallel to the beam, show the two positions of the two target wires: The 'below one' made of carbon positioned at $Z_C = -4.94$ and the 'inner two' at $Z_{Ti} = -1.63$. The wire assignment of the muon pairs is set to $(Z_C \pm 0.39)$ cm and $(Z_{Ti} \pm 0.34)$ cm for the two wires. The efficiency for the wire assignment is 99.7% with respect to the 'raw' spectrum and results in 2539 ± 63 J/ψ mesons from the Carbon wire and 1083 ± 44 from the Titanium wire (see figure 4.5). The efficiencies in the following are relative to the number of reconstructed J/ψ particles after wire assignment.

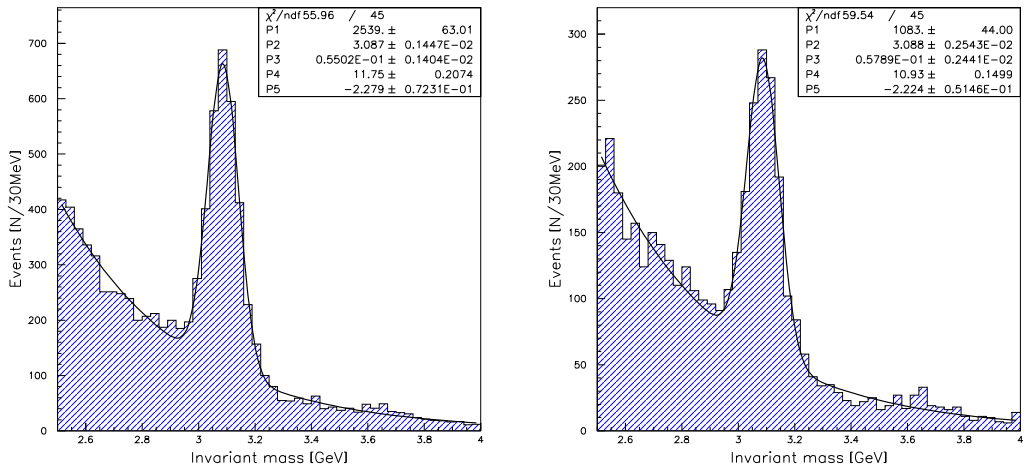

Figure 4.5: The distributions after wire assignment yield 2539 and 1083 reconstructed J/ψ mesons for the Carbon (left) and Titanium (right) wire respectively.

4.4.2 Vertex probability

The vertex probability is calculated from the χ^2 distribution of the fitted vertices. The distribution of the vertex probabilities for the reconstructed J/ψ mesons (See figure 4.6) show a high number of entries with values close to zero. This feature is not present in the corresponding distribution for Monte-Carlo simulated events. These events are therefore considered corrupt and are removed from the sample with a cut at $P_{vtx} > 0.005$. The efficiency of this cut is 92.9%. After this cut the vertex probability is reasonably well described by the Monte-Carlo.

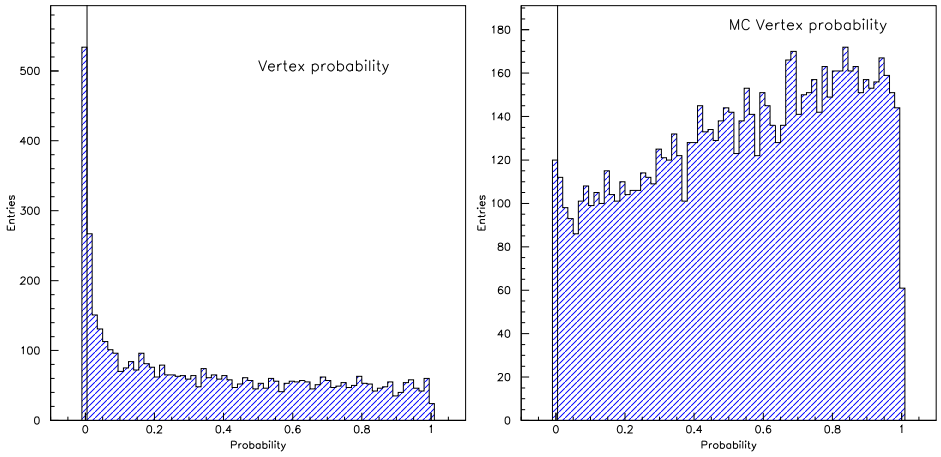

Figure 4.6: Vertex probability for data (left) and Monte-Carlo (right). The distribution from data shows a high number of muon-tracks with vertex probability close to zero.

4.4.3 Transverse momentum

The transverse momentum of a particle is defined as

$$P_\perp = \sqrt{p_x^2 + p_y^2} \tag{4.10}$$

where p_x and p_y are the momentum projections in the x and y direction respectively. The transverse momentum of the two muons is already considered in the SLT track selection algorithms. The SLT opens a search window in the Outer Tracker for tracks with transverse momentum higher than 0.7 GeV. This is not a strict cut, so muons with lower values still have a chance to pass the trigger. However, the transverse momentum distribution show that all the tracks contributing to the raw J/ψ have transverse momentum higher than 0.5 GeV (see figure 4.7). No further cuts on this property is therefore considered necessary. The transverse

momentum of the muons is well described by the Monte-Carlo after weighting the events according to the E789 experiment as described in Section 3.10.

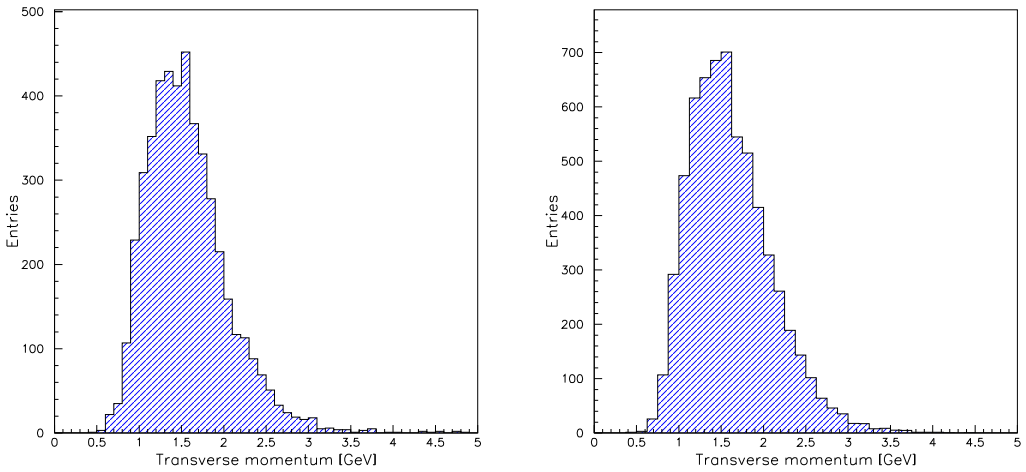

Figure 4.7: Transverse momentum distributions for data (left) and Monte-Carlo (right). The distributions agree well and show no tracks with nonphysical values.

4.4.4 RICH likelihood

The HERA-B Ring Imaging Cherenkov Counter has been constructed to separate kaons from protons and pions. Still this may be useful for identifying muons. There are two different hypotheses for estimating RICH likelihoods at HERA-B: *riter* and *rise*. The *riter* hypothesis [34] is based on an iterative method of sorting the photon hits. The *rise*, or ring-search, hypothesis uses a 2D ring superposition around each photon to find the Cherenkov ring center and radius[35]. The distributions of the RICH likelihoods for the two muons (figure 4.8) show only few entries with values close to unity. This is because the RICH is unable to cleanly separate muons from charged pions due to their small mass difference of ca. 34 MeV. An attempt to cut at the lowest values ($\ell_{rise,riter} > 0.01$) of the *riter* and *rise* muon likelihoods gives efficiencies of 79.8% and 54.2% respectively. Here this efficiency is considered too low, and combined with the fact that muons are not well identified by the RICH, it is decided not to use a cut on the RICH-likelihood in the following analysis.

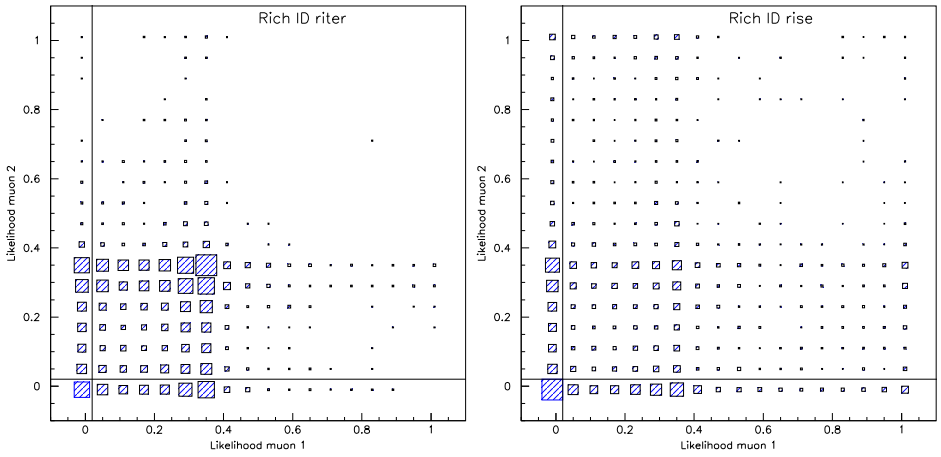

Figure 4.8: The Rise (left) and Riter Riter (right) RICH likelihoods.

4.4.5 Muon-chamber likelihood

The muon-chamber likelihood is the particle identification provided by the MUON system. The distribution for the muon-chamber likelihood (figure 4.9) shows that most muon-pairs have likelihoods close to unity. However, some of the tracks also have likelihoods close to zero, and these are avoided by a cut at $\ell_\mu > 0.1$. This results in an efficiency of 83.2% Although this cut lowers the availible statistics it is considered useful, also when comparing with Monte-Carlo where the zero-likelihood entries are missing.

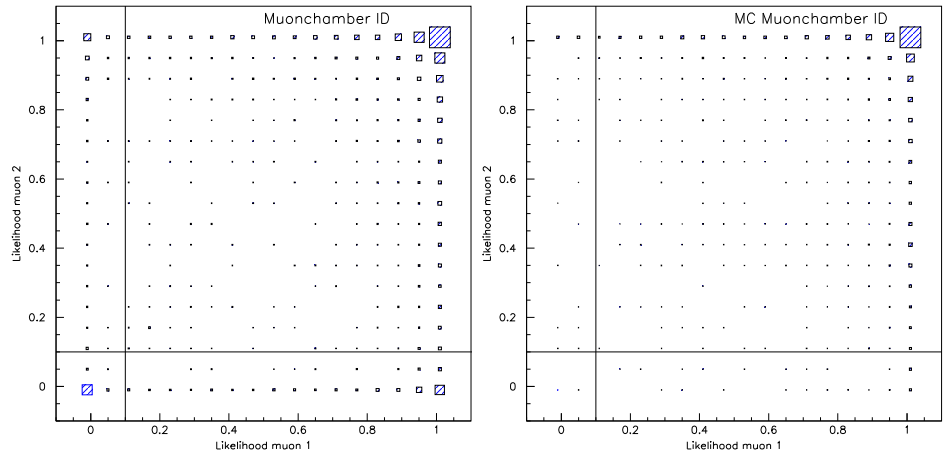

Figure 4.9: The muon-chamber likelihoods for muons, data (left) and Monte-Carlo (right).

4.4.6 Summary

Having investigated some properties of muon-tracks the following cuts on the muon-tracks are chosen:

Vertex-probability:	$P_{vtx} > 0.005$
Muon-chamber likelihood:	$\ell_\mu > 0.1$

The resulting signals are shown in figure 4.10 and yield 1795 ± 50 and 890 ± 37 reconstructed J/ψ particles assigned to the Carbon and Titanium wire respectively. The total efficiency for both of the applied cuts is 71% for the Carbon-wire and 82% for the Titanium wire. The efficiencies are, as noted earlier, the percentage of the remaining particles after the cuts are applied with respect to the number of particles before the cuts.

In this chapter a presentation of the principles behind the measurement of F_{χ_c}

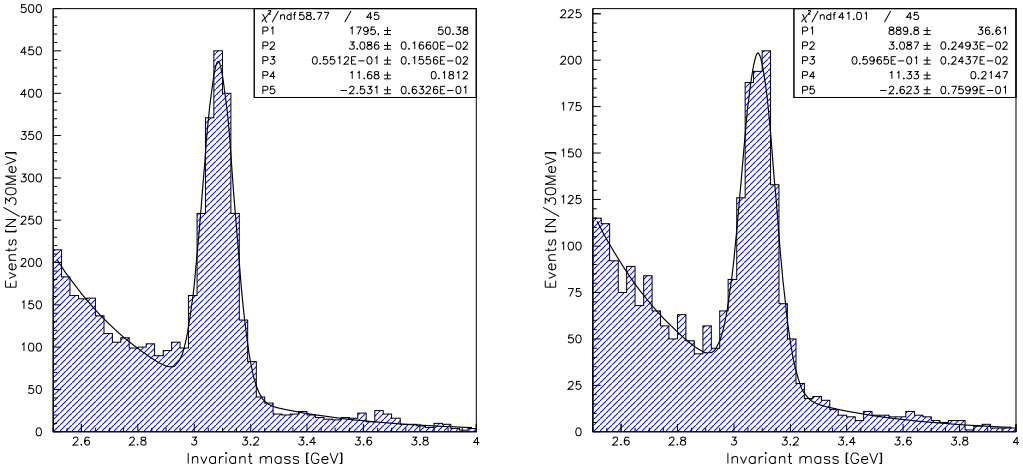

Figure 4.10: The J/ψ signals after the cuts on vertex probability $P_{vtx} > 0.005$ and muon-chamber likelihood $\ell_\mu > 0.1$. The signals yield 1795 ± 50 and 890 ± 37 reconstructed J/ψ particles for the Carbon and Titanium wire respectively.

has been given. The calculation of the invariant mass of the muon pairs is described and their invariant mass spectrum has been presented. This spectrum showed the particles ω/ρ, ϕ, J/ψ and ψ' . The properties of the reconstructed J/ψ have been studied for events from Carbon and Titanium wires, and the resulting signals give the starting point for the analysis in the next chapter.

Chapter 5

Analysis

The J/ψ was reconstructed in the last chapter giving 1795 ± 52 and 890 ± 37 reconstructed J/ψ particles from Carbon and Titanium interactions respectively. This sample gives the starting point for the the analysis presented in this chapter. First the method for the analysis is presented including χ_c reconstruction, background description and the procedure of fitting the signal. A clean χ_c signal is obtained from the Monte-Carlo sample, allowing comparison of photons from χ_c decays with other reconstructed clusters. Then the estimation of the significance of the χ_c signal is presented. This is followed by the optimization of the χ_c signal where the number of reconstructed χ_c particles and significance of the signal is studied for the respective cuts. The plots used for this optimization are presented in Appendix A for Monte-Carlo and in Appendix B for data.

5.1 Analysis method

The invariant mass of J/ψ γ is given by

$$M_{J/\psi\gamma} = \sqrt{M_{J/\psi}^2 + 2E_\gamma E_{J/\psi} - 2\vec{p}_\gamma \vec{p}_{J/\psi}} \tag{5.1}$$

where $M_{J/\psi}$ is the reconstructed invariant mass of the J/ψ , E is the energy and $\vec{p}$ the momentum vector for the indicated particles. This expression is found by entering the photon energy and J/ψ momentum and energy into eq.4.7 with $E_{J/\psi}^2 = M_{J/\psi}^2 + p_{J/\psi}^2$ and $E_\gamma = p_\gamma$. Because $M_{J/\psi}$ has a normal distribution, the invariant mass of the identified J/ψ particles is not constant. To study the $M_{J/\psi\gamma}$ spectrum would therefore not give a precise signal determination. Instead the mass difference given by

$$\Delta M = M_{J/\psi\gamma} - M_{J/\psi}. \tag{5.2}$$

is studied, thereby canceling the effect of the distributed $M_{J/\psi}$ values. Studying ΔM spectrum is not equivalent to studying the photon energy alone, as can be

seen from eq.5.1 where the J/ψ mass does not cancel. Another possible approach is to constrain the invariant mass of the identified J/ψ mesons to the table value, and then study the $M_{J/\psi\gamma}$ spectrum. Here the former method is chosen because it is considered simpler. The mass differences between the χ_{c0} , χ_{c1} and χ_{c2} and the J/ψ are summarized in Table 2.1.

5.1.1 Background description

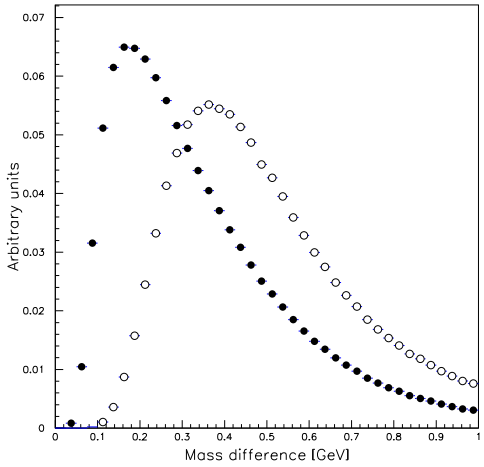

Figure 5.1: The mixed background distributions with energy cut of 2.0 GeV (black points) and 6.0 GeV (open points).

To understand the background is fundamental in any particle physics analysis. The background description is the reference which constitutes the signal by showing where there is none. To describe the background under the χ_c signal, each identified J/ψ is combined with photons from different events with similar event characteristics. This method, from now on referred to as 'event mixing', has the advantage of giving the background shape directly. The fit of the signal with background is then done using a minimum of parameters. The parameters needed are the three parameters of the Gaussian, *i.e.* width, mean position and number of entries in the signal, plus a scaling factor to adjust the background. Attempts to fit the background with either three Gaussians or a ninth order polynomial have not been successful, although the latter method is used successfully in [30]. Other strategies for describing the background could include using sideband events outside the J/ψ mass region, as well as equal sign muons. These methods will however not be used here.

Examples of the background distributions obtained using event mixing is shown in figure 5.1. In general it is not desirable to have the peak of the background close to the signal peak. In figure 5.1 it is seen that the distribution with cluster energy larger than 6.0 GeV peaks close to the mass difference of χ_c and J/ψ . The cuts on cluster energy should therefore be moderate enough to avoid the peaking close to signal region.

5.1.2 The χ_c signal-fit

The χ_c signal in the mass difference spectrum of the χ_c and the J/ψ is fitted with a Gaussian function. The three parameters of the Gaussian give the number of particles, the mean and the variance, or width, of the signal. If however some of the fit parameters give unphysical values or values that are unrealistic with respect to detector performance, corrections can be made by constraining or fixing these parameters. Fixing a parameter requires good understanding of the detector and a realistic Monte-Carlo simulation because the value of that parameter must be known prior to the measurement. The strategy used for fitting the χ_c signal is fixing the width of the Gaussian to the value found from a clean Monte-Carlo signal. Since there is no obvious way of extracting the correct χ_c photon from the digitized Monte-Carlo, a clean signal is obtained by matching the generated kinematical parameters of the χ_c photons with the digitized and reconstructed clusters. This is done by comparing the impact point of the generated photon in the ECAL with the positions of the clusters. The coordinates of the impact points are found from

$$(x_\gamma, y_\gamma) = (\frac{p_{\gamma x}}{p_{\gamma z}} R_z, \frac{p_{\gamma y}}{p_{\gamma z}} R_z) \tag{5.3}$$

where $p_{\gamma x,y,z}$ give the indicated momentum components of the Monte-Carlo generated value of a photon from χ_c . R_z is the distance in z, parallel to the beam, from the reconstructed vertex to the cluster in the ECAL. The vertex position is found from the J/ψ muon tracks reconstructed with procedures similar to those used for data. The angle between the generated photons and the reconstructed cluster has also been studied, and is calculated from

$$cos\theta = \frac{\vec{p}_\gamma \cdot \vec{p}_{\gamma reco}}{|\vec{p}|_\gamma \cdot |\vec{p}|_{\gamma reco}} \tag{5.4}$$

with $\vec{p}_{\gamma reco}$ as the momentum of the reconstructed cluster and $\vec{p}_\gamma$ as the total momentum of the generated photon.
The distance between the calculated impact point and the cluster position (D_{clus}) is plotted as a function of the angle in figure 5.2 and shows that they are strongly correlated. Most photons follow a close to parallel trajectory because p_z dominates the total momentum. Restricting D_{clus} is therefore a more efficient way to

isolate the clusters than restricting the angle. However, the information from the angle is used as a cross check. Care has been taken not to cut too hard on D_{clus} to avoid any bias on the energy or transverse momentum of the clusters. The

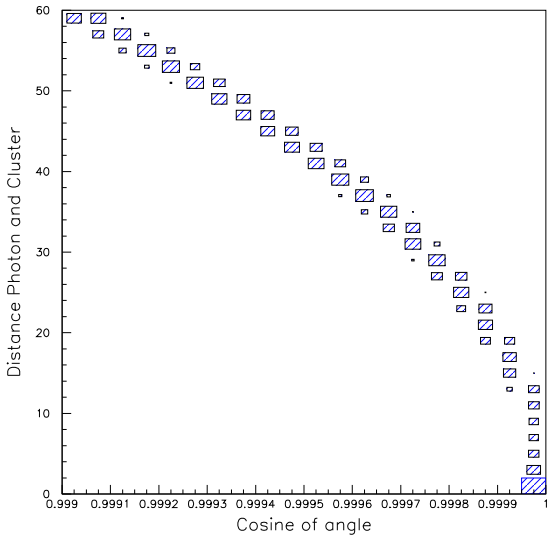

Figure 5.2: Distance between the positions of the reconstructed cluster and the calculated impact point of the generated cluster as a function of the angle between their directions.

generated energy of the χ_c photons is compared to the energy of the reconstructed clusters as a function of D_{clus} in figure 5.1.2. It is seen that for $D_{clus} < 5.0$ cm the energies correspond well while for $D_{clus} < 1.0$ cm, a discrepancy is seen in the low energy range. Hence the low energy clusters are lost if D_{clus} is restricted below 1.0 cm. Similarly, if any further restrictions on the angle is done after the restriction $D_{clus} < 5.0$ cm, the low energy spectrum is not reproduced by the reconstructed cluster (see figure 5.5). The $P_\perp$ spectra for the generated photons and the reconstructed clusters for D_{clus} <5.0 cm agree well (see figure 5.6), indicating that the clusters from χ_c are identified with no kinematical bias.

The resulting invariant mass distributions of $M_{J/\psi\gamma}$ with $D_{clus} < 50$ cm and $D_{clus} < 5.0$ cm are shown in figure 5.3. The resulting width of the Gaussian without any cuts on the clusters is 47 MeV. The width used for the χ_c fits in data, is found after all the cuts on the events and the clusters are applied. This is discussed in Section 6.1.1. For now the Monte-Carlo identified χ_c signal is used to compare the properties of reconstructed clusters from χ_c decays with other reconstructed clusters.

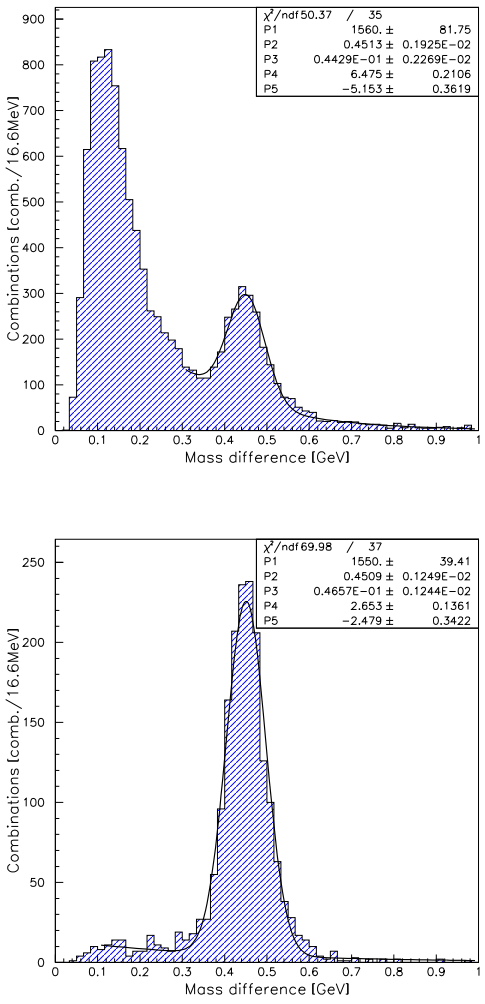

Figure 5.3: Distributions for Monte-Carlo matched clusters with distance cut of 50 cm (top) and 5.0 cm (bottom). Both distributions are fitted with a Gaussian function for the signal and an Exponential function for the background.

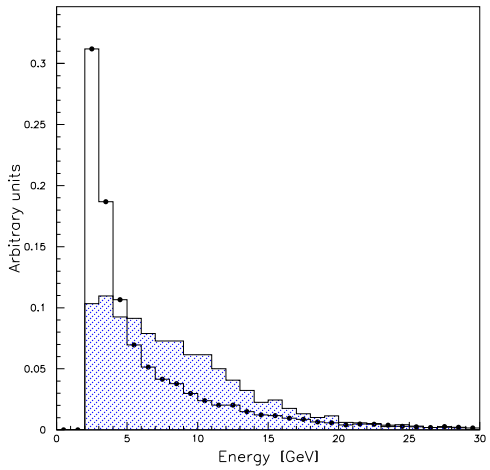

D_{clus}<**50 cm**

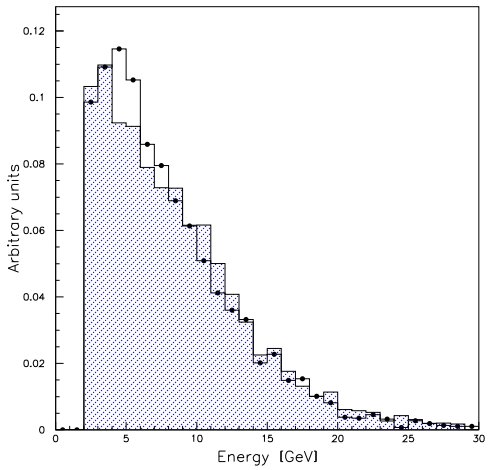

D_{clus} <5 cm

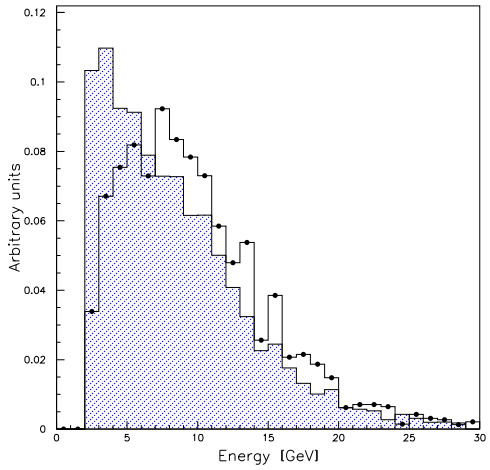

D_{clus}<1 cm

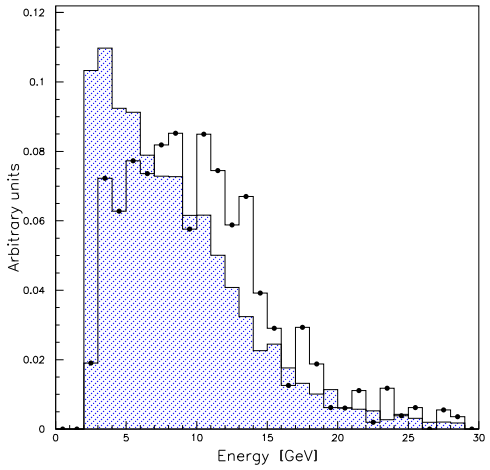

D_{clus}<0.5 cm

Figure 5.4: Comparison of energy distributions for generated photons from χ_c decays (shaded histograms) and clusters with different constraints on the distance between the calculated impact point of the generated cluster and the actual cluster position (D_{clus}) (open histograms marked with points). It is seen that for D_{clus} <1.0 cm and D_{clus} <0.5 some low energy clusters are lost

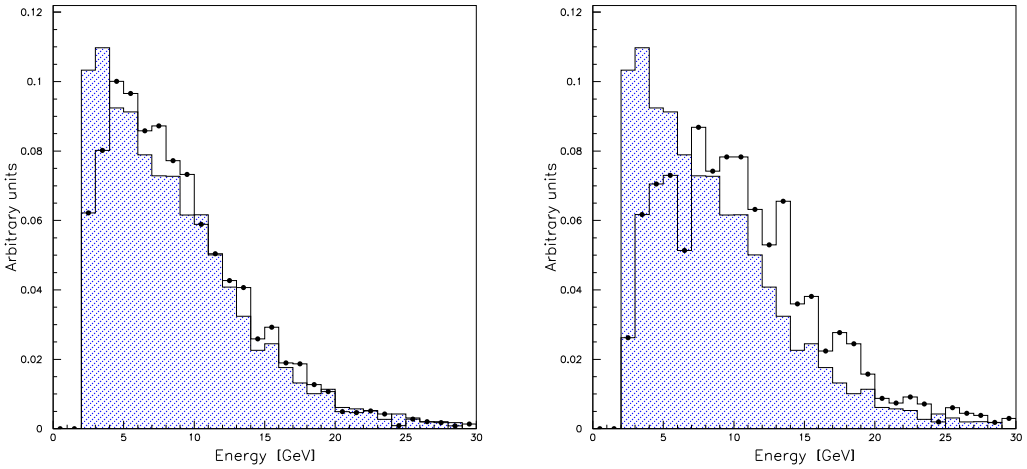

Figure 5.5: Comparison of energy distributions for generated photons from χ_c decays (shaded histograms) and clusters with $D_{clus} < 5$ cm with additional constraints on $cos\theta$ (open histograms). The distributions have $(1 - cos\theta) < 10^{-6}$ (left) and $(1 - cos\theta) < 10^{-7}$ (right).

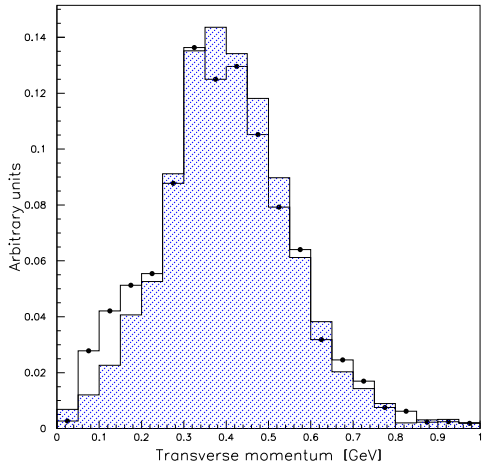

Figure 5.6: Comparison of transverse momentum distributions for generated photons from χ_c decays (shaded histogram) and matched clusters (open histograms).

5.1.3 Significance

The significance of the signal is commonly defined as

$$f(S,B) = \frac{S}{\sqrt{B}}. \tag{5.5}$$

Here S is the number of entries in the signal and B the number of entries in the background below the signal. The significance is calculated by counting the events within three standard deviations around the mean of the signal. This corresponds to 99.7% of the entries in the fitted signal. The error on $f(S,B)$ is given by the differential:

$$df(S,B) = \frac{\partial f}{\partial S}dS + \frac{\partial f}{\partial B}dB \tag{5.6}$$

Including errors eq. 5.5 then becomes

$$\begin{aligned} f(S,B) \pm df(S,B) &= \tfrac{S}{\sqrt{B}} \pm \left(\left(\tfrac{\Delta S}{\sqrt{B}} \right)^2 + \left(\tfrac{S \cdot \Delta B \sqrt{B}}{2B^2} \right)^2 \right)^{\frac{1}{2}} \\ &= \tfrac{S}{\sqrt{B}} \pm \left(\tfrac{\Delta S^2}{B} + \tfrac{S^2 \cdot \Delta B^2}{4B^3} \right)^{\frac{1}{2}}. \end{aligned} \tag{5.7}$$

The error in eq. 5.7 is dominated by the second term $\frac{\Delta S^2}{B}$ because the denominator in $\frac{S^2 \cdot \Delta B^2}{4B^3}$ brings this term close to zero because B^4 is large in the χ_c plots. Hence the significance with error can be expressed as

$$\frac{S}{\sqrt{B}} \pm \frac{\Delta S}{\sqrt{B}} \tag{5.8}$$

where the error ΔS given by the fit procedure. The error in the significance for the fitted χ_c signals is found to be constant at approximately 0.9 for both Monte-Carlo and data.

5.2 Signal optimization

The starting point for the following analysis is given by the J/ψ sample described in the previous section. This means that 1795 ± 50 J/ψ mesons from Carbon wire interactions and 890 ± 37 J/ψ particles from Titanium are available for the χ_c reconstruction. This number will be somewhat reduced in the following as some of the cuts introduced for the $J/\psi + \gamma$ reconstruction will not only affect the photons, but the full event. This is the case for the occupancy cuts which will be discussed in this section. Also a study of the cluster characteristics will be presented. The other parameters studied include the energy and transverse momentum of the clusters together with parameters connected to the energy distribution of the reconstructed clusters. But firstly more general properties of the Electromagnetic Calorimeter (ECAL) relevant to the analysis will be investigated.

5.2.1 ECAL characteristics

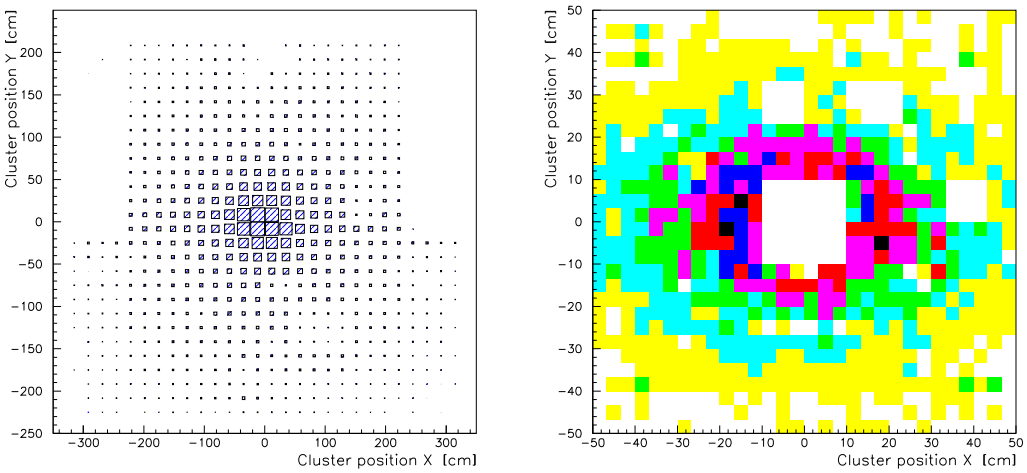

Figure 5.7: Positions of clusters in the full ECAL (left) and for a close-up on the area close to the beam pipe, where the darker shades indicate higher occupancy.

The geometrical distribution of the clusters in the ECAL is shown in figure 5.7. It is seen that the area close to the beam pipe is densely populated with clusters. The clusters in this area tend to overlap and may therefore not be well reconstructed. Also, since the main contribution to the background is from photon combinatorics, the exclusion of the innermost area of the ECAL may improve the signal significance.

Therefore a geometrical cut corresponding to the ellipse

$$\frac{x^2}{4} + y^2 > 484 \tag{5.9}$$

is applied to remove the area closest to the beam pipe. Here x and y are the positions of the clusters in the ECAL..
As mentioned in Section 3.6, the outer part of the ECAL was still under construction during the ECAL calibration. The geometrical partition of the ECAL is shown in figure 5.8. Because the calibration of the Outer ECAL is not on the same level as the Inner and Middle parts, results with and without the Outer ECAL will be discussed.

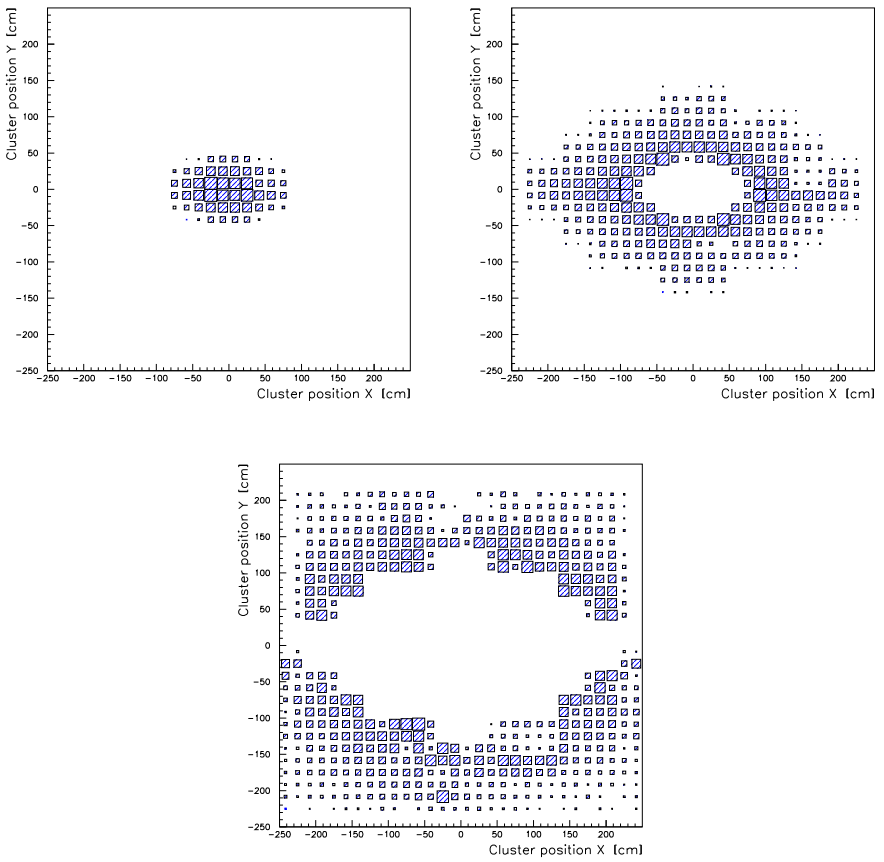

Figure 5.8: Distribution of clusters within the different ECAL parts Inner (top, left), Middle (top, right) and Outer (low). The size of the boxes shows the occupancy relative to each part.

5.2.2 Energy and transverse momentum

The energy E_{clus} of an ECAL cluster is defined as the total energy deposited in that cluster. The transverse momentum $P_\perp$ is defined in eq. 4.10. E_{clus} and $P_\perp$ of the ECAL clusters are correlated parameters: if E_{clus} is large then $P_\perp$ is likely to be large and vice versa. To cut on both may therefore not be useful. The correlation is however not obvious, a cut on E_{clus} will not give a distinct restriction of $P_\perp$ (See figure 5.9.). Therefore both parameters have been studied separately.

The motivation for imposing cuts on the energy of the ECAL-clusters is twofold.

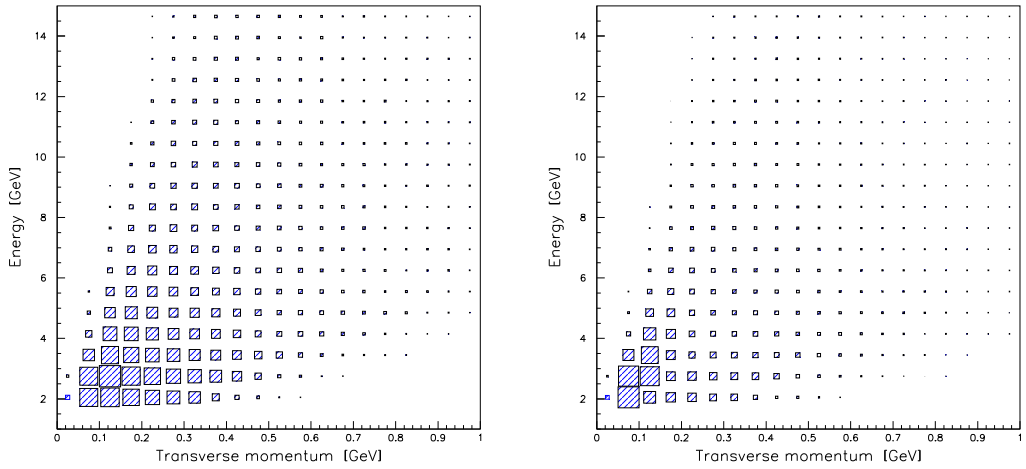

Figure 5.9: Energy vs. $P_\perp$ for ECAL clusters for data (left) and all Monte-Carlo events (right).

Firstly, clusters with high energies are more likely to be well reconstructed. An ECAL-cluster is reconstructed around a central cell which is the most energetic in that cluster. Clusters with higher energy in the central cell are then easier to define and reconstruct. No clusters with energies less than 1.0 are included in the analysis. Secondly it may be possible to separate the photons coming from $\chi_c \rightarrow J/\psi + \gamma$ decays from the other photons by a restriction on the cluster energy. However, it is seen from figure 5.10 that the photons from radiative χ_c decays cover energies from 0 to 10 GeV, and it is therefore not possible to cleanly isolate them by restrictions on the E_{clus} . But there is a high number of clusters with low energies in data and a cut of E_{clus} >2 therefore reduces the number of photon-candidates in data considerably, while the bulk of the χ_c photons are kept. The Monte-Carlo plots of the efficiency and the significance for the different energy cuts (see Appendix A, figure A.1) show that for Carbon the significance is stable until for cuts up to 3.5 GeV before it drops steeply. For Titanium the decrease in

significance seems more constant, also for cuts on low energy clusters. This may be explained by the higher background in the Titanium events because of higher atomic number of Titanium (Z=22) compared to Carbon (Z=6). For data (see Appendix B, figure B.1) it is seen that the efficiency and the significance drop for harder cuts on E_{clus} . However, for Carbon a small increase in the significance around 5.0 GeV is seen.

Due to the mentioned correlation between $P_\perp$ and E_{clus} , cuts on $P_\perp$ have been

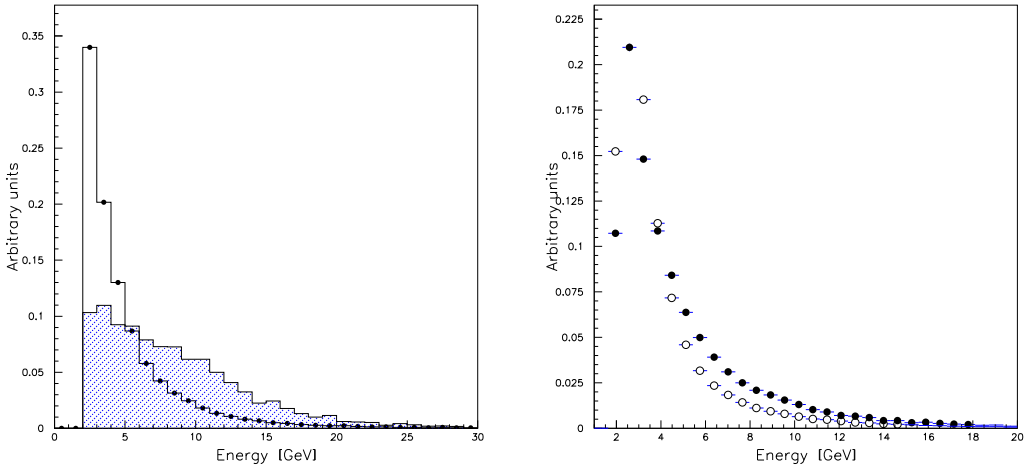

Figure 5.10: Cluster energy, Monte-Carlo vs. data: The left distributions show data (open histograms with points) compared with generated photons from χ_c decays only (shaded histogram). The right distributions are data (filled points) compared with Monte-Carlo events with no photons from χ_c (open points).

studied for E_{clus} =2.0 and E_{clus} = 3.0 GeV. The Monte-Carlo distributions (see Appendix A, figures A.2 and A.3) show that for both wires, and both energies, both the efficiency and the significance drop for increasing cuts on $P_\perp$. However, for data the significance of the signal increases for $P_\perp$ cuts of $P_\perp$ >0.15 and $P_\perp$ >0.2 GeV. For Monte-Carlo the corresponding efficiency drops in the same interval. This discrepancy between data and Monte-Carlo may influence the determination of the photon reconstruction efficiency and hence the final result.

The cuts on energy and transverse momentum are:

E_{clus} > 2.0 GeV
$P_{\perp}$ > 0.15 GeV

These cuts are used for both Carbon and Titanium events.

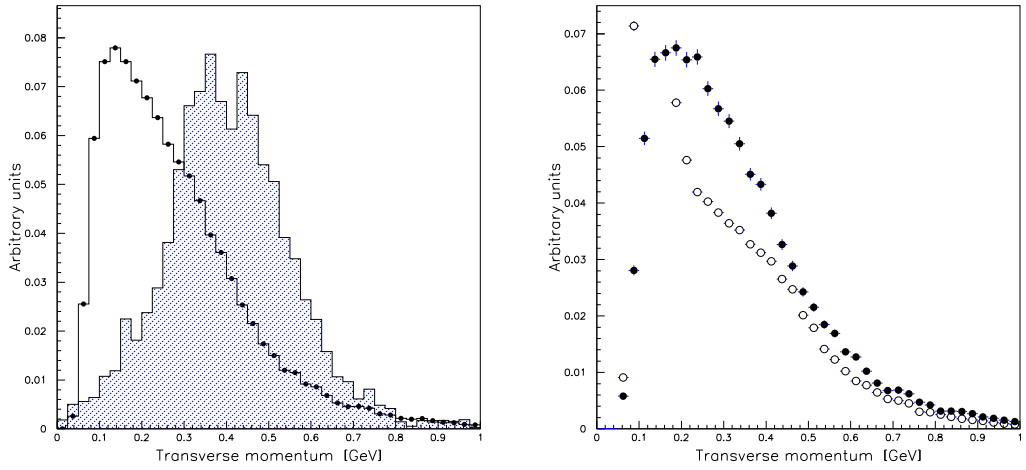

Figure 5.11: Transverse momentum, Monte-Carlo vs. data: The left plot shows clusters from data (open histogram with points) and the generated values for Monte-Carlo photons (shaded histogram). The distributions to the right are all Monte-Carlo clusters (open points) compared to clusters from data (filled points). All clusters have energy larger than 2.0 GeV.

5.2.3 Occupancy cuts

The *occupancy* of of the detector means in general the level of activity per event. More specifically, the occupancy here refers to the number of measured interactions in a given subdetector for one event. Two parameters related to the occupancy have been studied, namely the number of hits per event in the VDS (N_{vds}) and the number of reconstructed ECAL clusters per event (N_{clus}). Removing events with high occupancy may give improvements with respect to both the quality of the event reconstruction and the signal significance. The significance may be improved because high occupancy events give large contributions to the combinatorial photon background. But since these cuts remove full events it is also important to keep the cut values moderate to avoid reducing the available statistics.

The N_{vds} and N_{clus} parameters are compared to data in figure 5.12. It is seen

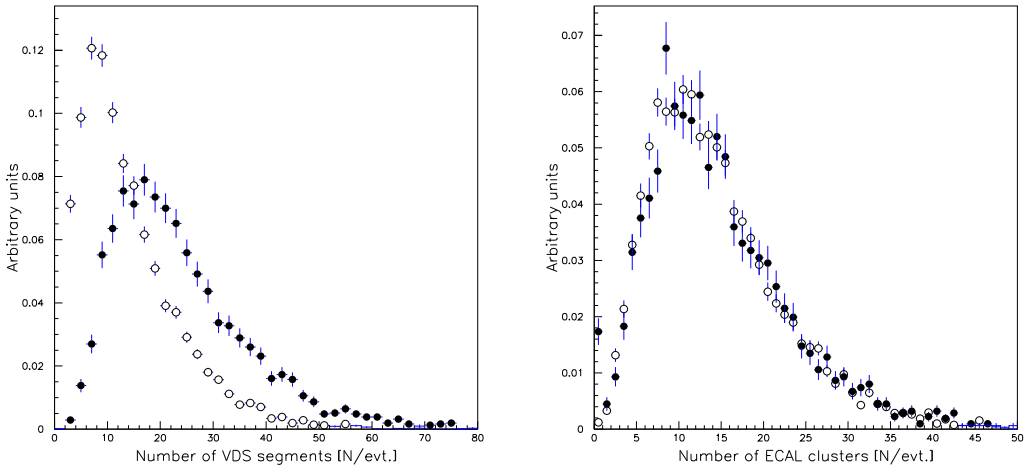

Figure 5.12: Comparison between data and Monte-Carlo for N_{vds} (left) E_{clus} (right). Events with mass close to the J/ψ is chosen for data.

that for data the N_{vds} parameter have more entries than the Monte-Carlo at N_{vds} >20. The Monte-Carlo events do not successfully reproduce the VDS occupancy from data. Moreover it is seen in figure 5.13 that the N_{vds} parameter is distributed differently for Carbon and Titanium events. This can be explained by the higher atomic number of Titanium, which generates more background. That the background is higher in Titanium is also seen in the J/ψ distributions in figure 4.5, Section 4.4. The N_{vds} parameter is not different for one or two wire runs as shown in figure 5.13. Because the occupancy is different for interactions from the two wires, these cuts have been studied separately, and applying different cuts for the different wires seem plausible.

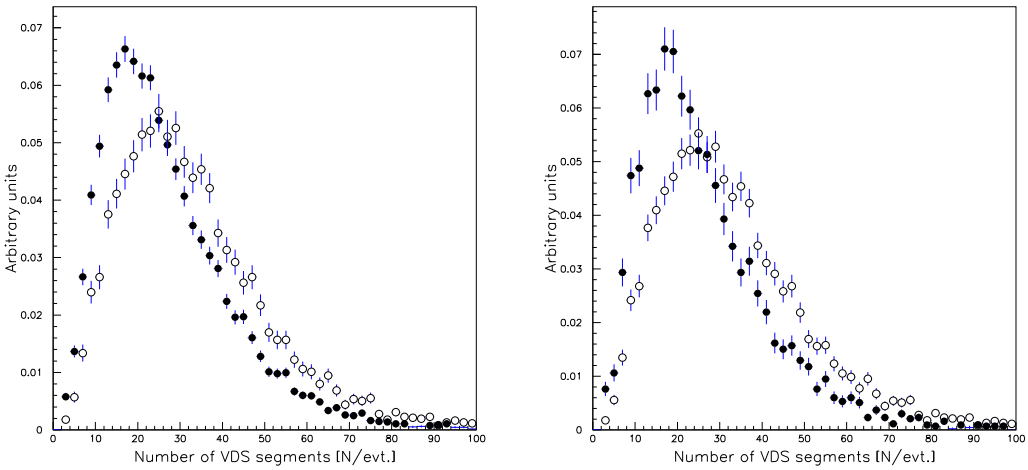

Figure 5.13: Values of N_{vds} per event for Carbon (black points) and Titanium (open points) for all runs (left) and two-wire runs only (right.)

The number of reconstructed χ_c particles and the signal significance in Monte-Carlo as a function of an upper limit on N_{vds} is given in Appendix A, figure A.4. It is seen that both the efficiency and the significance drops for N_{vds} <50. This is of course in agreement with figure 5.12 where only few events have N_{vds} >50. For data from the Carbon wire (see Appendix B, figure B.3) it is seen that both the efficiency and significance drops at $N_{vds} < 50$, but is enhanced for N_{vds} <30 and N_{vds} <20. For Titanium data (see see Appendix B, figure B.3) no clear χ_c signal was observed for N_{vds} <50, but both the efficiency and the significance are stable for the higher thresholds. The values chosen for this cut are:

Carbon:	$N_{vds}^{C} < 30$
Titanium:	$N_{vds}^{Ti} < 40$

The N_{clus} parameter is defined as the number of clusters per event with energy larger than 3.0 GeV. From figure 5.12 it is seen that N_{clus} is well reproduced by the Monte-Carlo. The motivation for restricting this parameter is to increase the signal significance by reducing the combinatorial background. Studying the distributions for the efficiencies and the significance for N_{clus} (see Appendix A, figure A.5) it is seen that the efficiency and the significance drop as the threshold value decreases. For data, the Carbon events (see Appendix B, figure B.4) show the same behavior as the Monte-Carlo, while for Titanium data (see Appendix B, figure B.4) the efficiency and significance seem stable until N_{clus} <30. Below this value, no signal was detectable. The cut for Carbon and Titanium is:

N_{clus} <30

5.2.4 ECAL cluster structure

The ECAL cluster structure refers to the distribution of energy within a cluster. Three parameters have been studied in this respect, namely the *width* of the cluster, the *asymmetry* of the cluster and the ratio of the *central cell energy to that of the total cluster* (R_{clus}). The width of the cluster is defined as the number of cells with considerable measured energy. This parameter can be used to evaluate whether the cluster is a single cell, a base or a structured cluster (see Section 3.6). The single cell cluster has all the energy deposited in one cell and has therefore width equal to one. For a base cluster the energy is typically deposited within a 3×3 cell region giving values of width from one to nine. A structured cluster would supposedly have even higher values.
The asymmetry of a cluster is defined by the ratio of the three most energetic cells of the cluster and its total energy. Hence it is closely related to the width and has a value equal to one if the cluster has a width of three or less.
To ensure that the cluster has some shower structure, a cut on the width is set larger than three. This cut removes clusters with unity values of both asymmetry and R_{clus} . (R_{clus} is unity if the width is equal to one.)
The asymmetry and R_{clus} have been studied with respect to efficiency and significance on data and Monte-Carlo. These studies have been done after all values of these parameters equal to unity have been removed.

The distributions of asymmetry for all Monte-Carlo clusters and clusters from χ_c decays (figure 5.15) show that they are nearly similarly distributed. This means that a cut on this parameter is unlikely to give a good background suppression. That this is the case is seen from the plots of the number of reconstructed particles and signal significance for both Monte-Carlo (Appendix A, figure A.6)and data (Appendix B, figure B.5). Therefore no cut is made on the asymmetry of the cluster.

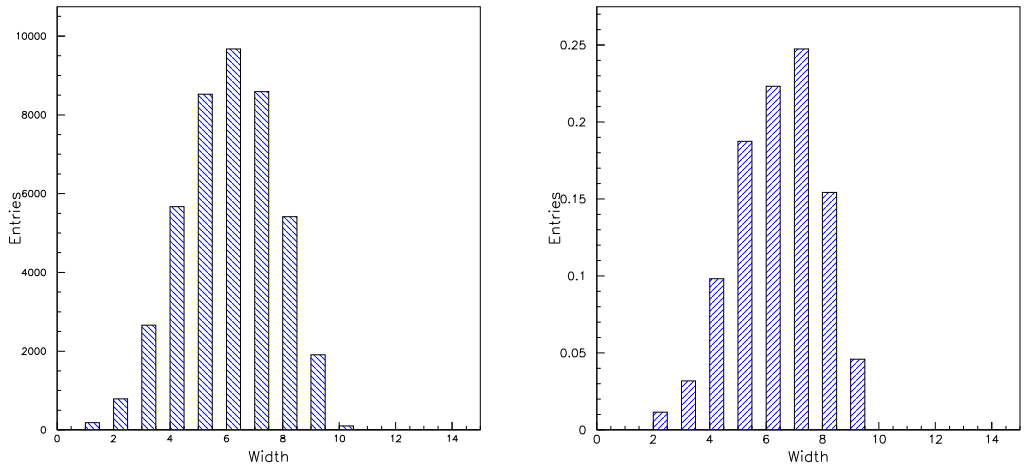

Figure 5.14: Width of clusters for data (left) and Monte-Carlo matched photons (right) show similar distributions.

For R_{clus} in Monte-Carlo it is seen in figure 5.16 that the clusters from radiative χ_c decays have more entries at higher values compared to all the clusters. The clusters from data show a somewhat different distribution than the Monte-Carlo clusters (see figure 5.16) which is also seen from the plots of the number of reconstructed χ_c and significance for cuts on R_{clus} (figures A.7, B.6), where the significance for Monte-Carlo drops for higher cuts while it is more or less stable in data. This may add to the systematic error on the determination of the photon reconstruction efficiency. The cut on R_{clus} is set to

$R_{clus} > 0.55$

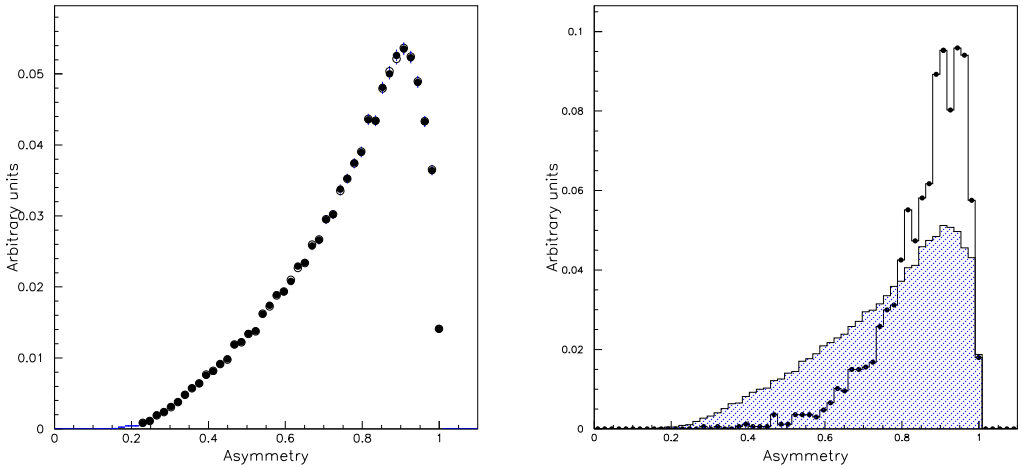

Figure 5.15: Cluster asymmetry for Monte-Carlo and data: The Monte-Carlo reproduces the data perfectly in the left plot and are overlapped by the black points from data. The right plot shows asymmetry for clusters from Monte-Carlo with no χ_c events (shaded histogram) compared to Monte-Carlo clusters from photons from radiative χ_c decays (open histogram with points).

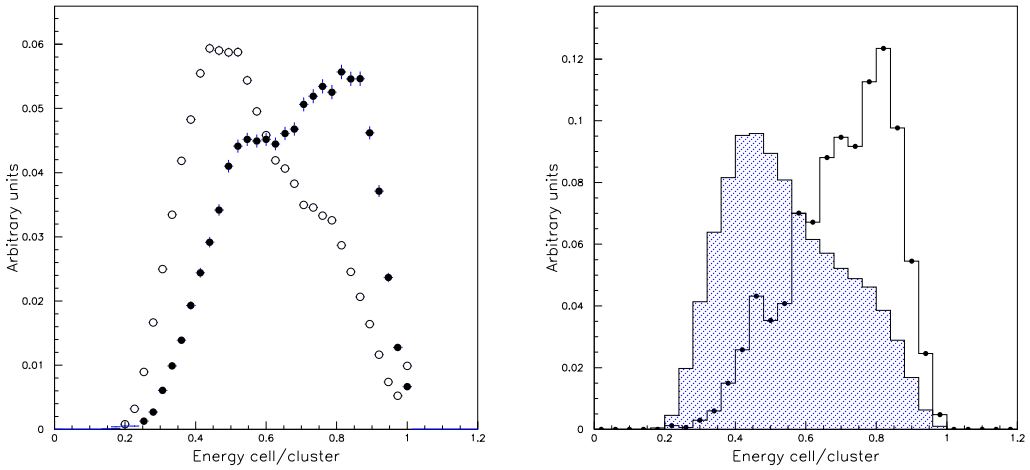

Figure 5.16: Comparison of R_{clus} between Monte-Carlo and data. The left plot shows clusters from data (black) and Monte-Carlo (open points) while the right plot shows Monte-Carlo with no clusters from χ_c events (shaded histogram) compared with Monte-Carlo clusters from χ_c only (open histogram with points).

5.2.5 Clusters from charged particles

In addition to electrons, charged particles like π^+ and π^- may deposit energy in the ECAL. Clusters from charged particles should if possible be excluded from the χ_c reconstruction to reduce the combinatorical background. Using information from the ECAL only, it is not possible to distinguish clusters caused by charged particles from those caused by photons. A possibility is to use information from the Main Tracking system to check if a charged track points to the cluster. The clusters from charged particles can then be identified and removed from the sample.
One immediate complication is the fact that a fraction of the photons emanating from χ_c decay convert into an electron positron pair by $\gamma \to e^+e^-$ in the vicinity of a nucleon. The fraction of converting photons is mentioned to be as high as 40% in [15]. Removing clusters pointed to by tracks from converted photons will then also reduce the reconstruction efficiency, taken that the e^+e^- pair enter the same cluster. If however the opening angle of the e^+e^- tracks is large enough to produce two clusters, this converted photon is in any case lost for χ_c reconstruction. The removal of clusters pointed to by charged tracks is used successfully in the CDF experiment [28].

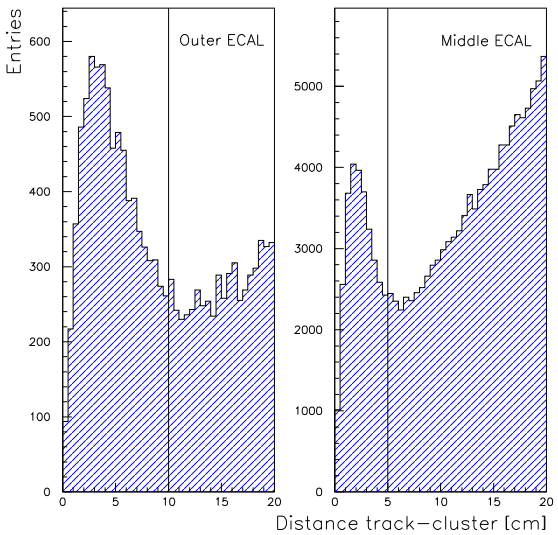

Figure 5.17: Data: Distance between estimated distance between the estimated position of charged tracks in and clusters in the ECAL. The lines in the histograms show the distance cut for the Outer (left) and the Middle (right) ECAL parts.

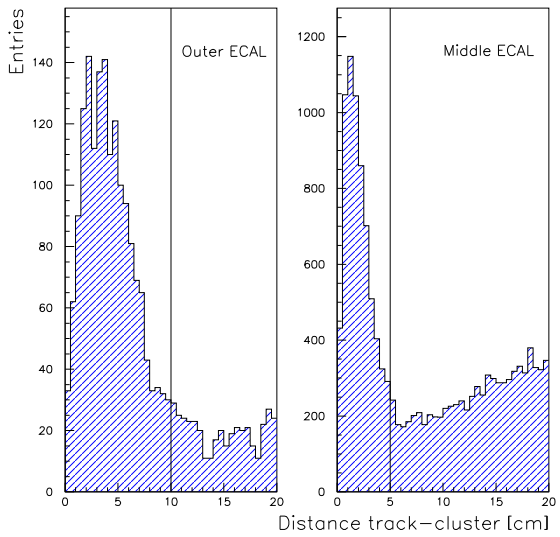

Figure 5.18: Monte-Carlo: Distance between estimated distance between the estimated position of charged tracks in and clusters in the ECAL for Monte-Carlo. The lines in the histograms show the distance cut for the Outer (left) and the Middle (right) ECAL parts.The distance cut is similar to what is used in data.

The Inner Tracker was not operational during most of the data taking. Therefore this study only includes the Middle and Outer parts of the ECAL parts which are covered by the Outer tracker. Because these ECAL parts have different spatial resolution (See Chapter 2, Section 3.6.) the study is done separately for the Inner and Outer ECAL. Only the events and clusters that have passed the already decided cuts are considered here. Tracks identified by the SLT as muons are not included because they are not expected to deposit energy in the ECAL. The technique used to calculate the impact point of a track at the given position of a cluster is much similar to the identification of true χ_c photons discussed in Section 5.1.2. The coordinates of the impact points are found by replacing the photon momentum components in eq. 5.3 by the corresponding track momenta:

$$(x_{trk}, y_{trk}) = (\frac{p_x}{p_z}R_z, \frac{p_y}{p_z}R_z) \tag{5.10}$$

Here R_z is the distance between the z-position of the start position of the track and the z-position of the cluster. The resulting distributions of the distance between the estimated impact point of the track and the position of the cluster (D_{trk}) are shown in figure 5.17. An increase in the number of entries is seen as D_{trk} is less than a value which is different for the two ECAL parts. The cluster is

identified as coming from a charged track if $D_{trk} < 10$ cm for the Outer ECAL. For the Middle ECAL this cut is set to $D_{trk} < 5.0$ cm. These cuts are marked with lines in figure 5.17.
As a cross check the angle θ_{trk} between the clusters and the tracks is studied, and figure 5.19 shows that $\cos\theta_{trk}$ is close to one for all clusters in the Middle ECAL with $D_{trk} < 5.0$ cm. This indicates that these clusters are caused by charged tracks.
The study is also performed on the Monte-Carlo sample where figure 5.18 indicates that the same cuts as those used on data can be applied to Monte-Carlo. Implementing this cut on the event from the Carbon wire in the Monte-Carlo sample resulted in 351 ± 61 reconstructed χ_c particles with a signal significance of 4.9. The efficiency is then 62.7% when compared to the number of reconstructed χ_c without this cut. The significance was reduced from 7.2 to 4.9 when this cut was applied. For data the number of reconstructed χ_c particles was reduced from 171 ± 52 to 94 ± 49 after applying this cut. The significance was reduced from 3.0 to 1.7.
Because the significance of the signals for both Monte-Carlo and data was reduced after removing clusters pointed to by charged tracks, this cut is not used in the following analysis. However, since the Inner ECAL was not considered because the ITR was not operated during the run 2000, this procedure should be tried for later runs using the full detector.

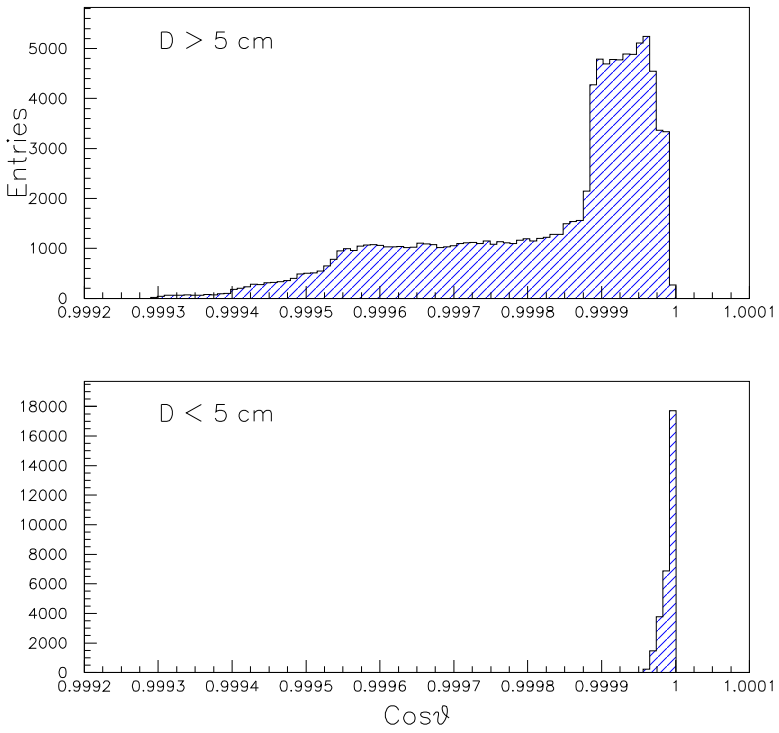

Figure 5.19: The histograms show cosθ_{trk}, where θ_{trl} is the angle between the charged tracks and the clusters, for a distance between the cluster position and the estimated position of the charged tracks of D_{trk} >5 cm (top) and D_{trk} <5 cm (bottom).

5.2.6 Background from π^0

The main contribution to the photon background is expected to come from the decay $\pi^0 \rightarrow \gamma\ \gamma$. The π^0 has a branching ratio of 98.8% [33] in this channel, and the π^0 is also the main fraction of the decay products of particles commonly produced at HERA-B like K^0_S, ω and Λ. A reduction of the combinatorical background under the χ_c signal is expected if the photons from π^0 are identified and removed from the sample of χ_c photon candidates.
The π^0 is reconstructed by calculating the invariant mass of two clusters given by

$$M_{\gamma\gamma} = \sqrt{2E^1_\gamma E^2_\gamma (1 - cos\theta)} \tag{5.11}$$

where E^i_γ is the energy of cluster i and θ the opening angle between the clusters 1 and 2. The expression is found from eq. 4.7 by assuming $|\vec{p}_\gamma| = E_\gamma$ due to massless photons. The angle is calculated from the definition of the dot-product given in eq. 5.4. The π^0 particles are assumed to decay at the z-position of the target wire for one wire runs. For runs with two wires, the vertex is assumed to have the same position as the vertex of the J/ψ muon candidates.
The events and clusters considered for π^0 reconstruction have been subject to the cuts for the reconstruction ofχ_c . In addition, only cluster pairs positioned in the same part of the ECAL are considered, and they must be separated by a distance roughly corresponding to two cells of the given ECAL part. The distance is calculated as

$$D_{\gamma\gamma} = \sqrt{(x_1 - x_2)^2 + (y_1 - y_2)^2}. \tag{5.12}$$

For the different ECAL parts the constraints on $D_{\gamma\gamma}$ are:

Inner:	$D_{\gamma\gamma} > 4.0$ cm.
Middle:	$D_{\gamma\gamma} > 11$ cm.
Outer:	$D_{\gamma\gamma} > 22$ cm.

This separation of the clusters is helpful because overlapping clusters are avoided [14]. The signals obtained for runs with one and two wires are shown in figure 5.2.6. The signals are fitted with a Gaussian and the background with a 4th order polynomial. The mean positions of the signals are 0.133 ± 0.001 GeV and 0.132 ± 0.001 GeV for one and two wire runs respectively. The slight shift compared to the table value of 0.1350 GeV [33] is not fully explained by a possible miscalibration of the Outer part of the ECAL (see Section 3.6); the mean with this part excluded is 0.1336 ± 0.0008, still shifted by 1 MeV. The shift could be due to a slight misalignment of the detector, but the mean of the signal agrees with the mean of 0.134 GeV found for the calibration of the ECAL (see figure 3.9). Within errors both these signals are in agreement with the table value. The

signals for one and two wire runs correspond well, indicating that the procedure is applicable for the total data sample. The signal for runs with both one and two wires is shown in figure 5.2.6 (left). The obtained mean position is 0.134 ± 0.001 with a width of 12 MeV.
The π^0 reconstruction is repeated for Monte-Carlo using similar procedures to those described for data. The signal shows a mean at 0.135 ± 0.002 GeV with a width of 9 MeV (see figure 5.2.6). Hence the resolution is 30% better in the Monte-Carlo.
To exclude the π^0 photons from the reconstruction of χ_c , all photons that are reconstructed within 3 standard deviations of the mean of the π^0 mass are removed. This interval is shown with lines in figure 5.2.6 for data and Monte-Carlo. The removal of π^0 candidates in Monte-Carlo reduces the χ_c reconstruction efficiency by 11.7%. The significance of the signal is also reduced from 7.6 to 7.0 after removing the π^0 candidates. For data the signal is reduced from 171 ± 52 to 144 ± 48 reconstructed χ_c after this cut is applied. The significance drops from 3.0 to 2.7.
Because the significance of the signals for both Monte-Carlo and data are reduced after removing the π^0 candidates, this procedure is not used in the following analysis. For later runs of data taking the statistics will be higher, and the χ_c can be reconstructed using harder cuts on energy and transverse momentum. Then the π^0 will be reconstructed with less background, and the procedure presented here may be more efficient.

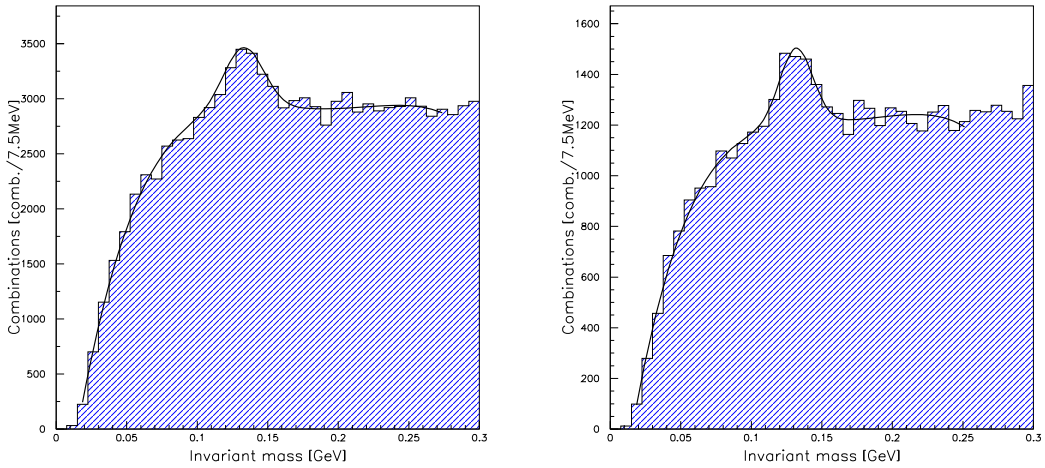

Parameters, one wire:
$N_{\pi^0} = 2258 \pm 437$
Mean=0.133 ± 0.001
Width=0.014 ± 0.002
$\chi^2 = 2.2$

Parameters, two wires:
$N_{\pi^0} = 1174 \pm 135$
Mean=0.132 ± 0.001
Width=0.012 ± 0.001
$\chi^2 = 1.6$

Figure 5.20: Reconstructed invariant mass of two ECAL clusters showing π^0 signal for runs with one and two wires (left) and Monte-Carlo (right). The lines indicate the interval corresponding to *pm* three standard deviations.

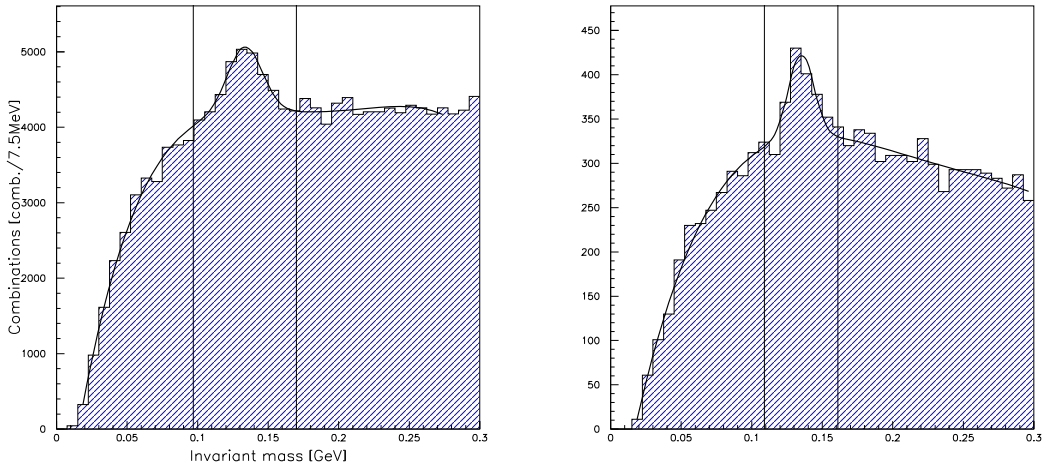

Parameters Data:
$N_{\pi^0} = 3477 \pm 252$
Mean=0.1336 ± 0.0008
Width=0.0122 ± 0.0008
$\chi^2 = 2.6$

Parameters Monte-Carlo:
$N_{\pi^0} = 273 \pm 56$
Mean=0.135 ± 0.002
Width=0.009 ± 0.002
$\chi^2 = 0.61$

Figure 5.21: Reconstructed invariant mass of two ECAL clusters showing π^0 signal for runs with one and two wires (left) and Monte-Carlo (right). The lines indicate the interval corresponding to pm three standard deviations.

5.2.7 Summary

The chosen cuts chosen for this analysis, including the cuts on the muons are:

VDS occupancy, Carbon	N_{vds} <30
VDS occupancy, Titanium	N_{vds} <40
Vertex probability	P_{vtx} >0.005
Muon-chamber likelihood	$\ell_\mu > 0.1$
ECAL occupancy	N_{clus} <30
Energy:	E_{clus} >2.0 GeV.
Transverse momentum:	$P_\perp$ >0.15 GeV
Width of cluster:	Width>3
Ratio of cluster energy central/total:	R_{clus} >0.55

These cuts will in the following be referred to as the *standard cuts*.
The optimization presented here is not based on a strict maximization of the significance Monte-Carlo because the Monte-Carlo events do not fully reproduce the experimental situation. The J/ψ signal for Monte-Carlo is background free while in the data there is an additional background below the J/ψ signal. Also; the occupancy of the detector is not fully reproduced in the Monte-Carlo events; the events in data have a higher charged track multiplicity as shown in Section 5.2.3. This requires harder cuts for data than the what is optimal for Monte-Carlo.
Because some cuts are selected from data with a basis in the plots of Appendix B, care has been taken to choose values that give a stable signal within variations of the respective cuts. This is to avoid choosing cuts based on statistical instabilities. In summary the cuts have been chosen to be reasonable with respect to both Monte-Carlo and data, but the tuning of the cuts was necessarily done on data.
The signals after all cuts are applied are shown in figure 6.3 in Section 6.2 of the next chapter. The signal for Carbon events yield 171 ± 52 reconstructed χ_c particles with a significance of 3.0 and the signal for Titanium events yield 105 ± 46 reconstructed χ_c particles with a significance of 2.1.
In the next chapter a detailed discussion of the χ_c signal is performed. First the width of the signal is found by comparison with Monte-Carlo, and then the results on F_{χ_c} are presented for Carbon and Titanium events separately. The combined result for both wires is also presented. The stability of the signals are then investigated with respect to variations of the energy cut on the clusters and the occupancy of the events. Finally the results are compared to previous measurements.

Chapter 6

Results and discussion

In the previous chapter the optimization of the χ_c signal was performed. The final results on F_{χ_c}, the fraction of J/ψ produced from χ_c, is presented in this chapter. Firstly the width of the signal fit is discussed. Then the χ_c resulting signals for Carbon and Titanium events are shown. The signal obtained by using the combination of both wires is also presented and the results on F_{χ_c} are calculated. The stability of the signal is then discussed with respect to cuts on cluster energy and occupancy. The impact on the signal determination when the Outer ECAL is excluded is also discussed. Then a rough estimation of the systematic error on the results is performed before the results are compared to previous measurements.

6.1 The χ_c signal

The histograms in figure 6.1 show the mass difference ΔM as defined in eq 5.2, including the standard cuts summarized in Section 5.2.7. There are no stunning signal peaks visible here, but there are clear enhancements for ΔM around 0.45 GeV for both wires which corresponds to the mass difference between two χ_c states χ_{c1} and χ_{c2} and the J/ψ (see Table 2.1). The signals will be fitted with Gaussians to extract the mean positions, number of entries and the significance of the signals, but first the expected width of the signal is estimated in the next section.

6.1.1 Width of the signal

The width of the Gaussian fitted to the χ_c signal will be fixed to what is expected from Monte-Carlo simulation as described in Section 5.1.2. This is necessary because a fit with free parameters generally returns an unrealistic width with respect

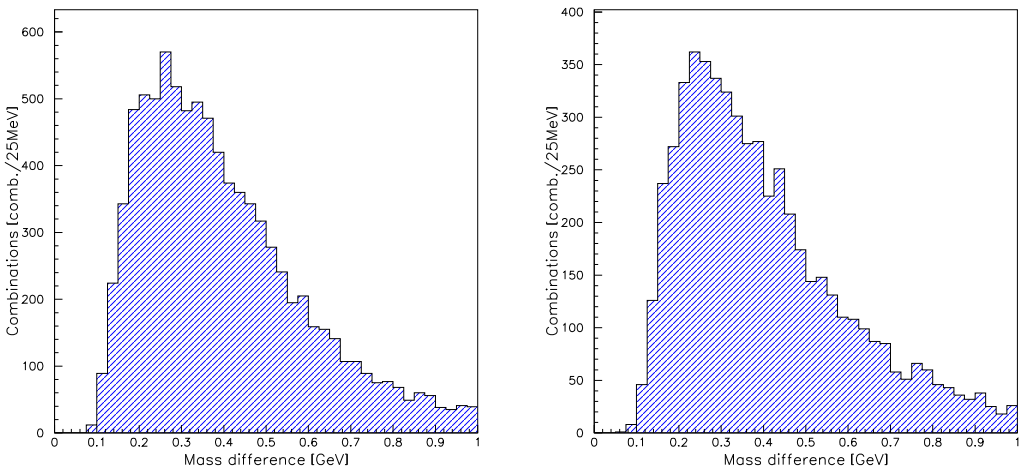

Figure 6.1: The mass difference ΔM for Carbon event (left) and Titanium events (right) after applying the standard cuts

to the ECAL resolution[1]. The distance D_{clus} between the reconstructed clusters and the estimated position of the generated χ_c photon in the ECAL is set to $D_{clus} < 5.0$ cm. The standard cuts, described in 5.2.7, are included when the width is estimated. Since the width is dependent on how the χ_c particles are distributed between the spin states χ_{c1} and χ_{c2} , the events have been weighted to correspond with NRQCD model as described in [13] and [16]. The NRQCD model is expected to give the most realistic ratio of χ_{c1} and χ_{c2} . Only the χ_{c1} and χ_{c2} particles will be reconstructed in the data because the decay $\chi_{c0} \rightarrow J/\psi$ γ has a branching ratio of $(6.6 \cdot 10^{-3})\%$ which is too low to give any contribution with the available statistics. (Less than 2 χ_{c0} particles are expected per 200 χ_{c1} and χ_{c2} .) The χ_{c0} is not therefore included in the plots for the width estimation. The Monte-Carlo simulation is not expected to fully reproduce the experimental ECAL resolution. Coherent noise in the ECAL, ECAL chamber misalignment, and incorrect track reconstruction in data are not fully taken into account [37]. In Section 5.2.6 the resolution is estimated to be 30% better for Monte-Carlo than for data. For χ_c reconstruction the difference is smaller because only a single photon is used, but how much is not obvious. In the following an additional 10% is added to the width found in Monte-Carlo when the χ_c signal is fitted in data. The width of the χ_c signal in Monte-Carlo has been checked for both wires separately. A difference in the width for the two wires is not expected because the detector configurations are similar. The higher background found in Titanium

[1]The width found from a free fit with the energy cut used here is app. 75 MeV, which is wider than expected.

events should not influence the width. The difference between the widths is found to be 4%, and is therefore considered negligible.
The occupancy cuts have been tuned individually for Carbon and Titanium events, and the width is found to depend on the number of segments in the VDS per event N_{vds} and the number of clusters with energy larger than 3.0 GeV N_{clus}. The cuts used are N_{vds} >30 and $N_{vds} > 40$ for Carbon and Titanium events respectively, and the resulting difference in the width is of 1 MeV. The difference from the N_{vds} cuts is then considered small and is not taken into account. The cut on N_{clus} is similar for Carbon and Titanium events. The cut on N_{vds} selected for the Carbon wire will be used in the following because this is the largest sample in both data and Monte-Carlo.

The χ_c signal obtained after setting $D_{clus} < 5.0$ cm is shown in figure 6.2. The

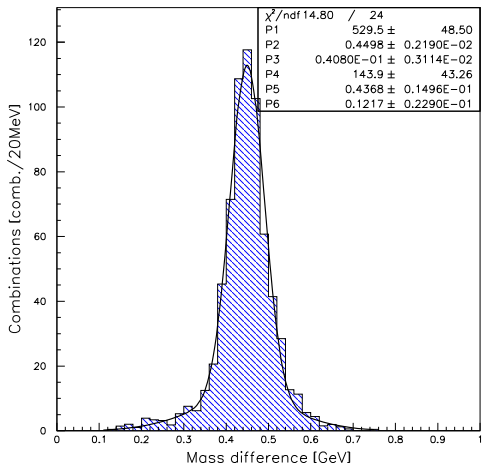

Figure 6.2: Monte-Carlo: Width estimation of the χ_c signal.

signal still has some background and is therefore fitted with two Gaussians, one is wide to accommodate the background, while the other is fitted to the signal. The width of the Monte-Carlo χ_c signal is then:

$\sigma_{MC} = 41 \pm 3$ MeV

Adding another 10% to account for the assumed difference in resolution for data and Monte-Carlo gives an estimated width of the χ_c signal in data:

$\sigma_{data} = 45$ MeV

The χ_c for the Carbon and Titanium wires with fitted signals are shown in figure 6.3. The cuts used to obtain the signals are the standard cuts described in

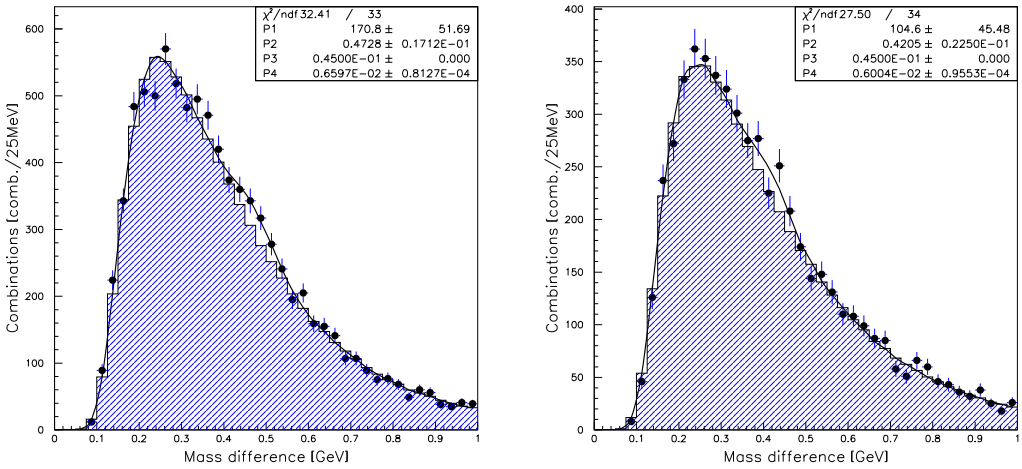

Figure 6.3: Data: The optimized χ_c signals for the Carbon wire (left) and the Titanium wire (right).

Sections 5.2.7. The resulting χ_c signal from Carbon events show

$$N^C_{\chi_c} = 171 \pm 52$$

reconstructed χ_c particles with a significance of $\frac{S}{\sqrt{B}} = 3.0$. The mean position of the mass difference is 0.47 ± 0.02 GeV.
For Titanium events the number of reconstructed χ_c particles are

$$N^{Ti}_{\chi_c} = 105 \pm 46$$

with a significance of $\frac{S}{\sqrt{B}} = 2.1$. The mean of the mass difference is 0.42 ± 0.2.
The corresponding distributions for Monte-Carlo are shown in figure 6.5. The Monte-Carlo distributions are fitted with a fixed width of 41 MeV as argued above. These distributions are not weighted because the Monte-Carlo weights were not included in the mixed background events[2]. The mean position of the mass difference is 0.45 ± 0.01 GeV and 0.44 ± 0.01 GeV for Carbon and Titanium events respectively.
Within errors the mean positions of the mass differences for data and Monte-Carlo agree reasonably, but the fact that for Carbon events and for Titanium events the mean positions are shifted in opposite directions on give a signal determination which is not entirely satisfactory.
However when the two wires are combined, there is good agreement with Monte-Carlo. The distribution is shown in figure 6.4 and is obtained using the standard cuts for the Carbon signal.

[2]This is not related to the Monte-Carlo sample, but to the procedures used here.

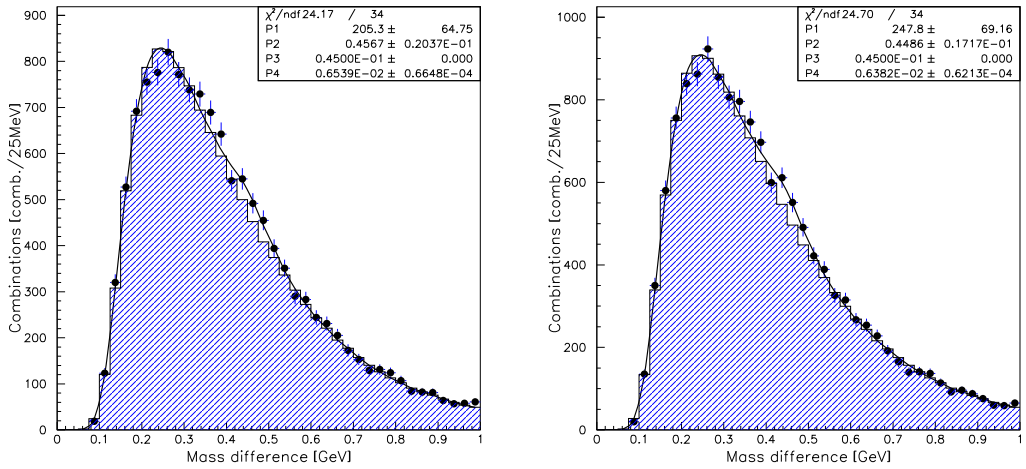

Figure 6.4: Data: The χ_c signal for both wires. The left distribution shows the signal with cuts optimized for Carbon wire, while the right distribution is the sum of the histograms optimized for each wire individually.

The number of reconstructed χ_c is

$$N_{\chi_c}^{both} = 205 \pm 65$$

with a mean position at 0.46 ± 0.02 GeV. Within errors, this is in agreement with the corresponding Monte-Carlo distribution for both wires combined where the fit gives a mean of 0.446 ± 0.004. The shift in the individual wires are then ascribed to the low statistics in the signals. The significance of the signal in both wires is 2.8. The number of reconstructed χ_c particles combining both wires is not the same as the sum of the entries in the signals optimized for each wire individually. This is due to the difference in the N_{vds} cut. The sum of the signals individually optimized signals is shown in figure 6.4 and gives

$$N_{\chi_c}^{tot} = 248 \pm 69$$

The sum of these signal is obtained by adding the histograms of figure 6.3.

6.2 Results on $F_{\chi c}$

The fraction of J/ψ produced from χ_c decays is given by

$$F_{\chi_c}^{J/\psi} = \frac{N_{\chi_c}}{N_{J/\psi} \cdot \varepsilon_\gamma}. \tag{6.1}$$

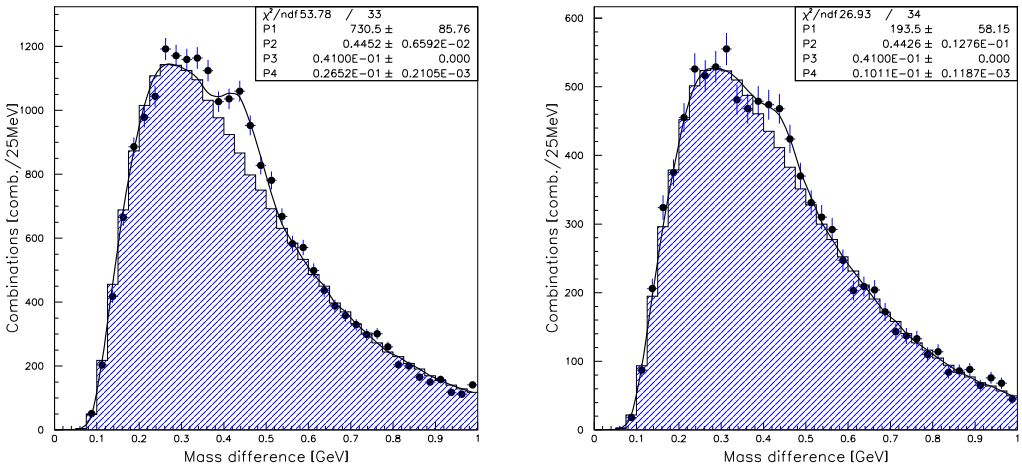

Figure 6.5: Monte-Carlo: The optimized χ_c signals for the Carbon wire (left) and the Titanium wire (right).

Wire	$N^{mc}_{J/\psi\chi_c}$	$N^{mc}_{\chi_c sel}$	ε_γ
Carbon	2177 ± 46	726 ± 56	0.33 ± 0.03
Titanium	859 ± 30	249 ± 39	0.30 ± 0.05
Both	3034 ± 51	205 ± 65	0.32 ± 0.02

Table 6.1: Data: Number of reconstructed J/ψ and χ_c particles and photon efficiency for the different wires.

and is derived in Section 4.1. In addition to finding the number of reconstructed J/ψ particles $N_{J/\psi}$ and the number of reconstructed χ_{c1} and χ_{c2} particles N_{χ_c}, the photon reconstruction efficiency must be calculated. The photon efficiency ε_γ is found by considering a Monte-Carlo sub-sample where all J/ψ particles are from χ_c decays. The ratio of the number of J/ψ particles $N^{mc}_{J/\psi\chi_c}$ and number of reconstructed χ_c particles from this sub-sample $N^{mc}_{\chi_c sel}$ using the standard cuts will then give the photon efficiency:

$$\varepsilon_\gamma = \frac{N^{mc}_{J/\psi\chi_c}}{N^{mc}_{\chi_c sel}} \tag{6.2}$$

The obtained values of $N^{mc}_{J/\psi\chi_c}$, $N^{mc}_{\chi_c sel}$ and ε_γ are summarized for the Carbon, Titanium and the combination of both wires in Table 6.1.

Using eq. 4.2 the obtained results for F_{χ_c} are:

Carbon wire: $F^{C}_{\chi_c}$=0.36 $\pm$ 0.11

Titanium wire: $F^{Ti}_{\chi_c}$=0.47 $\pm$ 0.22

Both wires: $F^{both}_{\chi_c} = 0.32 \pm 0.10$

The errors here are statistical only. Since the error in the Titanium events is dominated by low Monte-Carlo statistics it seems sensible at this point to present the combined result as the final result. For both wires the signal is better determined with respect to the mean position of the fitted signal. Before the results obtained here are compared to previous measurements, the stability of the signal is discussed to give a rough estimate of the systematic errors.

6.3 Signal stability

The stability of the signals has been studied for variations of the cuts discussed in the Sections 4.4 and 5.2. The plots showing the number of reconstructed χ_c particles and the significance of the signals are shown in Appendix A for Monte-Carlo and Appendix B for data. A complete estimation of the systematic errors are beyond the scope of this thesis, but has been performed in [15]. A detailed study of the χ_c signal for variations on the cluster energy, E_{clus}, and the number of segments in the VDS per event, N_{vds} , is however presented in the following. The study is done for Carbon and Titanium events and with events from both wires combined.

6.3.1 Signal vs. E_{clus}

Varying the energy cut gives an important test of the analysis results. The background peaks at higher values for higher energy cuts (see figure 5.1) and is therefore a test of the background description and the signal determination. The energy spectrum seen in data is well reproduced by the Monte-Carlo as shown in figure 5.1.2, but since weighting of the Monte-Carlo events was not applied for the determination of the photon efficiency ε_γ, a check on the result of F_{χ_c} as a function of E_{clus} is relevant.
The resulting signals for Carbon events with $E_\gamma > 2, 3, 4, 5$ GeV, are shown in figure 6.8. The mean of the χ_c signal is stable for $E_{clus} > 2, 3, 4$ GeV while for $E > 5$ GeV the mean is shifted to 0.49 GeV. The results on F_{χ_c} in figure 6.6 show stability within the errors, but is somewhat higher for E> 4, 5 GeV. The results

E_{clus} [GeV]	N_{χ_c}	$\frac{S}{\sqrt{B}}$	ε_γ	F_{χ_c}
2.0	171 ± 52	3.0 ± 0.9	0.33 ± 0.03	0.36 ± 0.11
3.0	143 ± 47	2.8 ± 0.9	0.31 ± 0.02	0.32 ± 0.11
4.0	148 ± 43	3.2 ± 0.9	0.27 ± 0.02	0.39 ± 0.12
5.0	130 ± 39	3.2 ± 0.9	0.23 ± 0.02	0.40 ± 0.13
2.0*	151 ± 48	2.8 ± 0.9	0.29 ± 0.03	0.36 ± 0.12

Table 6.2: Data, Carbon wire: Number of reconstructed χ_c , significance, photon efficiency and results for F_{χ_c} as a function of the cut on cluster energy E_{clus}. The number of reconstructed J/ψ particles was 1429 ± 45 for all cuts. *) Outer ECAL is removed.

on F_{χ_c} , the number of reconstructed χ_c particles, ε_γ for the different energy cuts are summarized in Table 6.2.
The invariant mass distributions for the Titanium wire with cuts on $E_\gamma > 2, 3, 4, 5$ GeV are shown in figure 6.9. Here the χ_c signal is not well reconstructed for $E_\gamma > 5.0$ GeV. Up to $E_\gamma > 4.0$ GeV the signal is stable with respect to mean position. The results on F_{χ_c} are shown in figure 6.6 and the numerical values, together with the number of reconstructed χ_c particles, ε_γ are summarized in Table 6.3. The statistical errors are large in the Titanium data, but the result on F_{χ_c} seem to be stable.
For the combination of both wires, the resulting χ_c signals are shown in figure 6.10. The mean of the signal fit seem to shift upwards for $E_{clus} > 4, 5$ GeV. The results on F_{χ_c} however are stable with the exception of $E_{clus} > 5.0$ GeV where F_{χ_c} is low. The numerical values with the number of reconstructed χ_c particles, ε_γ are summarized in Table 6.4.
The conclusion concerning the stability of the χ_c signal with respect to cuts on E_{clus} is that for the run 2000 data a cut of $E_{clus} > 5.0$ is too hard. With this cut the signals are not well reconstructed and the result on F_{χ_c} deviates from those obtained with the lower cuts on E_{clus}. This is likely to be connected to the low statistics available from the run 2000 rather than the background description and signal determination. Even if the background peaks close to the mean of the χ_c signal for $E > 5.0$ GeV the signal should still be well determined because the width is fixed.

E_{clus} [GeV]	N_{χ_c}	$\frac{S}{\sqrt{B}}$	ε_γ	F_{χ_c}
2.0	105 ± 46	2.1	0.30 ± 0.05	0.47 ± 0.22
3.0	103 ± 39	2.4	0.28 ± 0.04	0.50 ± 0.21
4.0	82 ± 37	2.2	0.24 ± 0.04	0.45 ± 0.22
5.0	44 ± 34	1.3	0.23 ± 0.03	0.26 ± 0.20
2.0*	80 ± 44	1.7	0.28 ± 0.04	0.39 ± 0.2

Table 6.3: Data, Titanium wire: Number of reconstructed χ_c , significance, photon efficiency and results for F_{χ_c} as a function of the cut on cluster energy E_{clus}. The number of reconstructed J/ψ particles was 1429 ± 45 for all cuts. *) Outer ECAL is removed

E_{clus} [GeV]	N_{χ_c}	$\frac{S}{\sqrt{B}}$	ε_γ	F_{χ_c}
2.0	205 ± 65	2.8 ± 0.9	0.32 ± 0.02	0.32 ± 0.10
3.0	190 ± 59	3.0 ± 0.9	0.30 ± 0.02	0.31 ± 0.10
4.0	177 ± 53	3.1 ± 0.9	0.26 ± 0.02	0.34 ± 0.10
5.0	146 ± 47	3.0 ± 0.9	0.23 ± 0.02	0.21 ± 0.08

Table 6.4: Data, Both wires: Number of reconstructed χ_c , significance, photon efficiency and results for F_{χ_c} as a function of the cut on cluster energy E_{clus}.*) Outer ECAL is removed.

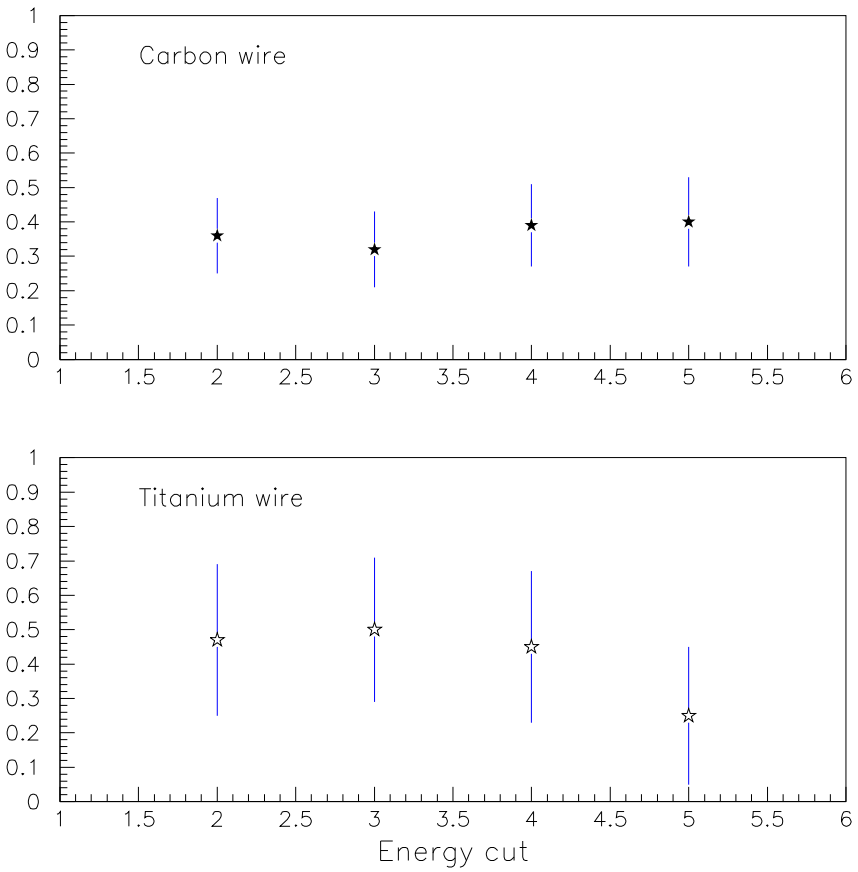

Figure 6.6: The results for F_{χ_c} for different cuts on the cluster energy for Carbon (top) and Titanium (bottom) events.

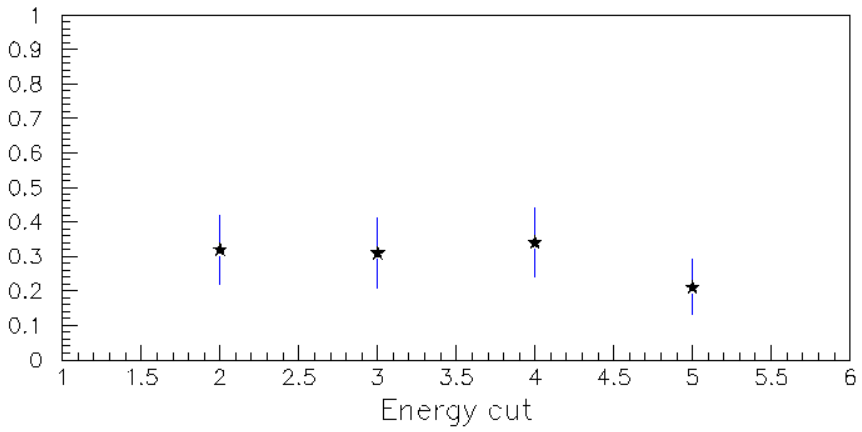

Figure 6.7: The results for F_{χ_c} for different cuts on the cluster energy for events from both wires.

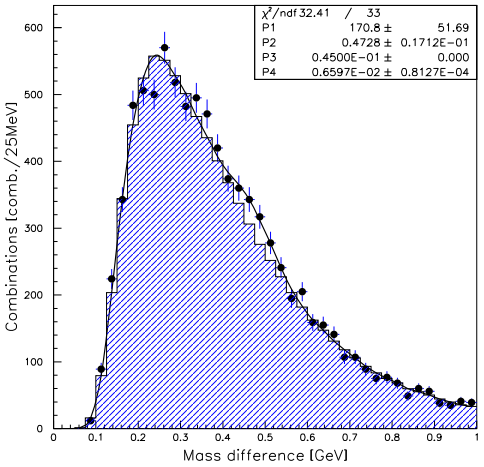

E_{clus} >2.0 GeV

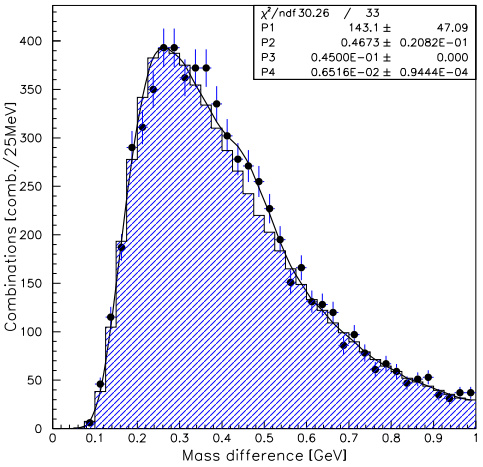

E_{clus}>3.0 GeV

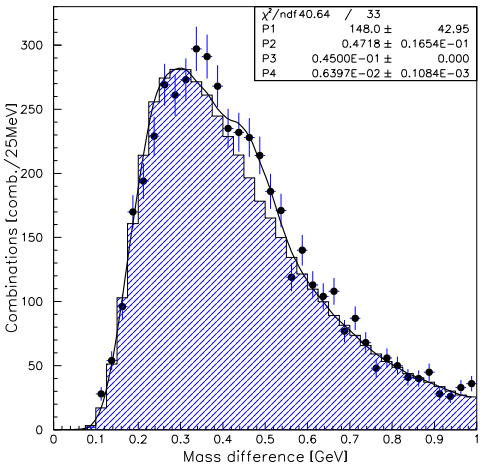

E_{clus}>4.0 GeV

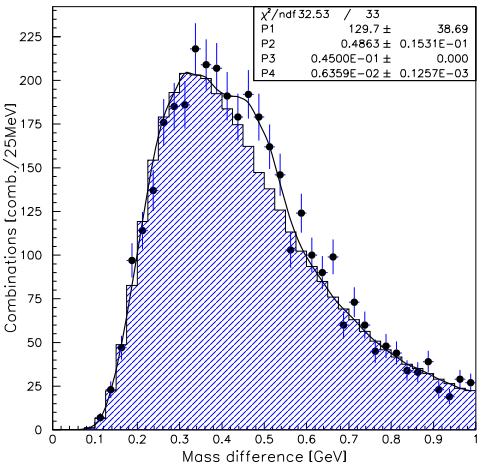

E_{clus}>5.0 GeV

Figure 6.8: Data, Carbon wire: The χ_c signal for various cuts on the cluster energy E_{clus}.

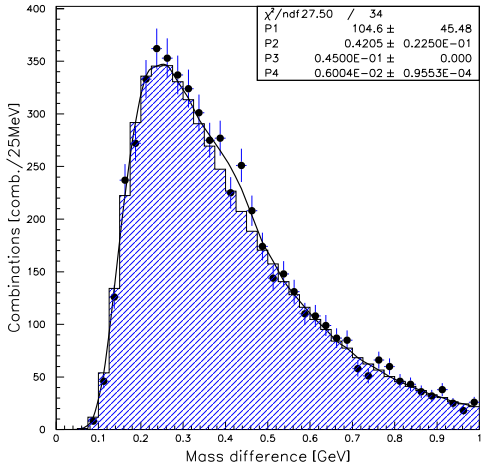

E_{clus} >2.0 GeV

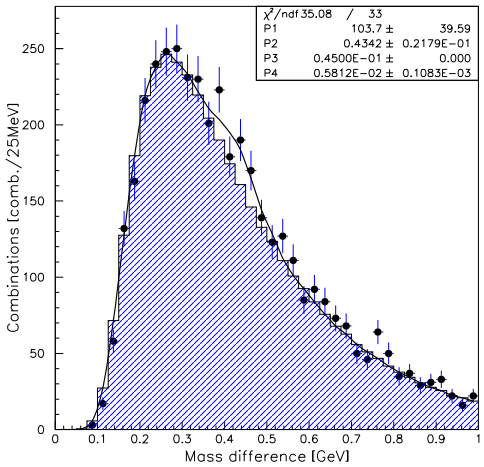

E_{clus}>3.0 GeV

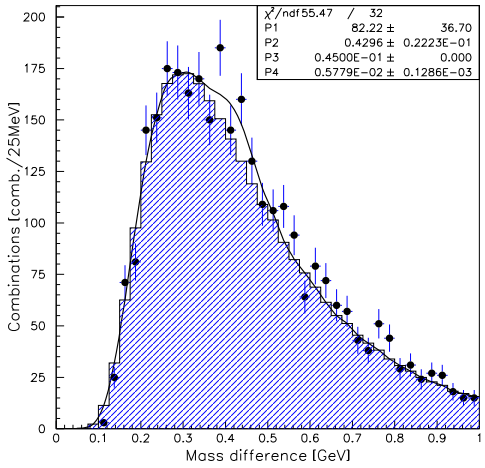

E_{clus}>4.0 GeV

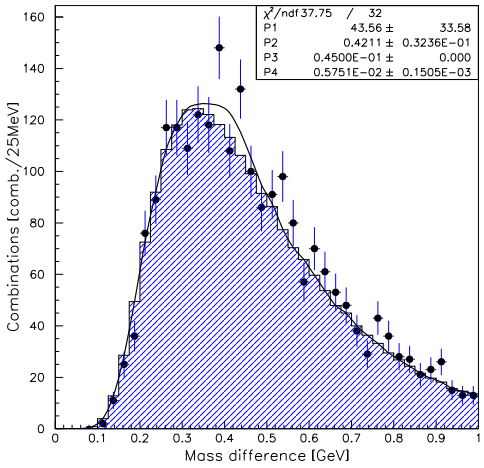

E_{clus}>5.0 GeV

Figure 6.9: Data, Titanium wire: The χ_c signal for various cuts on E_γ.

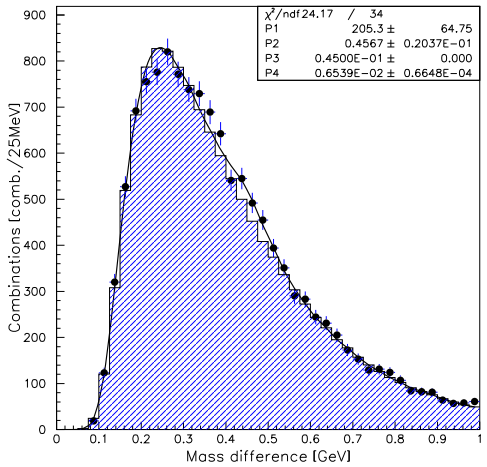

E_{clus} >2.0 GeV

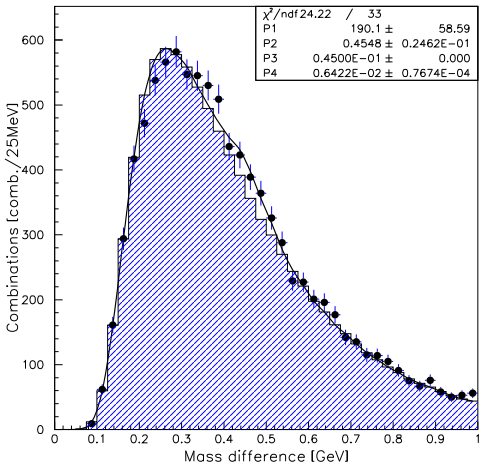

E_{clus}>3.0 GeV

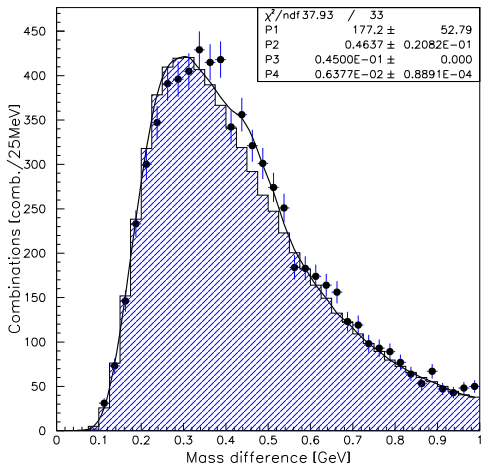

E_{clus}>4.0 GeV

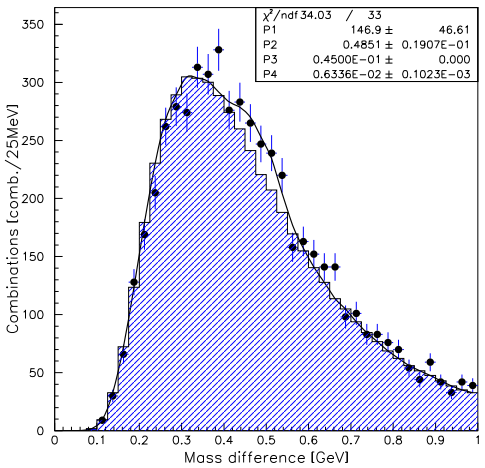

E_{clus}>5.0 GeV

Figure 6.10: Data, Both wires: The χ_c signal for various cuts on E_γ.

6.3.2 Signal vs. N_{vds}

The N_{vds} parameter is proven not to be fully reproduced by the Monte-Carlo where it is underestimated (see Section 5.2.3, figure 5.12). It has also been shown that there is a difference in N_{vds} for Carbon and Titanium events (see figure 5.13). To study the results on F_{χ_c} with respect to N_{vds} therefore gives an important systematic test of the analysis.
The χ_c signal for Carbon events with $N_{vds} < 40, 35, 30, 25$ is shown in figure 6.13. The mean positions of the signals are reasonably stable within variations on the N_{vds} parameter and the results on F_{χ_c} , plotted in figure 6.11, show stability within errors for all the N_{vds} cuts. F_{χ_c} is lower for cuts of N_{vds} <35, 40 than N_{vds} <30, 25. This occurs because the harder cuts on N_{vds} increase the number of entries in the signal in data. In Monte-Carlo ε_γ also increases for the harder N_{vds} cuts, which is in accordance to the data. That the effect is larger for data than for Monte-Carlo may be due to the higher occupancy in the data. The number of J/ψ and χ_c particles, significance, ε_γ and F_{χ_c} as a function of the N_{vds} cuts for Carbon events is summarized in Table 6.5.
For Titanium events the invariant mass distributions are shown in figure 6.14. The signal is stable for cuts down to $N_{vds} < 35$, while for N_{vds} <30 the mean of the signal is shifted by approximately 40 MeV compared to the other distributions. The results on F_{χ_c} as a function on N_{vds} cuts is shown in figure 6.11 and is stable within errors, only the result on F_{χ_c} for N_{vds} <50 is higher than for the harder cuts. The number of J/ψ and χ_c particles, significance, ε_γ and F_{χ_c} for the Titanium events as a function of N_{vds} is summarized in Table 6.6.
For the combination of both wires, the resulting χ_c signals for the different N_{vds} cuts are shown in figure 6.15. The signals are divided between two mean positions, 0.42-0.43 GeV for $N_{vds} < 50, 40, 35$ and 0.45-0.46 for $N_{vds} < 30, 25$. The result on F_{χ_c} is however stable for all cuts on N_{vds} . This may indicate that the mean of the fit is unstable due to low statistics. However, the mean positions are in reasonable agreement within the errors of 20-30 MeV. The switching between the two mass positions can be explained by the fact that two signal peaks are fitted with one Gaussian. The mass difference between the J/ψ and the χ_{c1} and χ_{c2} is 0.414 GeV 0.460 GeV respectively which is in accordance with the two signal maxima.
It is seen that the softer N_{vds} cuts give a less well determined signal in Carbon events, while the opposite trend is seen in Titanium events. But since the result on F_{χ_c} is stable for all N_{vds} cuts when the combination of the two wires is used, the instabilities in the results on F_{χ_c} for the separate wires can be explained as an effect due to low signal statistics.

N_{vds}	$N_{J/\psi}$	N_{χ_c}	$\frac{S}{\sqrt{B}}$	ε_γ	F_{χ_c}
40	1622 ± 44	130 ± 56	2.0 ± 0.9	0.32 ± 0.03	0.25 ± 0.11
35	1536 ± 47	145 ± 56	2.3 ± 0.9	0.32 ± 0.03	0.29 ± 0.12
30	1429 ± 45	171 ± 52	3.0 ± 0.9	0.33 ± 0.03	0.36 ± 0.11
25	1226 ± 41	157 ± 47	3.0 ± 0.9	0.34 ± 0.03	0.38 ± 0.12

Table 6.5: Data, Carbon wire: J/ψ and χ_c signal for different cuts on N_{vds} with significance of χ_c signal and results for F_{χ_c} .

N_{vds}	$N_{J/\psi}$	N_{χ_c}	$\frac{S}{\sqrt{B}}$	ε_γ	F_{χ_c}
50	810 ± 33	142 ± 49	2.7 ± 0.9	0.29 ± 0.05	0.61 ± 0.23
40	743 ± 33	105 ± 46	2.1 ± 0.9	0.30 ± 0.05	0.47 ± 0.22
35	696 ± 31	101 ± 43	2.2 ± 0.9	0.30 ± 0.05	0.48 ± 0.21
30	629 ± 29	75 ± 43	1.7 ± 0.9	0.32 ± 0.05	0.37 ± 0.22

Table 6.6: Data, Titanium wire: J/ψ and χ_c signal for different cuts on N_{vds} with significance of χ_c signal and results for F_{χ_c} .

N_{vds}	$N_{J/\psi}$	N_{χ_c}	$\frac{S}{\sqrt{B}}$	ε_γ	F_{χ_c}
50	2495 ± 60	278 ± 83	3.1 ± 0.9	0.30 ± 0.02	0.37 ± 0.12
40	2359 ± 57	240 ± 81	2.8 ± 0.9	0.31 ± 0.02	0.35 ± 0.12
35	2219 ± 54	251 ± 76	3.1 ± 0.9	0.31 ± 0.02	0.37 ± 0.12
30	2034 ± 51	205 ± 65	2.8 ± 0.9	0.32 ± 0.02	0.32 ± 0.10
25	1707 ± 48	202 ± 58	3.1 ± 0.9	0.32 ± 0.02	0.37 ± 0.11

Table 6.7: Data, Both wires: J/ψ and χ_c signal for different cuts on N_{vds} with significance of χ_c signal and results for F_{χ_c} .

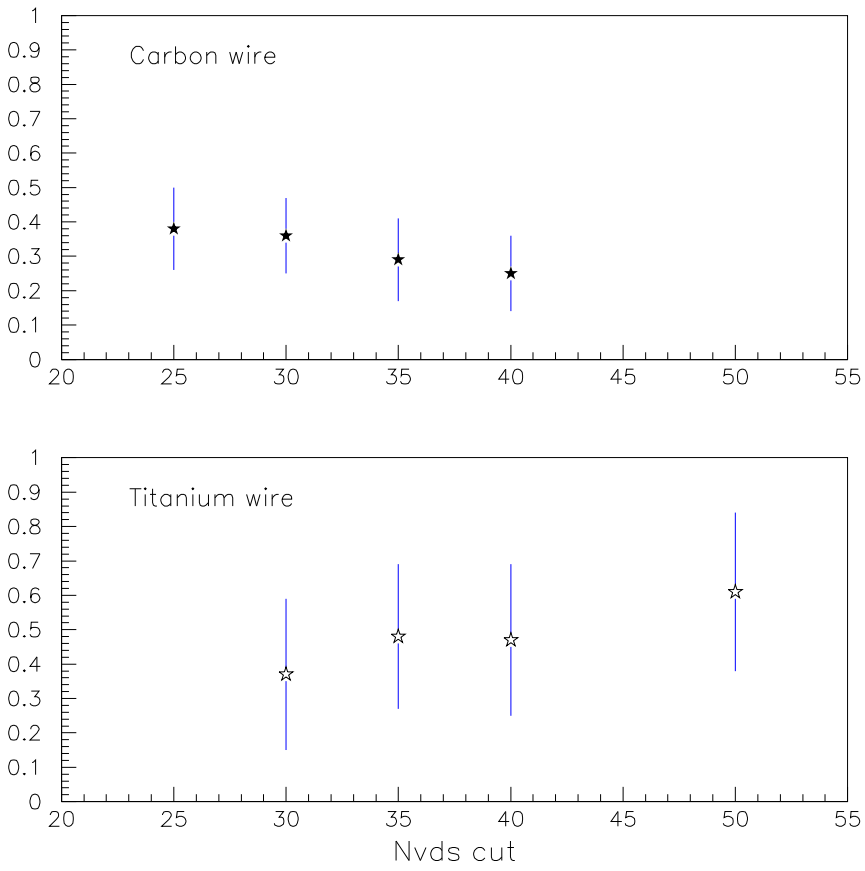

Figure 6.11: Results on F_{χ_c} as a function of N_{vds} for Carbon (top) and Titanium (bottom).

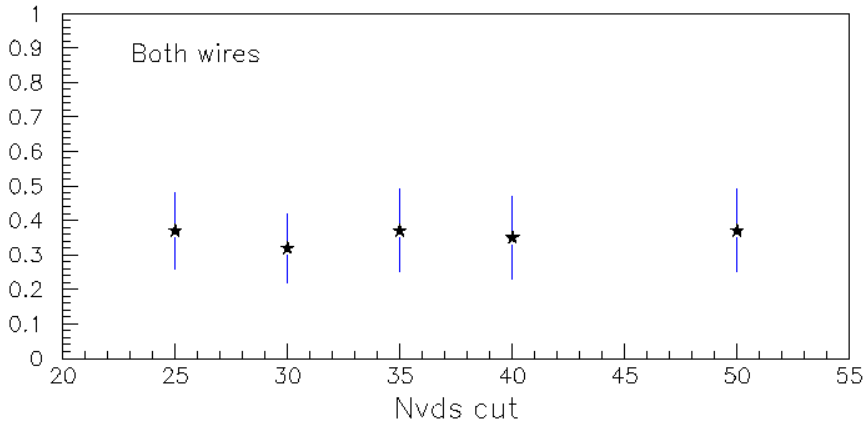

Figure 6.12: Results on F_{χ_c} as a function of N_{vds} for events from both wires.

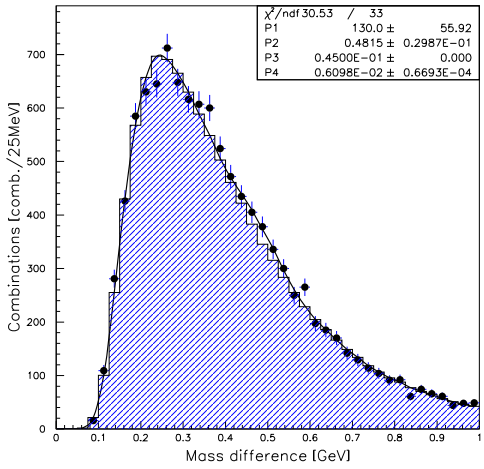

N_{nvds} <40

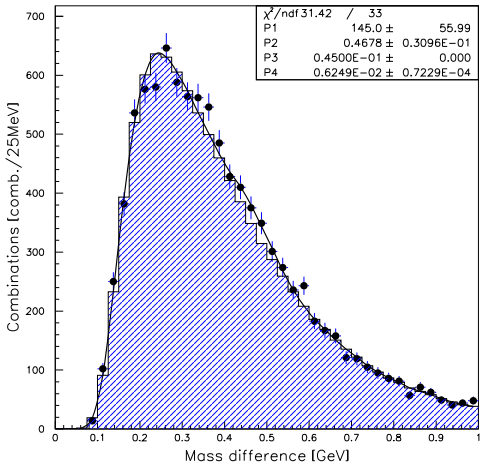

N_{nvds}<35

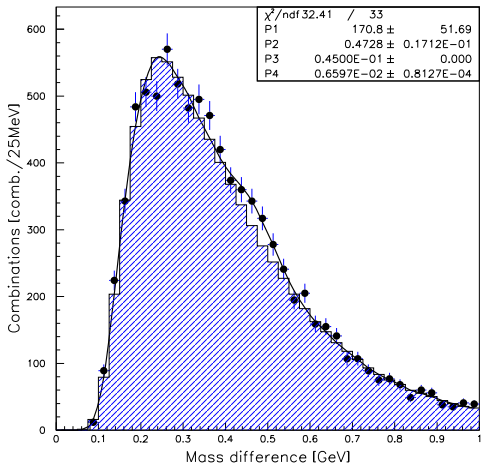

N_{nvds}<30

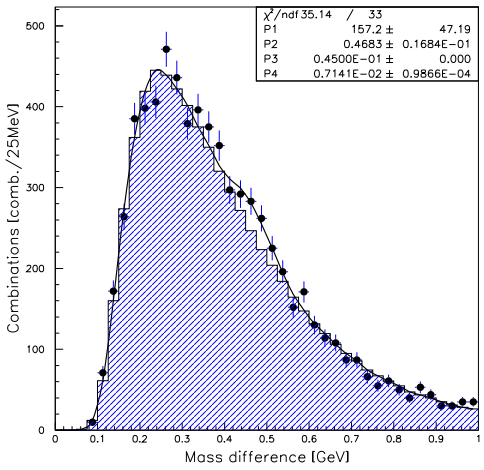

N_{nvds}<25

Figure 6.13: χ_c signal for various cuts on NVDS, Carbon wire.

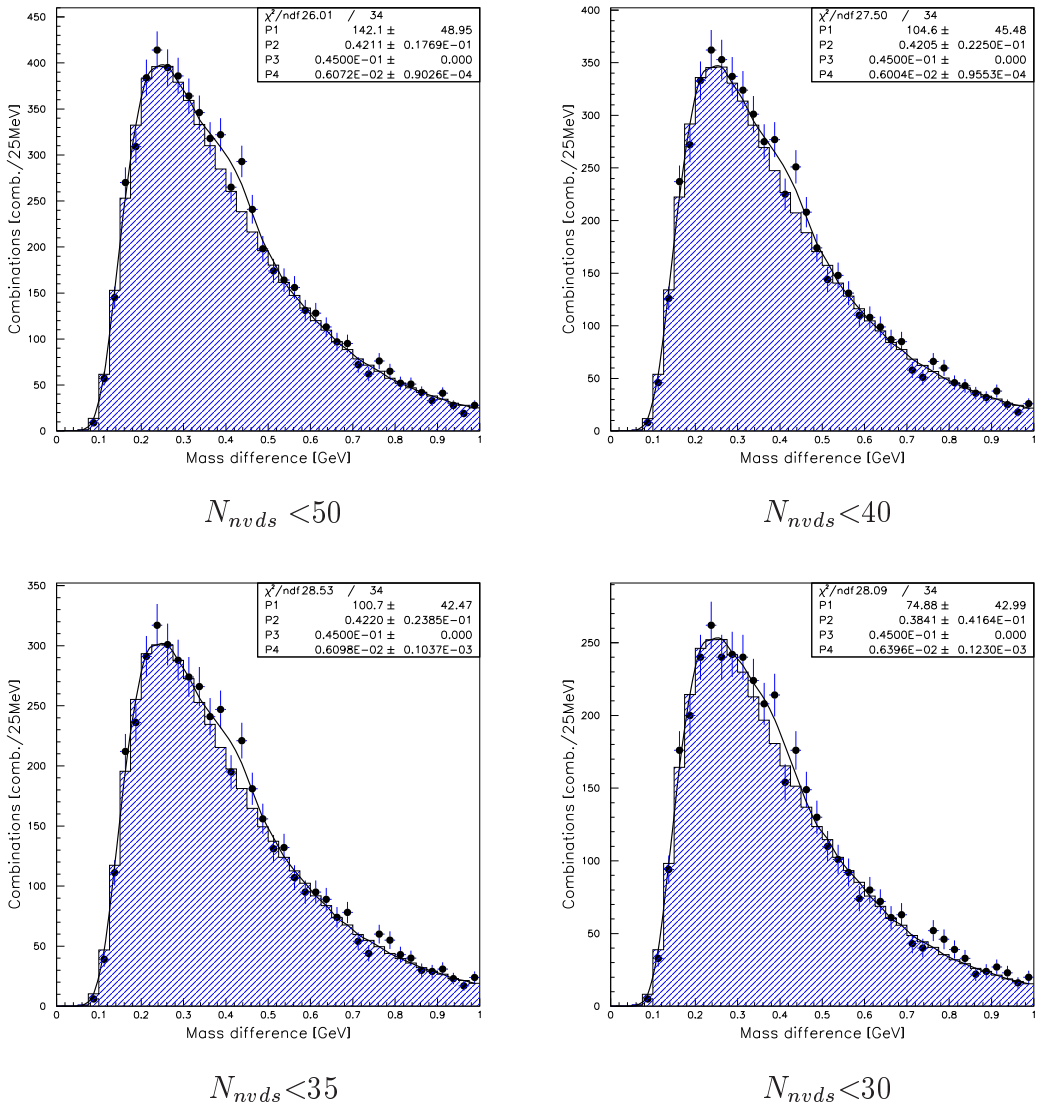

Figure 6.14: The χ_c signal for various cuts on NVDS, Titanium wire.

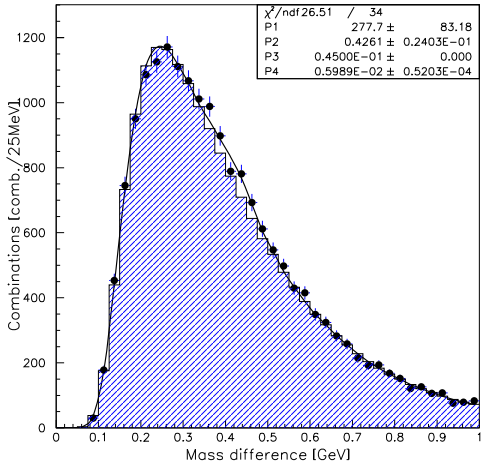

N_{nvds} <50

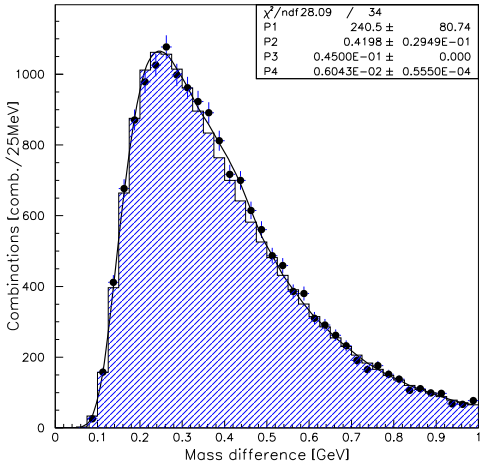

N_{nvds}<40

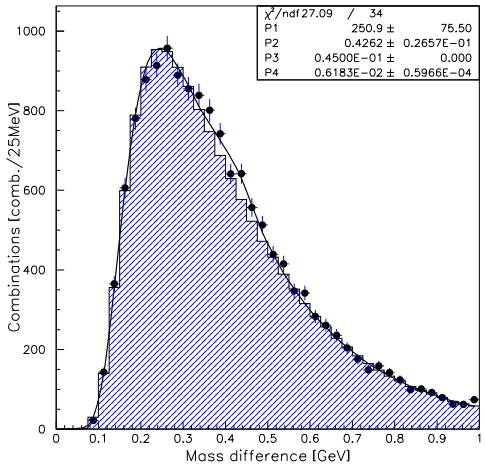

N_{nvds}<35

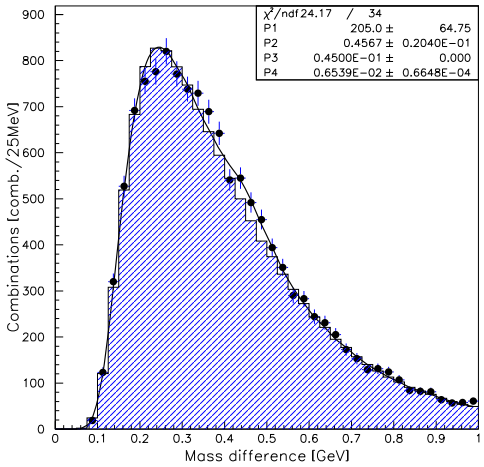

N_{nvds}<30

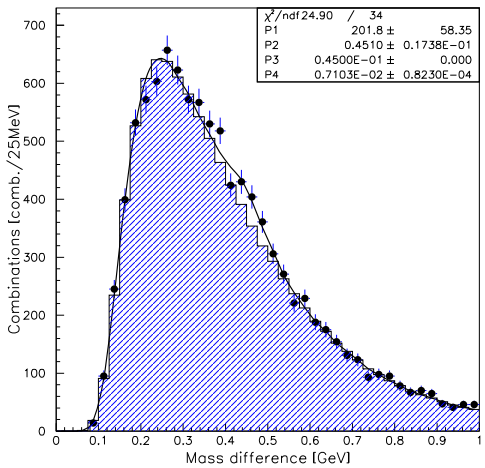

N_{nvds}<25

Figure 6.15: The χ_c signal for various cuts on NVDS, Both wires.

6.3.3 Exclusion of the Outer ECAL

As mentioned in Section 3.6, the Outer ECAL is not calibrated with the same precision as the other ECAL parts. It is therefore possible that the exclusion of this part will improve the determination of the mean of the signal. The distributions for Carbon and Titanium events with standard cuts, the combination of both wires with the cuts used for Carbon, and the sum of the optimized signals for Carbon and Titanium are shown in figure 6.16. The mean positions with the Outer ECAL included and excluded are:

Mean positions, Outer ECAL included:
Carbon: 0.473 GeV
Titanium: 0.421 GeV
Both: 0.457 GeV
Both optim. C,Ti: 0.449 GeV

Mean positions, Outer ECAL excluded:
Carbon: 0.465 GeV
Titanium: 0.406 GeV
Both: 0.449 GeV
Both optim. C,Ti: 0.436 GeV

The trend is that the mean positions move slightly closer to the expected mean from Monte-Carlo of approximately 0.45 GeV when the Outer ECAL is excluded. One exception is the Titanium signal, which moves further from the expected mean, from 0.421 GeV to 0.406 GeV. However, the inclusion of the Outer ECAL has no drastic effect on the mean position. This agrees with the result in Section 5.2.6 where the mean of the reconstructed π^0 seems independent of the exclusion of the Outer ECAL. The Outer ECAL is therefore included in the analysis.

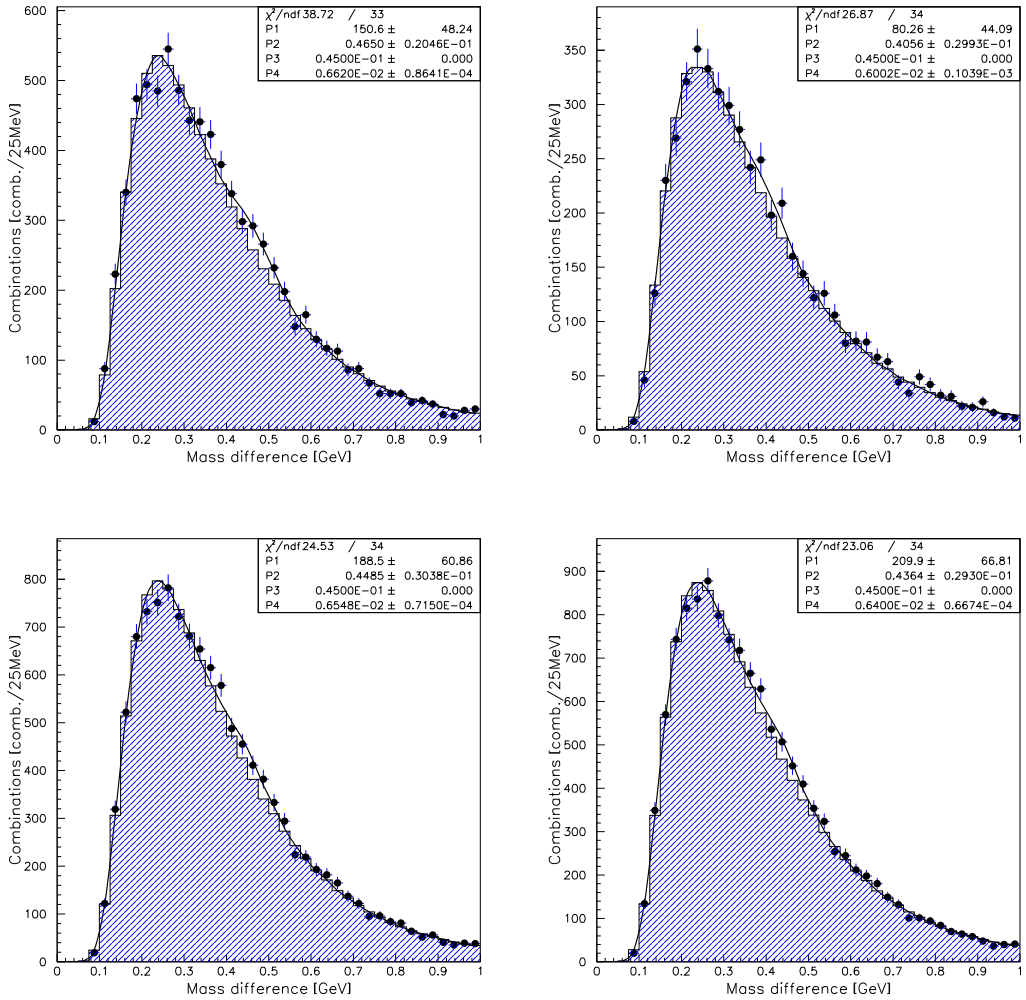

Figure 6.16: χ_c signals without the Outer ECAL for Carbon wire (top, left), Titanium wire (top, right), both wires with cuts for Carbon (bottom, left), and sum of the signals optimized individually for the two wires (bottom, left).

6.3.4 Summary

For the estimation of the systematic error the results from the combined wires are considered. The results on F_{χ_c} have been shown to be stable within the statistical errors for different cuts on E_{clus} as long as the highest cut of 5.0 GeV is avoided (see Table 6.4 and figure 6.7). From $E_{clus} > 2.0$ GeV to $E_{clus} > 4.0$ GeV the result on F_{χ_c} changes by 6%. For the cut on N_{vds} , the result on F_{χ_c} changes by 15% when the cut value is varied by ± 5 (see Table 6.7 and figure 6.11).
The variations in the results due to the cuts on E_{clus} and N_{vds} are well within the statistical errors of approximately 30%. The systematic error due to cut dependency is therefore not easily extracted from this study. A detailed study of the systematic errors in the estimation of the F_{χ_c} is performed in [15]. Here an systematic error from cut dependence is estimated to 6% and the total systematic error is estimated to 10.5%. These estimates seem reasonable with respect to the study performed here.
The final results, including systematic errors of 10.5% are then:

Carbon wire: $F_{\chi_c}^{C} = 0.36 \pm 0.11 \pm 0.04$

Titanium wire: $F_{\chi_c}^{Ti} = 0.47 \pm 0.22 \pm 0.05$

Both wires: $F_{\chi_c}^{both} = 0.32 \pm 0.10 \pm 0.03$

The first error is statistical and the second systematic.

6.4 Comparison with previous measurements

Previous measurements, which are relevant for comparison with the result obtained here, include experiments performed with both pion and proton beams. All the experiments which have measured F_{χ_c} have had energy levels where the production mechanisms are expected to be similar for πN and pN reactions as described in Section 2.1. At these energies the charmonium production is dominated by gluon-fusion. A description of the experiments which previously have measured the F_{χ_c} , is given in Appendix C. The previously obtained results on F_{χ_c} and the χ_c cross sections are compiled in Appendix C, Table C.1.
The measurements for the separate target material interactions, proton-Carbon and proton-Titanium, are compared with the previous measurements in figure 6.17. The result from proton-Titanium reactions has a large error and agrees with any other measurement, although the central value of 0.47 is high compared to the other results. The result from proton-Carbon reactions also agrees with the previous measurements, but in a more convincing way with smaller errors.

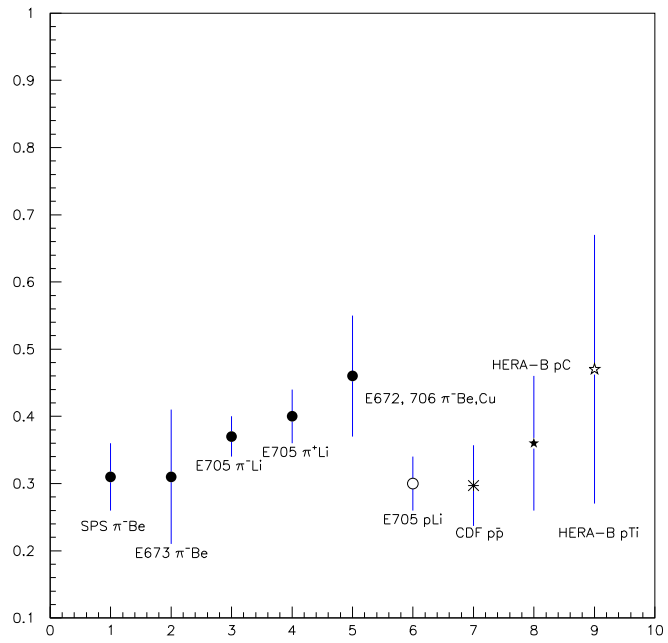

Figure 6.17: The results for F_{χ_c} for proton-Carbon and proton-Titanium interactions compared with previous results.

The obtained results on F_{χ_c} for the combination of both wires is compared to previous measurements in figure 6.18. The measurement by the E705 collaboration at Fermilab [31] is the only[3] measurement with pN reactions, and this result obtained at HERA-B is in excellent agreement with this measurement.
As mentioned in Section 2.1, and as can be seen in figure 6.18, there is an observed discrepancy between the measured value of F_{χ_c} for πN reactions and the pN reactions. This discrepancy is not explained by the NRQCD production model which predict similar results for F_{χ_c} when the beam energy is sufficiently high. The result obtained here is lower than the measurements in πN reactions by the E705 and E706 experiments at Fermilab. But due to the errors on the measurements no definite conclusion can be drawn on the basis of this HERA-B measurement. However, this result supports the trend in the previous measurements where the fraction of J/ψ produced from χ_c is lower for pN reactions than for πN reactions. A speculative, but still reasonable, explanation to the higher value of F_{χ_c} seen for pion beams, can be given by considering the fact that the charged pions are bound states of two quarks, while the protons contain three quarks. The two

[3]Not including the measurement from E673, where only 11.8 ± 5.4 χ_c were reconstructed.

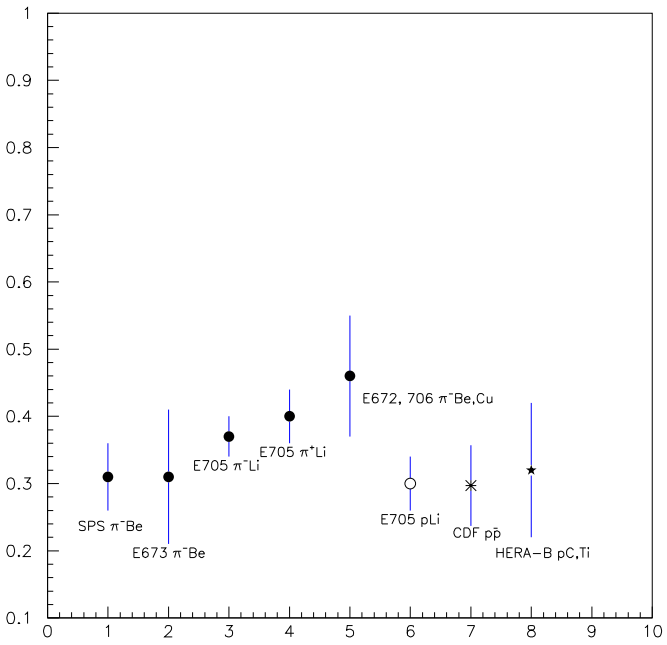

Figure 6.18: The combined results for F_{χ_c} for proton-Carbon and proton-Titanium interactions compared with previous results.

gluons binding the quarks in the pions then have more available energy than the three gluons in the protons if the beam energies are similar. The result in harder, more energetic, gluons in the πN gluon-fusion reactions compared to those for the pN reactions. This may in turn increase the cross-sections for the χ_c state in πN reactions compared to pN reactions.
In Section 2.2 the value of F_{χ_c} predicted by the Non-Relativistic QCD (NRQCD) model is argued to be somewhat higher than 0.27. This result obtained at HERA-B supports this prediction of $F_{\chi_c}^{NR} \geq 0.27$. The prediction from the Color Singlet Model (CSM) of $F_{\chi_c}^{CSM} = 0.69$ (see Table 2.2) is not compatible with this measurement.

In this chapter the final results on the fraction of J/ψ produced from decays of χ_c have been presented and discussed. In the next chapter the conclusions of this thesis are presented followed by the outlook for the next period of data taking at HERA-B.

Chapter 7

Conclusions and Outlook

The study has been performed from using a sample of approximately $450 \cdot 10^3$ triggered di-muon events from the run 2000 at HERA-B. From this sample the light quark particles ω, ρ and ϕ have been reconstructed in addition to the Charmonium states J/ψ , χ_c and ψ' . The χ_c was reconstructed by adding a photon to the J/ψ invariant mass.
Based on $N^C_{\chi_c} = 171 \pm 52$ reconstructed χ_c particles from Carbon events, $N^{Ti}_{\chi_c} = 105 \pm 46$ reconstructed χ_c particles from Titanium events and $N^{both}_{\chi_c} = 205 \pm 65$ for the combination of both wires, the fraction of J/ψ particles produced from the decay $\chi_c \to J/\psi\ \gamma$ has been measured. The are results obtained are:

Carbon wire: $F^C_{\chi_c}$=$0.36 \pm 0.11 \pm 0.04$

Titanium wire: $F^{Ti}_{\chi_c}$=$0.47 \pm 0.22 \pm 0.05$

Both wires: $F^{both}_{\chi_c} = 0.32 \pm 0.10 \pm 0.03$

The first error is statistical and the second error systematic. The systematic error is 10.5% of the obtained result. The results are mutually compatible within errors.
The result obtained with the combination of the two target wires is regarded the most reliable due to low statistics in the signals for the separate wires. The combined result agrees well with the comparable measurement from the E705 collaboration [31]. This measurement from HERA-B supports the observed discrepancy between F_{χ_c} measured in πN and pN reactions. The predicted value from Non-Relativistic QCD production model of $F^{NR}_{\chi_c} \geq 0.27$ is confirmed. The prediction from the Color Singlet production Model of $F^{CSM}_{\chi_c} = 0.69$ can be excluded.

Using the run 2000 data from HERA-B a measurement of the branching ratio of the ω to a di-muon final state is expected to be possible. The analysis is ongoing and may provide the second measurement in the world of this branching ratio.
The data taking for the run 2002 has started during the work on this thesis. This run is expected to yield 2.1 million reconstructed J/ψ particles [38]. This opens the possibility for a wide range of measurements in the field of heavy quark production. An estimated number of $300 \cdot 10^3$ χ_c will give a measurement of F_{χ_c} with unprecedented precision. This will allow measurements of F_{χ_c} as a function of the J/ψ transverse momentum and Feynman-x[1]. The HERA-B Feynman-x acceptance includes negative values and should provide new knowledge to heavy quark production dependency of this parameter. The production cross sections of all the χ_c particles, including the χ_{c0} should be within reach.
The ECAL energy resolution is expected to be improved in the run 2002. Since the determination of the ratio of the production cross-sections of the χ_{c1} and χ_{c2} gives important input to the development of the NRQCD model, the possibility to disentangle these states must be thoroughly investigated. A measurement similar to the one performed in the E705 experiment [31] where the χ_{c1} and χ_{c2} states are disentangled may very well be within reach with the run 2002 data. If the energy resolution of the ECAL should prove insufficient, the expected statistics on χ_c particles will allow χ_c reconstruction from converted photons. The energy resolution of the Main Tracking System will then allow clean separation of the χ_c states.
The nuclear dependence of the Charmonium cross sections is given high priority in the 2002 physics program. Since HERA-B has the possibility to run with up to eight different target materials simultaneously the outlook for these studies are very promising.
Keeping in mind that a measurement of the $b\bar{b}$ cross section has already been performed with the statistics of the run 2000 [17], the expected yield of reconstructed 2.1 million J/ψ particles will allow a precise measurement of the $b\bar{b}$ cross section.

[1]See eq. 3.2 for the definition of the Feynman-x.

Appendix A

Plots for Optimization, Monte-Carlo

The object of this Appendix is to show the development of the reconstructed χ_c signal in Monte-Carlo for the cuts studied for the optimization in Section 5.2. The plots show the number of reconstructed χ_c particles and the significance (see Section 5.1.3, eq 5.8) of the signal for the different cut values. The black points show the values obtained for Carbon events, and the open points show the values for Titanium events.

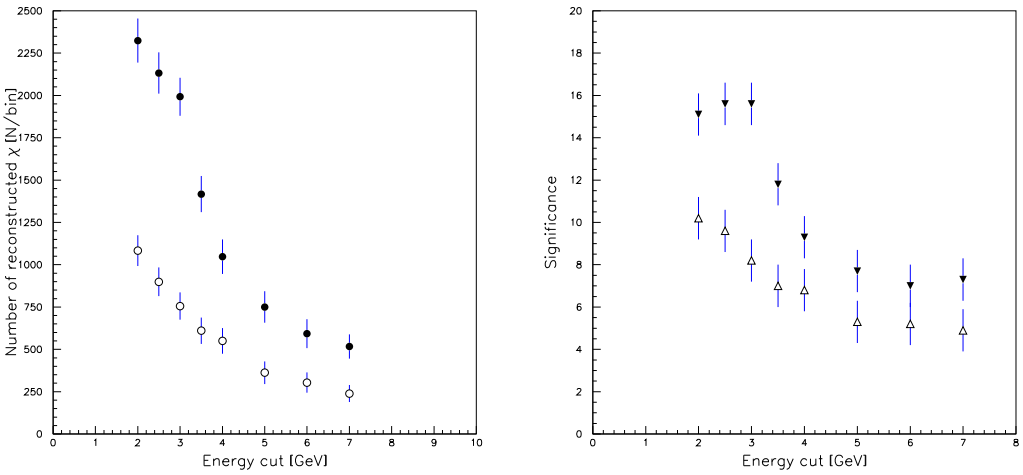

Figure A.1: Number of reconstructed χ_c (left) and significance (right) as a function of cuts on cluster energy

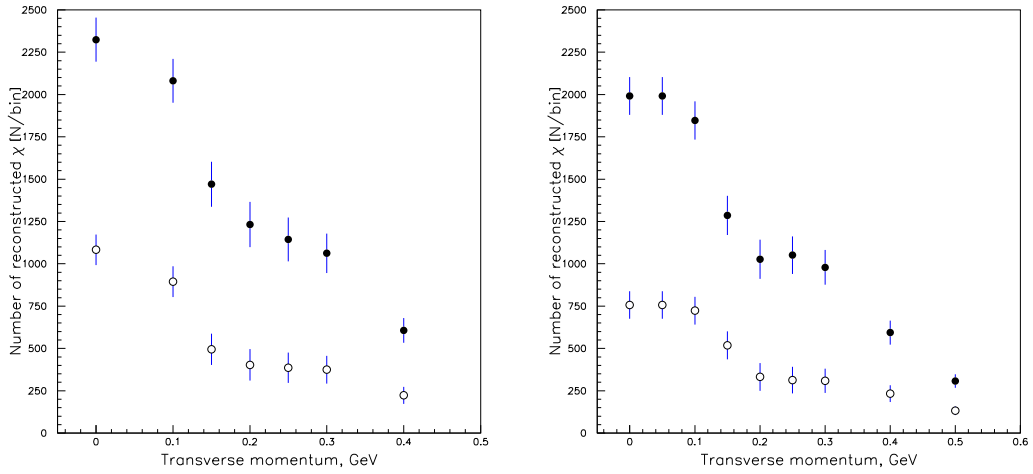

Figure A.2: Number of reconstructed χ_c mesons as a function of $P_\perp$ for energy cuts of 2.0 GeV (left) and 3.0 GeV (right)

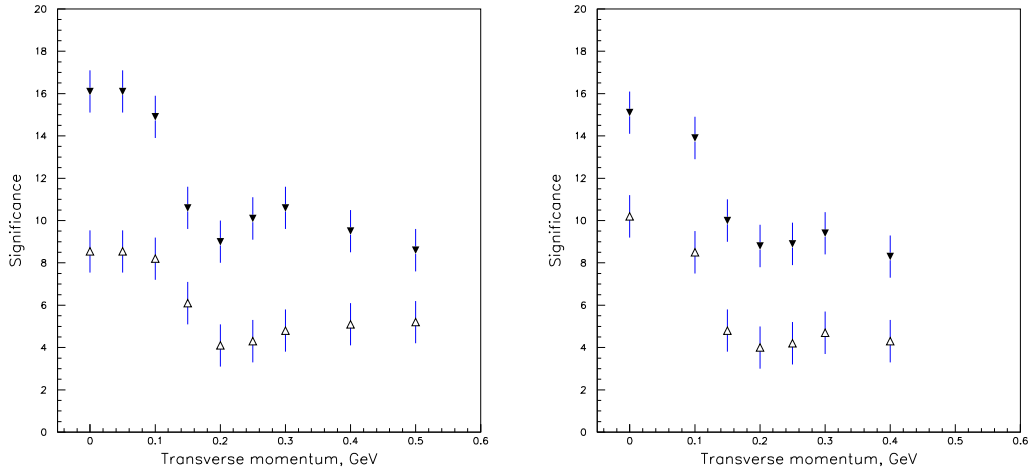

Figure A.3: Significance of the signal as a function of $P_\perp$. The plots have energy cuts of 2.0 GeV (left) and 3.0 GeV (right)

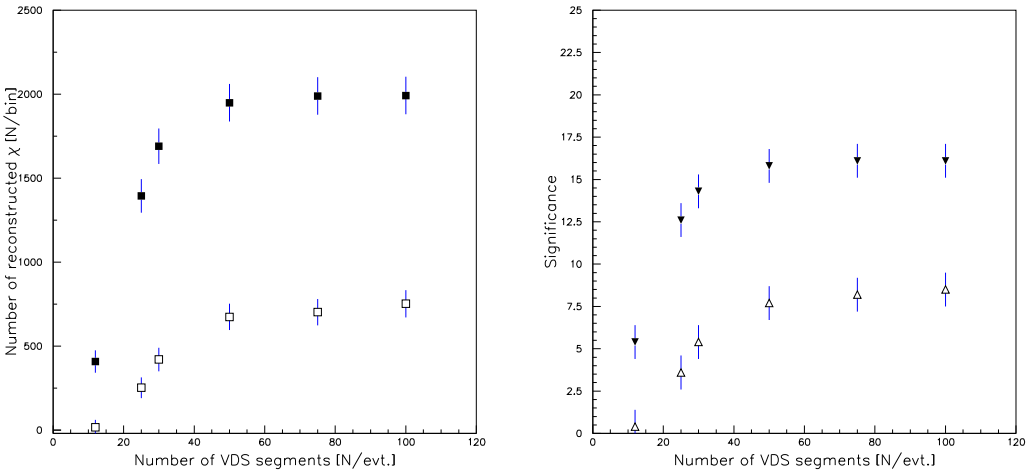

Figure A.4: Monte-Carlo: Number of reconstructed χ_c mesons (left) and signal significance (right) as a function of upper limits on N_{vds} .

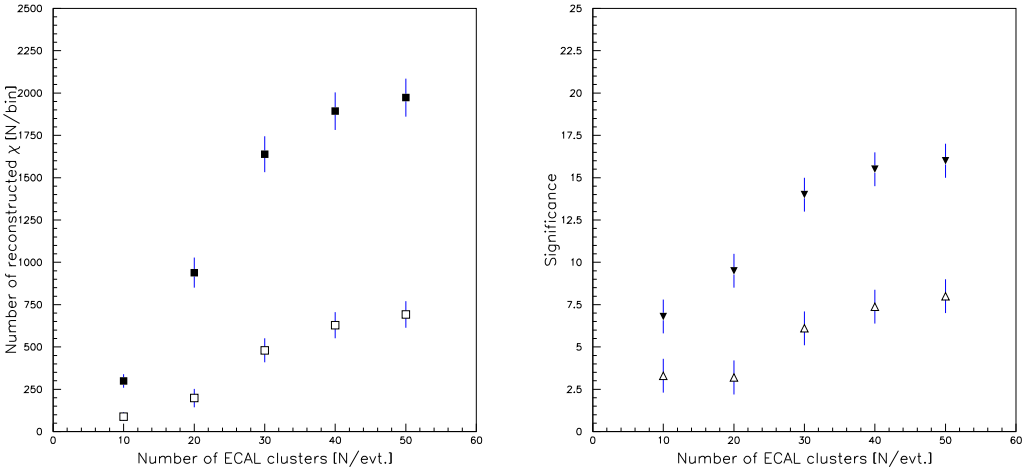

Figure A.5: Monte-Carlo: Number of reconstructed χ_c mesons as a function of upper limits onN_{clus} .

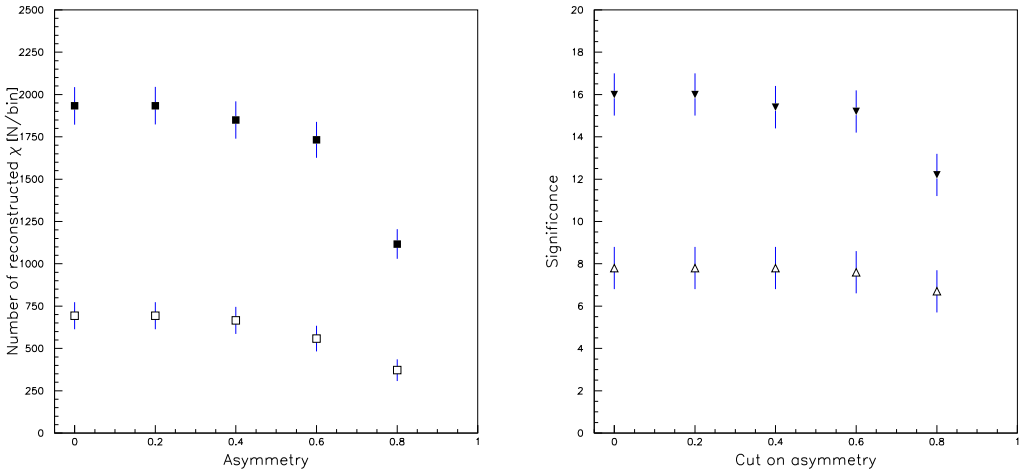

Figure A.6: Monte-Carlo: Number of reconstructed χ_c mesons (left) and significance (right) for asymmetry of the cluster.

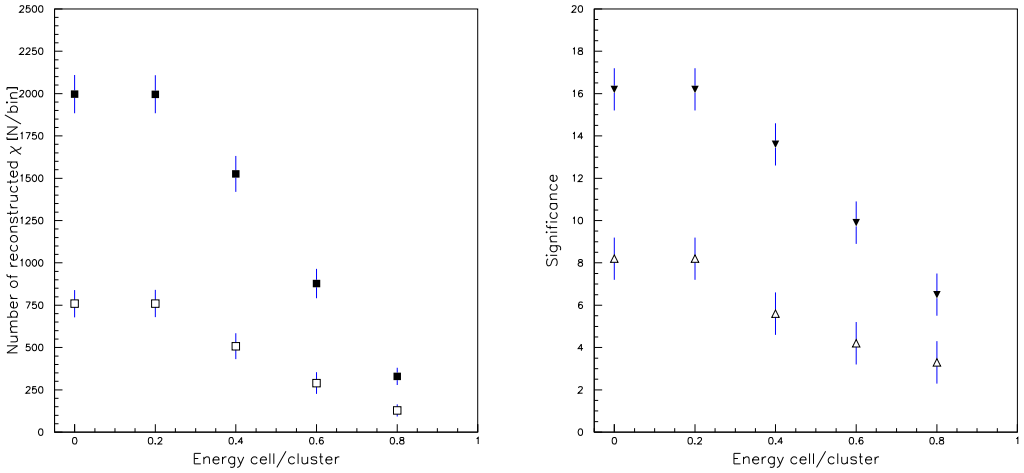

Figure A.7: Monte-Carlo: Number of reconstructed χ_c mesons (left) and significance (right) as a function of R_{clus} .

Appendix B

Plots for optimization, data

These plots are presented to show how the number of entries in the χ_c signal and the significance (see Section 5.1.3, eq 5.8) vary for the cuts studied for signal optimization in Section 5.2.
The plots are for Carbon and Titanium events as indicated in the captions.

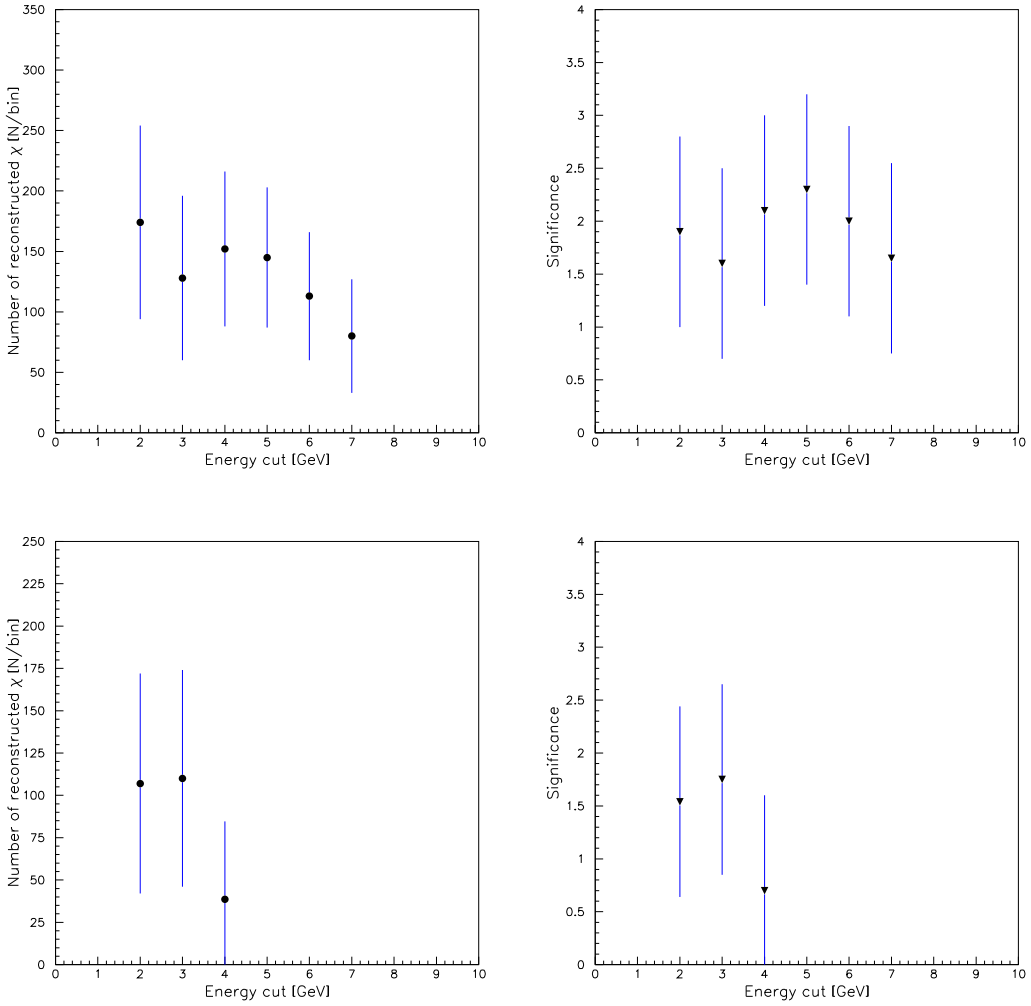

Figure B.1: Data Carbon and Titanium wire: Number of reconstructed χ_c (left) and signal significance (right) as a function of cluster energy. For Titanium data with clusters of energy larger than 5.0 GeV the signal was not well fitted.

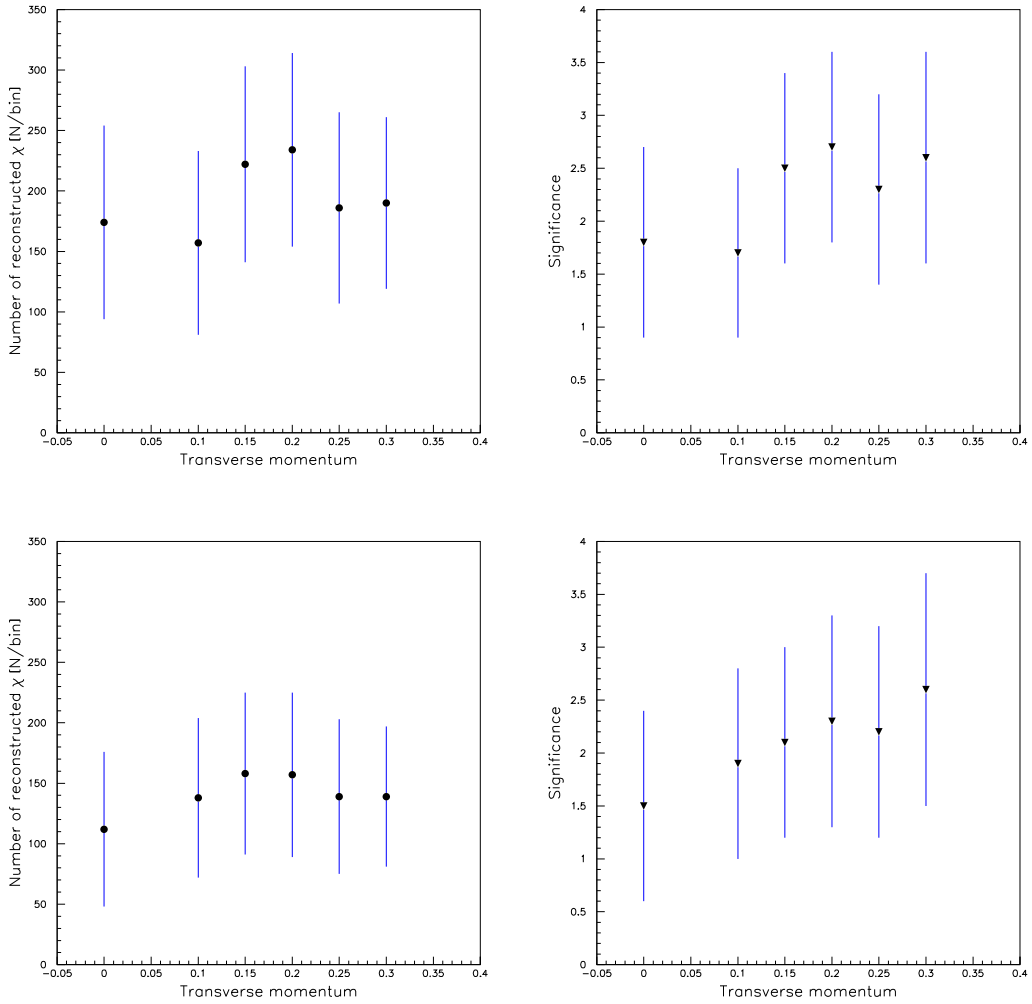

Figure B.2: Data, Carbon and Titanium wire: Number of reconstructed particles (left) and signal significance (right) for different values of transverse momentum. The energy cut on the clusters was 2.0 GeV

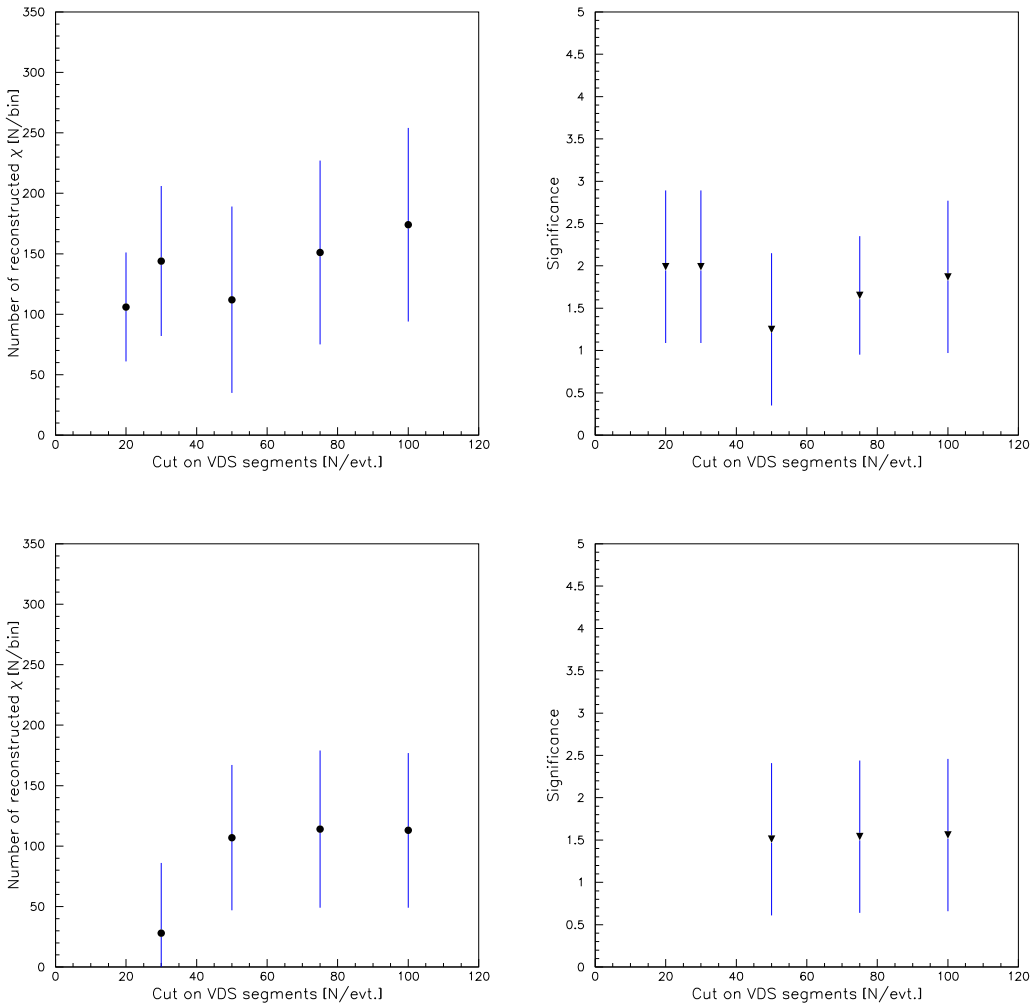

Figure B.3: Data, Carbon and Titanium wire: Signal and significance as a function of upper limits on N_{vds} .

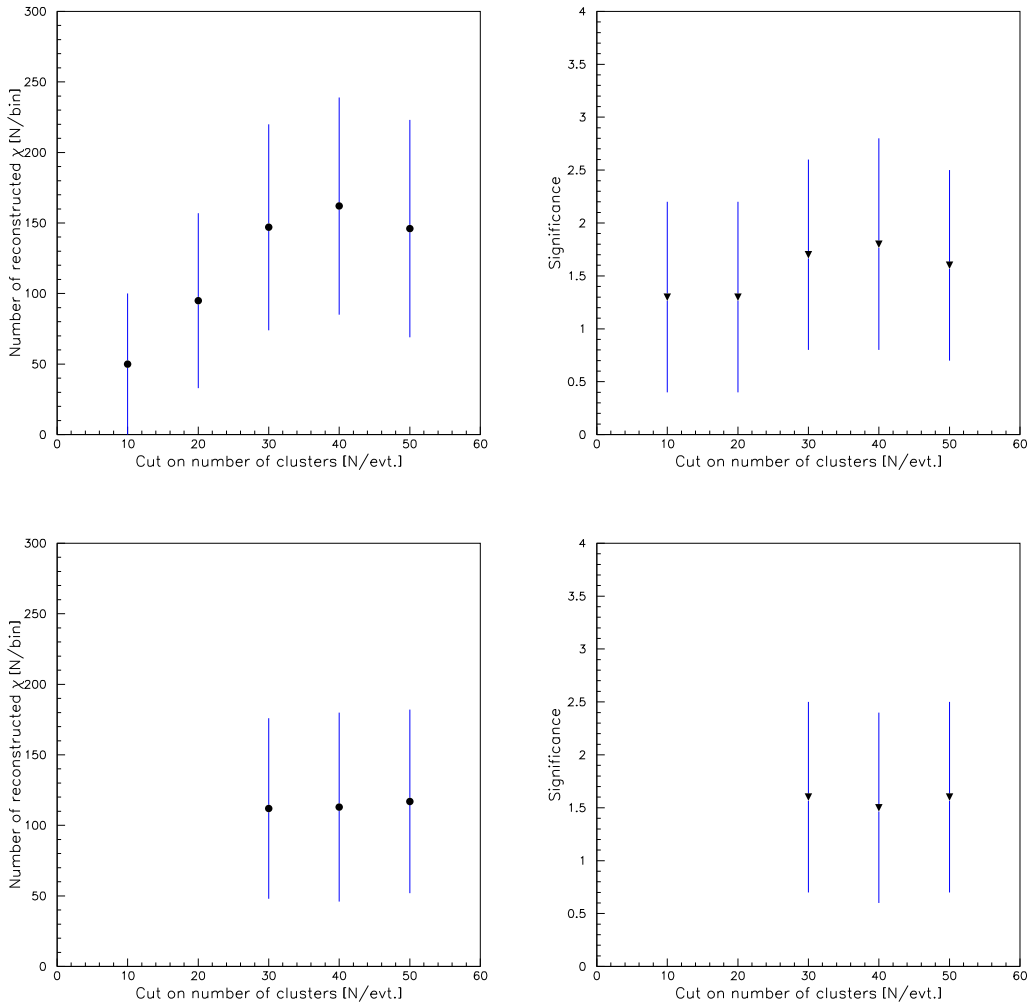

Figure B.4: Data, Carbon and Titanium wire: Number of reconstructed χ_c and significance for various cut values on the upper limit of N_{clus} for Carbon (upper plots) and Titanium wire (lower plots). For upper limits below 30 no signal was successfully reconstructed in the Titanium wire.

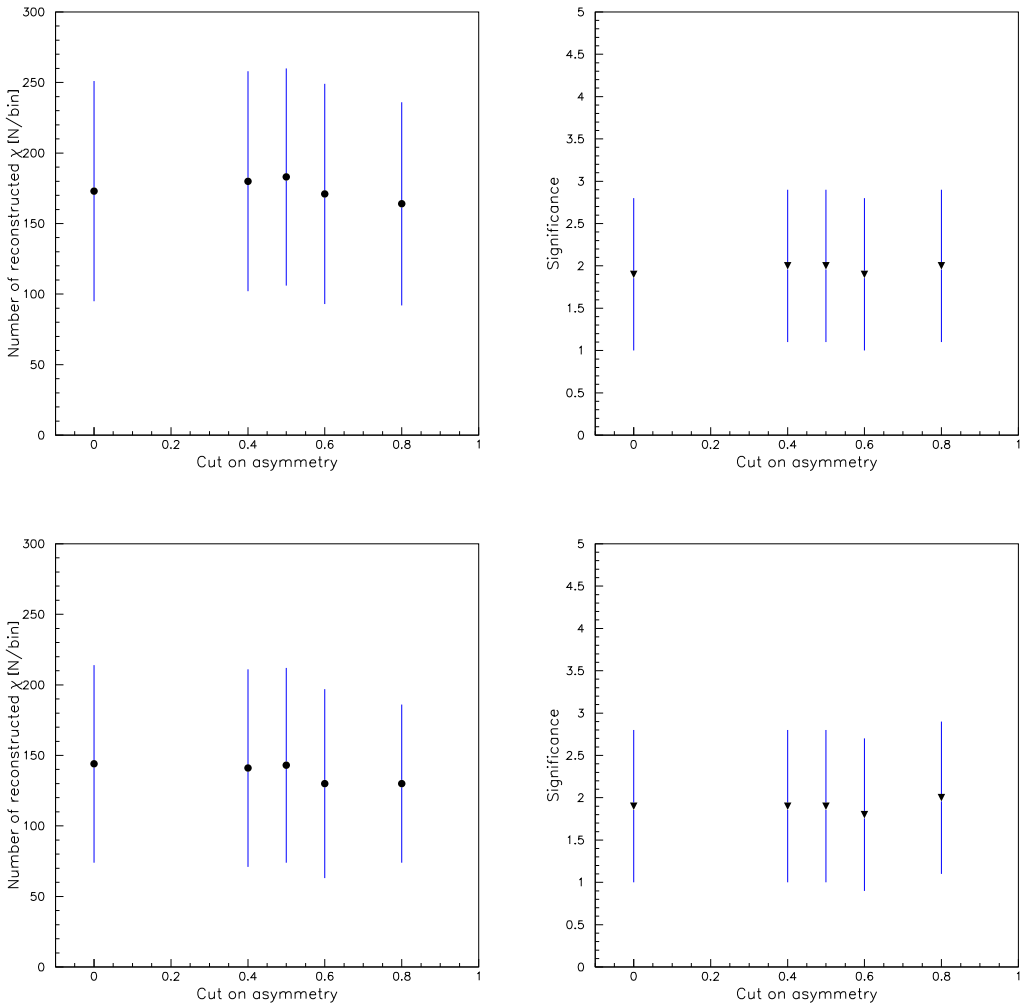

Figure B.5: Data: Carbon (top) and Titanium (bottom) wire: Number of reconstructed χ_c and significance as a function of cluster asymmetry.

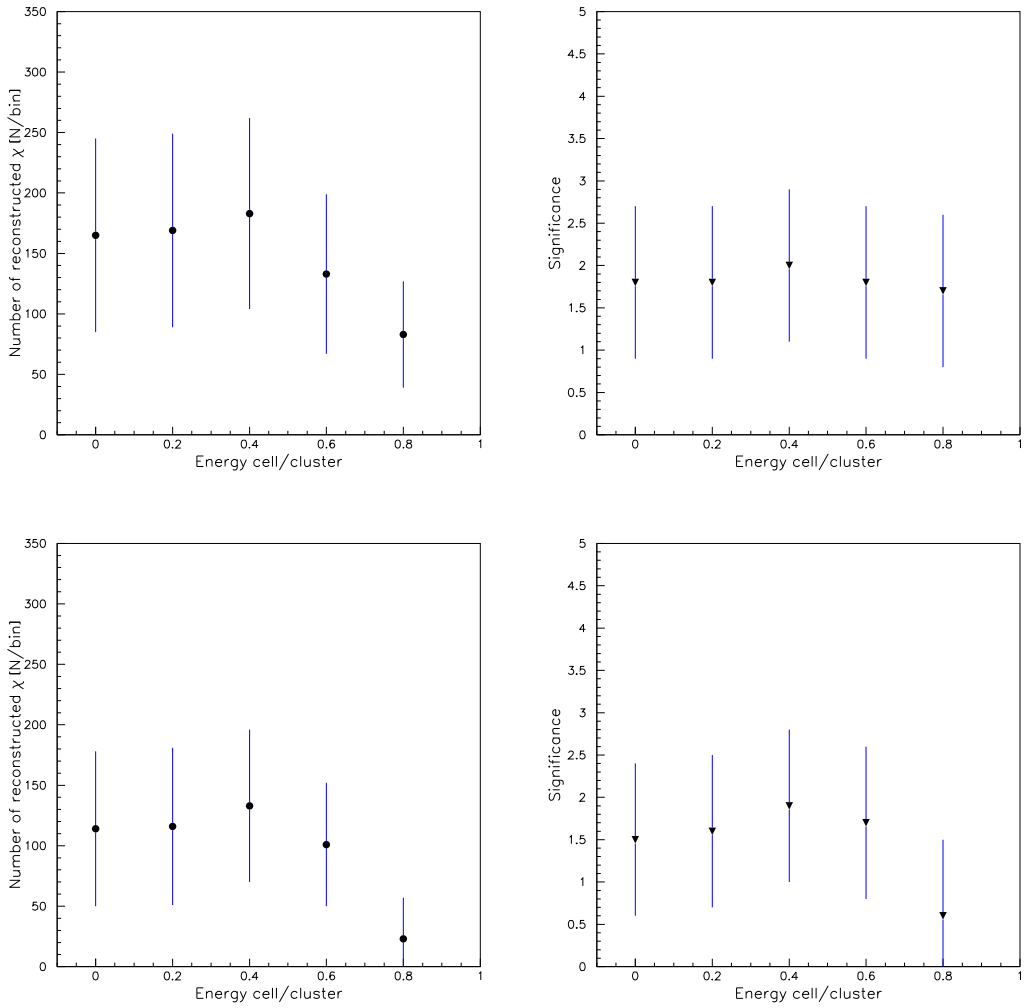

Figure B.6: Data, Carbon (top) and Titanium (bottom) wire: Number of reconstructed χ_c (left) and significance (right) as a function of the ratio between energy of the central cell of the cluster and the total cluster energy.

Appendix C

Summary of previous results

C.1 Introduction

In this chapter a summary of the previously obtained results for charmonium production is given. The emphasis is on results for the fraction of J/ψ produced from radiative χ_c decays (F_{χ_c}). Results on the production cross sections of J/ψ and ψ' are not included here. The intention is to describe the previous measurements by showing the obtained signals and to display some characteristics of the different analyses. The mentioned experiments all have a fixed target with the exception of the CDF-experiment where colliding $p\bar{p}$ beams are used. Both pion- and proton-beams have been accounted for.
Due to the low branching ratio of $\chi_{c0} \rightarrow J/\psi$ ($(6.6 \pm 1.8) \cdot 10^{-3}\%$ [33] this state is not considered in the following. Where mentioned the 'χ_c' particles refer to the χ_{c1} and the χ_{c2} states only. All the results presented here are summarized in Table C.1.

C.2 217 GeV $\pi^- Be, H_2$ reactions at Fermilab

This experiment was motivated by the results from the CERN intersecting storage rings which suggested that the J/ψ is produced primarily through an intermediate χ_c state [19],[20]. The measurements include estimation of F_{χ_c} in 217 GeV π^- H_2 and π^- Be collisions. The detector used was the Chicago Cyclotron Magnet Spectrometer Facility and approximately 160 J/ψ were collected in the $\mu^+\mu^-$ decay channel. The range of the transverse momentum ($P_\perp$) of the J/ψ was $0.0 < P_\perp < 3.2$ GeV and the Feynman-x (x_F) acceptance is measured between $0.0 < x_F < 0.9$ [21]. The photons used for reconstructing the mass of J/ψ γ were subject to an energy cut of $E_\gamma > 5.0$ GeV. The photons reconstructed with a γ γ invariant mass consistent with the invariant mass of the π^0 were also removed. The reconstructed J/ψ γ -spectrum (Fig. C.1) showed an excess of

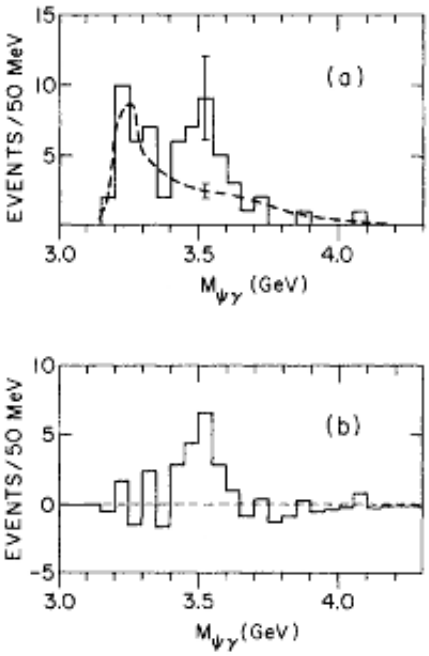

Figure C.1: Results from 217 GeV π^-Be,H at Fermilab: (a) The invariant mass of J/ψ γ , the dashed line indicates the background. (b) Invariant mass of J/ψ γ with subtracted background. The figure is from [21].

17.2 ± 6.6 events above the background in the χ_c mass-range. The background was described using photons from sideband $\mu^+\mu^-$ events combined with the full J/ψ -sample. Another method was suggested as well, namely using Monte Carlo generated photons from π^0 -decays combined with the J/ψ data sample. This method was reported to give close to the same background as the method of using photons from sideband events. The result for the fraction of produced J/ψ from radiative χ_c decay was F_{χ_c} $=0.70 \pm 0.28$.

C.3 The CERN Super Proton Synchrotron (SPS)

Results for the production cross-sections of both the χ_{c1} $(\sigma(\chi_{c1}))$ and the χ_{c2} $(\sigma(\chi_{c2}))$ and F_{χ_c} were published from the CERN Super Proton Synchrotron (SPS) in 1982 [22]. The Goliath spectrometer was used with a π^- beam of 185 GeV and collected a total of 44750 J/ψ events from a di-muon final state. The photons from radiative χ_c -decay were detected as the conversions $\gamma \rightarrow e^+e^-$ in a magnetic spectrometer. This method improves the experimental resolution because the resolution of a magnetic spectrometer in general is superior to that of an electromagnetic calorimeter. However, the global detection efficiency for the J/ψ γ reconstruction was only $1.15 \pm 0.06\%$. The χ_c states were reconstructed by constraining the mass of the J/ψ to 3097 MeV and setting the e^+e^- mass to 0 Mev. They were successfully separated and 91 events of the χ_{c1} state and 66 of the χ_{c2} state were observed (See figure C.2.). The fractions of J/ψ produced from χ_{c1} and χ_{c2} were then $F^{J/\psi}_{\chi_{c1}} = (17.7 \pm 3.5) \cdot 10^{-2}$ and $F^{J/\psi}_{\chi_{c2}} = (12.8 \pm 2.3) \cdot 10^{-2}$.

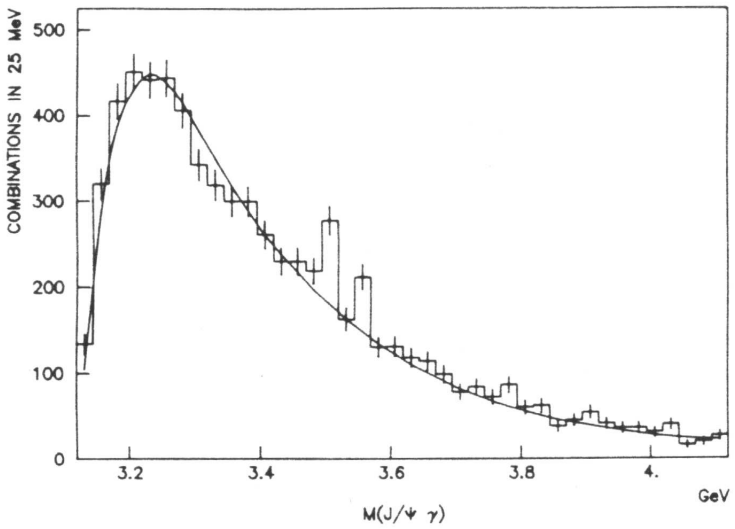

Figure C.2: Results from the SPS at CERN: The distribution shows the invariant mass of $J/\psi\ \gamma$, the full line is the estimated background. Two bins with a clear excess above the background show the χ_{c1} (3510 MeV) and χ_{c2} (3556 MeV) resonances. The figure is from [22]

This gives a total fraction of F_{χ_c} =$(30.5 \pm 5.0) \cdot 10^{-2}$. The production cross sections were calculated to $\sigma(\chi_{c1}) = 65 \pm 19$ nb/nucleon and $\sigma(\chi_{c2}) = 96 \pm 29$ nb/nucleon. This gives a total production cross section for the two χ_c states of $\sigma(\chi) = 160 \pm 35$ nb/nucleon and a cross-section ratio of $\frac{\sigma(\chi c1)}{\sigma(\chi c2)} = 0.68 \pm 69$.

C.4 The E673 experiment at Fermilab.

The E673 experiment at Fermilab used the superconducting Chicago cyclotron magnet particle spectrometer (CYCLOPS), and was an intended to test the charmonium production models. Proton and pion beams of 200 GeV and 190 GeV respectively were used on a Beryllium target [23]. Again the J/ψ particles were reconstructed from the di-muon final state and. An energy constraint of $3.0 < E_\gamma < 50$ GeV was imposed on the photons used for χ_c reconstruction. The expected width of one fitted χ_c state was $\sigma = 15.5 \pm 5$ MeV, sufficient to separate the two states. For the J/ψ particles the range for $P_\perp$ was 0.0-2.0 GeV and the $x_F$acceptance 0.1-0.7.

C.4.1 The pion beam

The pion-beam yielded 908 ± 41 J/ψ and 53.6 ± 17.1 χ_c (See figure C.3). The resolution of the photon detector was high enough to detangle the two χ_c states. The method was to fit two constrained Gaussians to the signal peak. The fits were constrained in the sense that the widths were set equal and their separation was fixed to the known mass difference between χ_{c1} and χ_{c2} . The number of χ_{c1} and χ_{c2} events was determined to 33.9 ± 14.0 and 19.7 ± 9.8 respectively. The result were F_{χ_c} =0.31 ± 0.10 with a contribution from the χ_{c1} of $F_{\chi_{c1}}^{J/\psi} = 0.20 \pm 0.08$ and from the χ_{c2} of $F_{\chi_{c2}}^{J/\psi} = 0.11 \pm 0.06$. The production cross sections were measured to $\sigma(\chi_{c1}) = 65 \pm 28$ nb/nucleon and $\sigma(\chi_{c2}) = 67 \pm 34$ nb/nucleon. This gives a cross section ratio of $\frac{\sigma(\chi_{c1})}{\sigma(\chi_{c2})} = 0.96 \pm 0.64$.

C.4.2 The proton-beam

The statistics for the proton-beam were somewhat lower than for the pion-beam, yielding 157 ± 17 J/ψ and a total of 11.8 ± 5.4 χ_c . (See figure C.3.) The limited statistics did not allow proper Gaussian fits to the signals, the number of events above the background for the two χ_c states were counted to be 8.3 χ_{c1} particles and 7.7 χ_{c2} particles. This gave F_{χ_c} =0.47 ± 0.23 and a cross-section ratio of $\frac{\sigma(\chi_{c1})}{\sigma(\chi_{c2})} = 0.24 \pm 0.28$. For the production cross-section, only a result for the χ_{c2} was obtained of $\sigma(\chi_{c2}) = 134 \pm 68$ nb/nucleon.

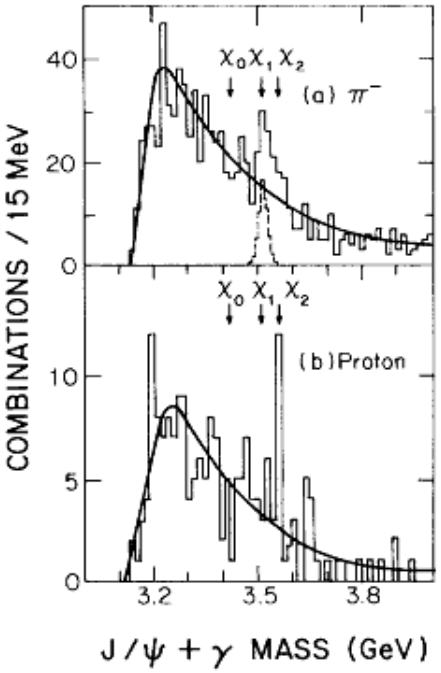

Figure C.3: Results from E673: Top: Results from the π^- -beam, showing peak above the background in the J/ψ γ spectrum. Bottom: Results from the proton-beam. The figure is from [23].

C.5 Results from the Collider Detector at Fermilab

This experiment at the Collider Detector at Fermilab (CDF) used $p\bar{p}$ collisions at $\sqrt{s} = 1.8$ TeV. A total of 32642 ± 185 J/ψ were reconstructed from a di-muon sample yielding 1230 ± 72 χ_c [28]. Photons with energy deposition higher than 1.0 GeV in one cell of the electromagnetic calorimeter were used for the χ_c reconstruction. In addition, a cut requiring that no charged tracks point to the cell of the photon candidate was imposed. The background was Monte-Carlo generated by using the J/ψ combined with photons from decays of π^0, η and K^0. The mass resolution for the χ_c states was 50 MeV and 55 MeV for the χ_{c1} and the χ_{c2} respectively. No attempt was made to separate the two states. However, by studying converted photons 46.7 ± 7 χ_{c1} particles and 23 ± 6 χ_{c2} particles were reconstructed and separated [29]. The results in [29] are not published in [28] and do not enter the results given in the following. The high statistics of this experiment allowed to measure the F_{χ_c} in different J/ψ $P_\perp$ -bins. Also, as another special feature of this experiment, the feed-down, or decay to J/ψ , from b-flavored mesons was accounted for. The results are corrected for this effect. For the other experiments mentioned here this effect is negligible [29]. For all bins of $P_\perp$ >4.0 GeV, the result was $F_{\chi_c} = 0.297 \pm 0.017 \pm 0.057$ where the first error is statistical and the second systematic. The results as a function of $P_\perp$ is shown in Fig C.5.

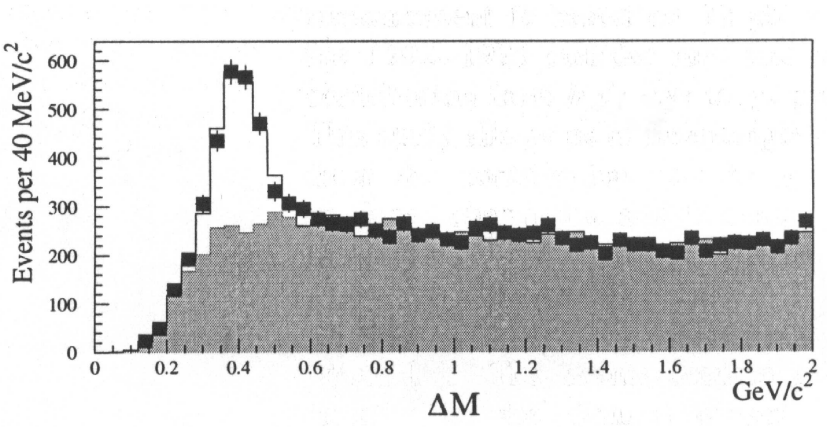

Figure C.4: Results from CDF: The mass difference of J/ψ γ and J/ψ showing a resonance at the mass difference of the χ_c states and the J/ψ . The figure is from [28].

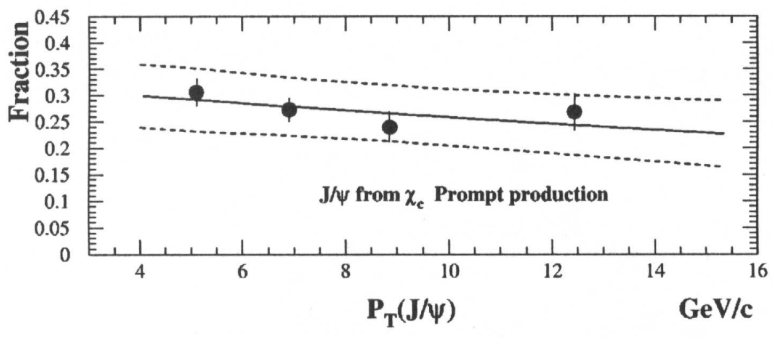

Figure C.5: Results from CDF, J/ψ ratio vs $P_\perp$: Ratio of produced J/ψ form χ_c -decay as a function of $P_\perp$. The figure is from [28].

C.6 The E705 experiment at Fermilab

The experiment used 300 GeV beams of pions and protons upon a fixed Lithium target. The positively charged beam had the partition of 45% π^+ and 55% p while the negatively charged beam consisted of 2% $\bar{p}$ and 98% π^- [29]. Due to low $\bar{p}$ statistics, only results from the π^+, π^- and p beams were published. The results for the π^+ and π^- beams were put combined for estimating the χ_{c1} and χ_{c2} cross-sections. There are two existing publications on χ_c -production from this experiment, [30, 31]. Of the two [31] has the most sophisticated analysis, including separation of the χ_{c1} and χ_{c2} states. The results presented here are therefore mainly be from this article.
The muonic decay of the J/ψ was studied and a total of approximately 25000 J/ψ were collected, 6090 ± 90 from the proton-beam, 12470 ± 160 from the π^--beam and 5560 ± 90 from the π^+-beam [30]. The χ_c was reconstructed by the addition of a photon required to have a total energy larger than 2.5 GeV. The $\gamma\ \gamma$ mass was also studied, and all photons with a reconstructed $\gamma\ \gamma$ -invariant mass less than 200 MeV were not used. This is to avoid using photons from the $\pi^0 \to \gamma\gamma$ decay for χ_c reconstruction. The background was described by pairing photons and J/ψ particles from different events and fitted with a ninth-order polynomial. In addition, an enhancement close to the mass of the χ_c caused by photons from radiative χ_c decay, but still from a different event, is removed by a 'second mis-pairing' by weighting each photon with the probability that it came from a χ_c . There is another interesting note on the background description in [30] where correlated effects like $\Psi(2S) \to J/\psi\pi^0\pi^0, J/\psi\eta$ and $J/\psi\gamma\gamma$ have been studied. The conclusion was that these effects do not enter the mass-difference spectrum above the mass difference between χ_c and J/ψ , and therefore the factor for scaling the background was extracted from the region above the χ_c -region ($\sim$460 MeV). The transverse momentum range for the J/ψ is approximately $0.0 < p_\perp < 4.0$GeV

and the Feynman-x acceptance was $-0.10 x_f < 0.45$ thereby covering also the negative $x_F$region.

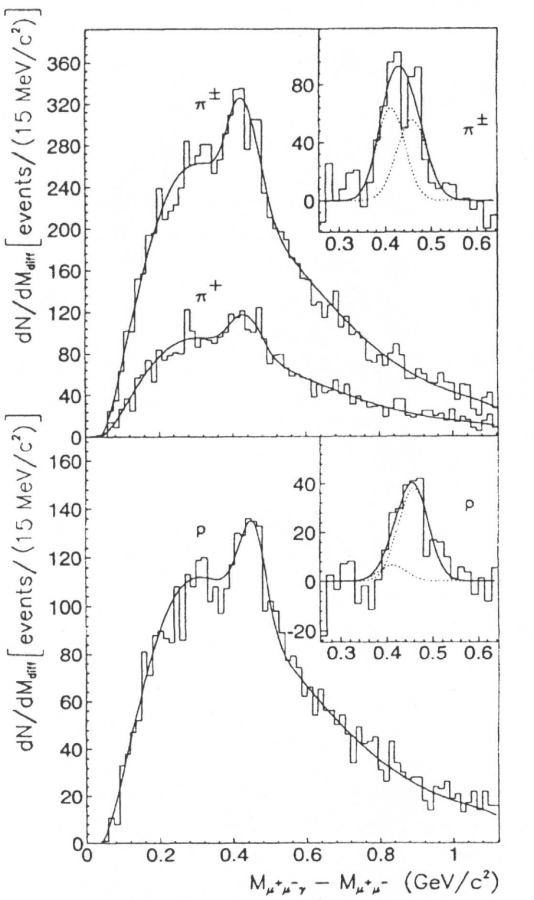

Figure C.6: Results from E705, Mass difference of J/ψ γ and J/ψ for $\pi^{\pm}$ (top) and proton-beam (bottom). The insets show the χ_c signal with subtracted background. The figure is from [31].

C.6.1 The pion-beams

For the pion-beams a total of 632 ± 84 χ_c particles were reconstructed. For the two beams the results on F_{χ_c} were $F^{J/\psi}_{\chi_c\pi^-} = 0.37 \pm 0.03$ and $F^{J/\psi}_{\chi_c\pi^+} = 0.40 \pm 0.04$ for the π^- and π^+ beams respectively [30]. The χ_{c1} and χ_{c2} were separated by fitting two Gaussians to the signal peak. (See figure C.6) The measured cross-sections for the combined pion beams are $\sigma(\chi_{c1}) = 146 \pm 55 \pm 15$ and $\sigma(\chi_{c2}) = 277 \pm 115 \pm 28$. The ratio of the cross-sections is $\frac{\sigma(\chi_{c1})}{\sigma(\chi_{c2})} = 0.52^{+0.57}_{-0.27}$. The production cross-section of the two χ_c states together is then $\sigma(\chi_{c2}) + \sigma(\chi_{c1}) = 423 \pm 128 \pm 32$.

C.6.2 The proton-beam

There were 244 ± 56 reconstructed χ_c -mesons from proton induced reactions [31]. The fraction of J/ψ produced from χ_c was measured to F_{χ_c} $=0.30 \pm 0.04$ [31]. Again the two χ_c -states were separated by fitting two Gaussian functions to the signal excess (Fig. C.6) and the found cross-sections were $\sigma(\chi_{c1}) = 31 \pm 62 \pm 3$ and $\sigma(\chi_{c2}) = 364 \pm 124 \pm 36$. The ratio of the two produced states was measured to $\frac{\sigma(\chi_{c1})}{\sigma(\chi_{c2})} = 0.08^{+0.25}_{-0.10}$ and the sum of the two cross-sections was measured to $\sigma_{\chi_{c2}} + \sigma_{\chi_{c1}} = 395 \pm 138 \pm 36$.

C.7 The E672/E706 experiment at Fermilab

This experiment used a 515 GeV negative pion-beam with fixed Beryllium and Copper targets. The J/ψ was reconstructed through a di-muon final state and photons converted to e^+e^- were used for the χ_c reconstruction. A total of 9600 ± 105 J/ψ were collected in the Feynman-x range of $0.10 < x_f < 0.80$ [29]. This resulted in a totally 84 ± 16 reconstructed χ_c , well separated into 47 ± 12 χ_{c1} and 37 ± 11 χ_{c2} (See figure C.7). The fraction of J/ψ from χ_{c1} was measured to $F^{J/\psi}_{\chi_{c1}} = 0.26 \pm 0.07$ and to $F^{J/\psi}_{\chi_{c2}} = 0.20 \pm 0.06$ for the χ_{c2} giving a total of F_{χ_c} $=0.47 \pm 0.47 \pm 0.23$. The production-ratio was estimated to $\frac{\sigma(\chi_{c1})}{\sigma(\chi_{c2})} = 0.63 \pm 0.25$.

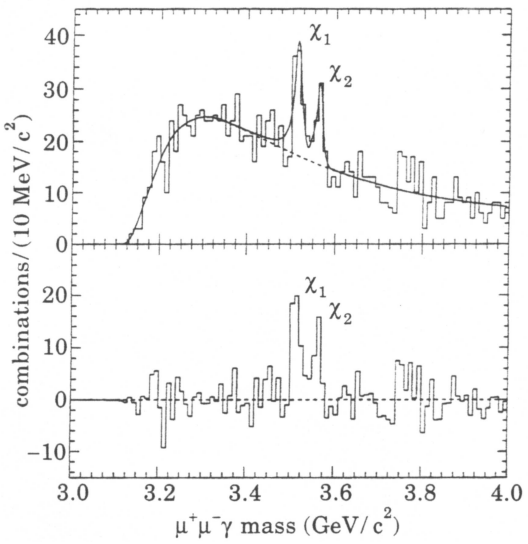

Figure C.7: Results from E672/E706: The J/ψ γ invariant mass spectrum (top) and the background subtracted signal (bottom). The figure is from [29].

C.8 The E771 experiment at Fermilab

For an incident proton-beam, this experiment was the first to cleanly separate the two χ_{c1} and χ_{c2} particles [32]. Here 800 GeV protons were incident on a fixed silicon target resulting in a center of mass energy of $\sqrt{s} = 38.8$ GeV. Again a di-muon final state was used to reconstruct the J/ψ . The sample yielded 11660 ± 139 J/ψ . Photons converted into e^+e^- were used to reconstruct the χ_c , and the obtained resolution allowed clean separation of χ_{c1} and χ_{c2} . (See figure C.8.) A total of 33 ± 9 χ_{c1} and 33 ± 10 χ_{c2} were reconstructed. The background was described by mixing J/ψ and photons from different events and then subjected to a polynomial fit. Two Gaussians are fitted to the signal with a width, determined by the fit, of 5.2 ± 2.0 MeV. The resulting production cross-sections are $\sigma_{\chi_{c1}} = 263 \pm 69 \pm 32$ nb/nucleon and $\sigma_{\chi_{c2}} = 498 \pm 143 \pm 67$ nb/nucleon, where the first error is statistical and the second systematic. The ratio is then $\frac{\sigma(\chi_{c1})}{\sigma(\chi_{c2})} = 0.53 \pm 20 \pm 0.07$ where again the first error is statistical and the second systematic With the errors defined the same way, the sum of the χ_c cross-sections are $\sigma_{\chi_{c2}} + \sigma_{\chi_{c1}} = \pm \pm 761 \pm 159 \pm 74$.

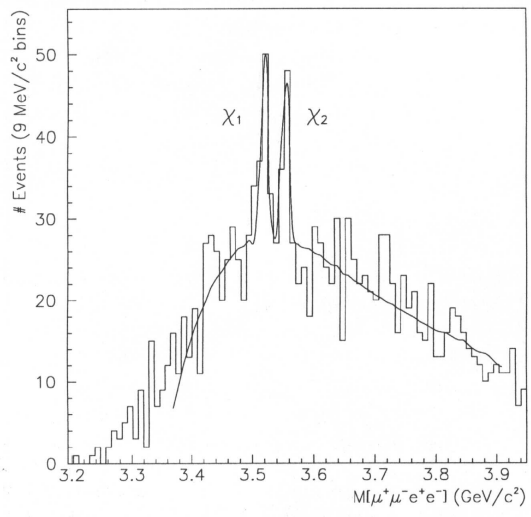

Figure C.8: Results from E771: The invariant mass of J/ψ e^+e^- . The solid line shows the polynomial fit to the background plus two Gaussians. The figure is from [32].

Exp.	Beam and Target	$N_{J/\psi}$	$N_{\chi_{c1,2}}$	F_{χ_c}	$\frac{\sigma(\chi_{c1})}{\sigma(\chi_{c2})}$	$\sigma(\chi_{c1,2})$[nb/nucl.]
FNAL	217GeV π^-Be,H	$\sim$160	17.2 ± 6.6	0.70 ± 0.28	-	-
SPS	185GeV/π^-Be	44750	157	0.31 ± 0.05	0.68 ± 0.29	160 ± 35
CDF	$\sqrt{s}$=1.8TeV$p\bar{p}$	32642 ± 185	1230 ± 72	$0.297 \pm 0.017 \pm 0.057$	-	-
E673	200GeV pBe	157 ± 17	11.8 ± 5.4	0.47 ± 0.23	0.24 ± 0.28	$134 \pm 68^{*}$
E673	190GeV π^-Be	908 ± 48	56.3 ± 17.1	0.31 ± 0.10	0.96 ± 0.64	$132 \pm 44^{**}$
E705	300GeV pLi	6090 ± 90	244 ± 56	0.30 ± 0.04	$0.08^{+0.25}_{-0.15}$	$395 \pm 138 \pm 36^{**}$
E705	300GeV π^-Li	12470 ± 160	590 ± 50	0.37 ± 0.03	$0.52^{+0.57}_{-0.27}$	$423 \pm 128 \pm 32^{**}$
E705	300GeV π^+Li	5560 ± 90	300 ± 35	0.40 ± 0.04		
E771	800GeV pSi	11660 ± 139	66 ± 14	-	$0.53 \pm 0.20 \pm 0.07$	$761 \pm 159 \pm 74^{**}$
E672/706	515GeV π^-Be,Cu	9600 ± 105	84 ± 16	$0.46 \pm 0.09^{***}$	0.63 ± 0.25	-

$*$) Result is for χ_{c2} only.
$**$) The published cross-sections of the χ_{c1} and the χ_{c2} have been added.
$***$) The published fractions for χ_{c1} and χ_{c2} have been added.

Table C.1: A summary of previously obtained results for the fraction of J/ψ produced from χ_c (F_{χ_c}) and the χ_c production cross-sections.

Bibliography

[1] J.J. Aubert *et al.* Phys. Rev. Lett. **33**, 1404 (1974)

[2] M. Beneke, hep-ph/9703429, (1997)

[3] R. K. Ellis *et al.* QCD and Collider Physics, CAMBRIDGE MONOGRAPHS ON PARTICLE PHYSICS, NUCLEAR PHYSICS AND COSMOLOGY **8** (1996)

[4] M. Beneke and I. Z. Rothstein, Phys. Rev. **D54**, 2005 (1996).

[5] G. T. Bodwin, E. Braaten, G. P. Lepage, Phys. Rev. D **51**, 1125 (1995)

[6] C. E. Carlson, R. Suaya, Phys. Rev. D **18**, 760 (1978)

[7] T. Lohse *et al.* HERA-B Proposal (1994)

[8] A. Christensen, Analysis meeting 22.01.02

[9] M. H. Schub, *et al.*, Phys. Rev. **D52** (1995)

[10] T. Sjøstrand, Comp. Phys. Comm. **82** (1994)

[11] H. Pi, Comp. Phys. Comm. **71** (1992)

[12] R. Brun *et al.*, GEANT3, Internal Report CERN **DD/EE/84-1**, CERN (1987)

[13] J. Ivarsson *et al.* HERA-B Note **99-067** (1999)

[14] O. Igonkina *et al.* HERA-B Note **00-103** (2000)

[15] O. Igonkina, HERA-B Note **02-028** (2002)

[16] O. Igonkina, HERA-B Note **01-067** (2001)

[17] The HERA-B Collaboration, HERA-B Note **02-005** (2002)

[18] The HERA-B Collaboration, HERA-B Note **01-064**, (2001)

[19] J.H. Cobb *et al.*, Phys. Lett. **72B**, 497 (1978)

[20] A. G. Clark *et al.*, Nucl. Phys. **B142**, 29 (1978)

[21] T. B. W Kirk *et al.*, Phys. Rev. Lett. **42**, 619 (1979)

[22] Y. Lemoigne *et al.*, Phys. Lett. **113B**, 509 (1982)

[23] D. A. Bauer *et al.*, Phys. Rev. Lett. **54**, 753 (1985)

[24] R. Mankel, HERA-B note **95-239** (1995, revised 1997)

[25] HERA-B Software Group, Arte The Event Reconstruction and Analysis Tool for HERA-B (1996)

[26] D. Emelyanov *et al.*, Grover Manual (2001)

[27] The ALEPH Collaboration, **CERN-EP/2001-090** (2001)

[28] CDF Collaboration, Phys. Rev. Lett. **79**, 578 (1997)

[29] CDF Collaboration, Il Nuovo Cimento, **109A**, 827 (1996)

[30] E705 Collaboration, Phys. Rev. Lett. **70**, 383 (1993)

[31] E705 Collaboration, Phys. Rev. D **49**, 543 (1994)

[32] E771 Collaboration, hep-ex/9908010 (1999)

[33] Particle Data Group, The European Physical Journal. C, **3**, (1998)

[34] M. Staric, P. Krizan, Nucl. Instruments & Methods in Physics Research A **433** 279 (1999)

[35] R. Eckmann, D. Dujmic, HERA-B Note 00-004 (2000)

[36] M. Villa, Collaboration Meeting, June (1997)

[37] Mauro Villa, private communication

[38] The HERA-B Collaboration, HERA-B Note 01-064 (2001)